SYNTHESIS AND CHARACTERIZATION OF POROUS AND DENSE SILICON OXYCARBIDE (SiCO) MATERIALS

by

SUSANA ISABEL AGUIRRE-MEDEL

Presented to the Faculty of the Graduate School of

The University of Texas at Arlington in Partial Fulfillment

of the Requirements

for the Degree of

DOCTOR OF PHILOSOPHY

THE UNIVERSITY OF TEXAS AT ARLINGTON

August 2019

Acknowledgements

I wish to express my gratitude to my advisor Professor Peter Kroll, who provided me with continuous support and opportunities through my doctorate degree. I am truly thankful for all the projects, conferences, workshops and periods abroad that I had the opportunity to experience, as well as the freedom and trust to develop my researcher skills in my doctorate degree.

I specially want to thank Professor Sorarù from the University of Trento in Italy, for giving me the opportunity to work in his lab, I learned a lot in his laboratory with his continuous support, and knowledge along with the help of Prasanta Jana, Emanuele Zera and Professor Campostrini. I would like to thank everyone at UTA who help me throughout my degree: Dr. Edwards who I cannot thank enough for all the hard work he put into helping me build lab instruments, training me, and characterizing my materials, I also want to thank Dr. Gout for all her help, support, encouraging and uplifting talks throughout these years. I want to thank Dr. Lang, for all the stimulating conversations, his enthusiasm and interest have been very enlightening. I also want to thank all my group members for their assistance and support. I also want to thank the departmental staff at UTA for their hard work. Thanks to the undergraduate students that I had the privilege to train and introduce to experimental research. Special thanks to Kendall Hendrix for her hard work, willingness to help and learn skills in the laboratory. It is always motivating and refreshing to help others learn and enjoy research.

I want to thank my beloved parents who have always supported me, encouraged me and provided me with the necessary strength to always keep going. I could not have done it without them.

August 01, 2019

Abstract

SYNTHESIS AND CHARACTERIZATION OF POROUS AND DENSE SILICON OXYCARBIDE (SiCO) MATERIALS

Susana Isabel Aguirre-Medel, PhD

The University of Texas at Arlington, 2019

Supervising Professor: Peter Kroll

In the field of materials discovery, the appearance of Polymer Derived Ceramics (PDC's) over 30 years ago represents a breakthrough in materials science and development. The PDC route represents significant advantages in ceramic science and technology. This route enables synthesis of bulk ceramics, fibers, porous ceramics and coating materials that are stable at temperatures up to 2000 ºC. PDCs can be separated into binary and ternary systems. Examples of binary systems are silicon carbide (SiC) and silicon nitride (Si_3N_4). Ternary systems include silicon carbonitride (SiCN) and silicon oxycarbide (SiCO). One very important feature of PDCs is their crystallization resistance. For example, silica (SiO_2) crystallizes into cristobalite while the SiCO system remains amorphous.

Recent insight into the micro and nanostructural features of these materials has provided understanding of the properties of these materials and their applications. The development and applicability of PDC materials is interdisciplinary requiring expertise from physicists, chemists, material scientists, engineers, and mineralogists.

In this work, we focus our investigation into the ternary system SiCO. Our objective is to contribute to the field of PDC materials by investigating microstructural,

physical and chemical properties of these materials. First, we present the synthesis and characterization of SiCO aerogels and provide insight into the importance of solubility parameters in the microstructural features of these materials. We synthesized SiCO aerogels and reported the importance of polymer solubility and swelling in the microstructural features of these materials.

Then, we present the synthesis of ambient dried SiCO ceramics and characterized their microstructural features as well as the adsorption efficiency. We compared the adsorption efficiency of porous SiCO to mesoporous silica and activated carbon. Porous SiCO had outstanding adsorption ability towards methylene blue (MB) and results indicated that highest Specific Surface Area (SSA) is not the most important characteristic in the adsorption of dyes in these materials.

To investigate more closely the polymer to ceramic conversion of these SiCO materials, ambient-dried SiCO were annealed in inert atmosphere starting from 400 °C up to 1000 °C. Nitrogen adsorption analysis along with FE-SEM imaging suggest that pore development as well as particle shrinkage of SiCO play a role in the microstructural properties of sol-gel derived SiCO ceramics.

Last, to investigate high temperature behavior of SiCO PDC ceramics, we synthesize carbon-rich SiCO bulk ceramics when annealed up to 1500 °C. We obtained information about the phase separation of SiCO ceramics, the increase of SiC crystalline growth and the presence of small and decreasing graphite peaks with increasing annealing temperature. XRD and Raman analysis show increased arrangement of the free carbon phase present in these SiCO ceramics.

Table of Contents

List of Illustrations

List of Tables

Chapter 1

Introduction

1.1 Aerogels

Aerogels are porous materials with properties such as optical transparency (up to 99 %), low density (0.003 - 0.8 g/cm^3), high porosity (95 to 99 %)[1] low thermal and low dielectric constant, low sound velocity (100 m/s)[2-3], and low conductivity (~0.01 W/mK).[4] These porous materials have a wide array of applications in research and industry including adsorption, catalysis, sensing, and insulation.[5] Kistler coined the term aerogel in 1932 to refer to gels in which the solid network does not collapse when the liquid is replaced with gas. Kistler applied the supercritical drying technique for the first time.[6] This procedure prevents the formation of gas-liquid interphase, which causes mechanical tension in the liquid and pressure of the walls that cause gel shrinkage.[5] The main advantage of supercritical extraction is the almost complete elimination of capillary forces[2], which minimizes pore collapse.

1.2 SiCO Materials

Silicon oxycarbide (SiCO) materials belong to the polymer-derived ceramic (PDC) synthesis route.[7-9] SiCO materials have general composition as $SiC_xO_{2(1-x)} + yC_{free}$.[10] Free carbon content in these materials affects their physical and chemical properties.[11,8] For example, an increasing amount of free carbon forms a percolating network which increases the electrical conductivity,[7] as well as increasing the stability of SiCO. Kleebe et al. studied this material and found that SiCO with greater carbon content displays higher elastic modulus and increased oxidation resistance in comparison to pure silica.[12] Moreover, SiCO remains amorphous above 1200 °C, where pure silica (SiO_2) crystallizes.[13] The improved properties of SiCO in comparison to SiO_2, are motivating for the synthesis of SiCO aerogels. Aerogels are solid porous materials well known particularly for their small pore size, large specific surface area (SSA), and for displaying the best optical transmission observed in porous materials as well as displaying a variety of interesting properties.[4] The structure of SiCO materials is varied

and depends on molecular precursor, composition, and synthesis conditions.[14] For example, the hydrogen content in the structure varies with exposure temperature in synthesis. At temperatures below 1000 °C, the material appears homogeneous and amorphous, and at temperatures above 1200 ºC, SiCO undergoes phase separation with SiC, carbon, and SiO_2.[12, 15] One peculiar feature of SiCO is the possibility of dissolving significant amounts of carbon within the glass network, which is not feasible using common solid-state synthesis methods.[16] As a consequence, SiCO is only synthesized through the molecular route because the solubility of SiC in silica is about 1%.[15] Silicon oxycarbide possesses a large mole fraction of carbon along with the silica structure accounting for improved crystallization resistance. SiCO displays greater resistance to oxidation[13] and corrosion in comparison to pure silica.[17] Whereas silica crystallizes into cristobalite at 1200 °C, SiCO remains amorphous up to 1250 °C.[13] At temperatures close to 1300 °C, SiCO undergoes phase separation into silicon carbide, silica, and free carbon, but the silica phase remains amorphous up to 1500 °C.[13] The following figure shows the phase composition of silicon oxycarbide materials.

$$SiC_xO_y = \left\{\frac{y}{2}SiO_2 + (1-\frac{y}{2})SiC\right\} + (x+\frac{y}{2}-1)C$$

SiCO glass “free” carbon

Figure 1-1 SiCO composition (SiCO glass and "free" carbon)

The following figure displays the schematic composition diagram for a SiCO system. SiC_xO_y represents the overall composition of a given sample. The SiCO separation mechanism is divided into two steps. Initially, the SiCO system separates into free carbon and amorphous SiO_xC_y. This separation is located on the tie-line between SiO_2 and SiC phases. The second step involves phase separation of the SiO_xC_y into SiC, SiO_2, and other intermediate SiCO compositions which are located along the SiC-SiO_2 tie-line.[13]

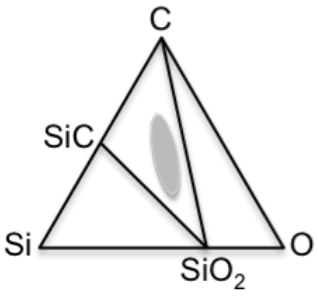

Figure 1-2 Composition diagram for silicon oxycarbide materials

1.3 SiCO Aerogels

SiCO aerogels are commonly synthesized via the sol-gel or the polymer-route. The polymer- route involves the crosslinking of organic-inorganic polymers such as siloxanes to form a gel. After gelation, solvent exchange is performed to eliminate unreacted precursors. Afterward, drying is traditionally performed using supercritical drying (generally with CO_2) to obtain a preceramic gel. The solvent used in synthesis impacts density, porosity, and surface morphology.[18] The objective of using supercritical drying is to prevent pore collapse by the elimination of liquid-gas interphase.[5] Subsequent heat treatment transforms the material into an amorphous ceramic. SiCO aerogels have a density ranging from 0.250 to 0.950 g/cm[3,7], and porosity of 55 to 90 vol %. PDC aerogels have been synthesized and characterized for gas sensing,[19] anodes for Li-ion batteries,[20] water purification,[21] and electromagnetic adsorbers.[22]

Chapters 2, 3, and 4 are devoted to the investigation of porous SiCO materials. First, chapter 2 presents a study of SiCO PDC aerogels synthesized using a variety of solvents to analyze the effects of polymer solubility. Recently, some research has focused on the investigation of SICO aerogels using acetone as solvent.[23-24] We investigate microstructural properties of aerogels synthesized with four different solvents, and compare our results to provide a rationale for these particularities.

Chapter 3 investigates ambient dried porous SiCO materials, sol-gel SiCO porous materials are reported in the literature.[25-27] In this chapter, we present a different synthesis

method for SiCO porous ceramics. We characterize these materials before and after ceramic conversion and present a comparison study of SiCO ceramics to mesoporous silica and activated carbon in the adsorption properties of the cationic dye methylene blue (MB). Chapter 4 shows the investigation of the ceramic conversion of these materials. We take a close look at the microstructural characteristics of SiCO materials when annealed up to 1000 ºC.

1.4 PMHS/DVB System Importance

The PMHS + DVB (polymethylhydrosiloxane + divinylbenzene) system was first introduced to study the microstructural evolution of SiCO ceramics with a high amount of free carbon. The PMHS + DVB system was introduced by Kleebe and Blum in 2005.[28] Later on, a thorough spectroscopic investigation of carbon-rich SiCO ceramics was published.[29] Subsequently, a systematic study of these ceramics was done, transmission electron microscopy (TEM) was used to investigate the evolution of the free carbon phase from 1000 to 1450 °C. The microstructural evolution of SiCO ceramics showed a material that remained primarily amorphous with a turbostratic carbon phase and SiC nanoparticles.[12]

More recently a systematic study of PMHS + 60% DVB SiCO materials was published, where they used TG-MS, Raman, NMR, SEM, and optical microscopy to investigate the pyrolytic conversion of these materials up to 1450 °C.[30] Other studies have investigated the polymer to ceramic conversion of PHMS+DVB ceramics.[17, 31-32] As well as the crosslinking of only PMHS using a platinum catalyst.[33]

Chapter 5 of this thesis provides a systematic investigation of a 2:1 mass ratio of PHMS: DVB SiCO ceramic annealed from 1000-1500 °C. In this work we have prepared samples in 100 °C increments in order to provide a detailed study in this temperature range.

The XRD analysis provides information about the progressive increment of SiC crystalline growth as well as the presence of small and decreasing graphite peaks with increasing annealing temperature. The XRD analysis provides information about the formation

of graphite in these materials, and along with Raman analysis, we investigate the free carbon phase present in these SiCO ceramics.

Chapter 2

Effects of Solvents on Microstructural Features of Poly(methylhydrosiloxane)/Divynilbenzene Aerogels

Abstract

The impact of solvents on the microstructure of poly(methylhydrosiloxane)/divinylbenzene (PMHS/DVB) aerogels was investigated. The gels are obtained in highly diluted conditions via hydrosilylation reaction of PMHS bearing Si-H groups and cross-linking it with carbon-carbon double bonds of DVB. Polymer aerogels are obtained after solvent exchange with liquid CO_2 and subsequent supercritical drying. Samples are characterized using microscopy and porosimetry. Common pore-formation concepts do not provide a solid rationale for the observed data. Solubility and swelling of the cross-linked polymer in various solvents are major factors governing pore formation of these PMHS/DVB polymer aerogels. Four different types of organic solvent (n-hexane, cyclohexane, tetrahydrofuran, and acetone) have been used while keeping all the other synthesis parameters fixed. Results indicate the importance of polymer solubility and swelling in the obtained SiCO aerogels.

2.1 Introduction

Although the PDC (Polymer Derived Ceramic) route has been extensively used for synthesizing Si-based ceramics, it was not until recently that SiC, SiCN and SiCO aerogels were synthesized using the PDC route.[3-4] In this process, first, a polymer aerogel is synthesized and then converted, through a pyrolysis process in inert atmosphere, into the corresponding PDC aerogel. The polymer aerogel is synthesized via hydrosilylation of a Si-based polymer bearing Si-H bonds with molecules bearing C=C moieties.[5] The cross-linking is performed in highly diluted conditions.

PDCs aerogels have been found to have different applications. For example, SiCO aerogels were found to show good sensing response towards N_2 at 300 °C and H_2 at 500 °C.[6]

In a separate study SiCO aerogels showed high specific reversible capacity of more than 900 mAh/g with 360 mAh/g (10 C) charging rate.[7]

2.2 Experimental

2.2.1 Chemicals

Poly(methylhydrosiloxane), PMHS (*MW~1900, CAS: 63148-57-2)* and divinylbenzene (DVB, technical grade, 80%, CAS: 1321-74-0) were purchased from Alfa Aesar (Alfa Aesar Ward Hilt MA, USA). The solvents, cyclohexane, and acetone were bought from J. T. Baker (Fisher Scientific Italia, Rodano, Italy), tetrahydrofuran (THF) from Sigma-Aldrich (Sigma-Aldrich, Saint Louis, MO, USA) and n-hexane from Chem-Lab (Chem-Lab, West-Vlaanderen, Belgium). Karstedt's catalyst (platinum divinylmethylsiloxane complex, ~2% in xylene (*CAS: 68478-92-2)*) was bought from Sigma Aldrich, Saint Louis, MO, USA. All the chemicals were used as purchased without any further purification step.

2.2.2 Aerogel Synthesis

All samples were prepared with a 1:2 mass ratio of PMHS to DVB. In a standard reaction 0.5 g (0.47 cm^3) PMHS and 1.0 gram (0.93 cm^3) DVB were mixed in 5.5 g of solvent. The mixture was homogenized with a magnetic stirrer for two minutes before 10 µL of the Pt catalyst was added under stirring for another two minutes. After that, the mixture was transferred into a pressure reactor (Parr acid digestion vessel; model 4749 Parr, IL, USA) and placed into a furnace at 150 ºC for 3 and 6 hours. After crosslinking the sample was taken off the furnace and allowed to cool to room temperature.

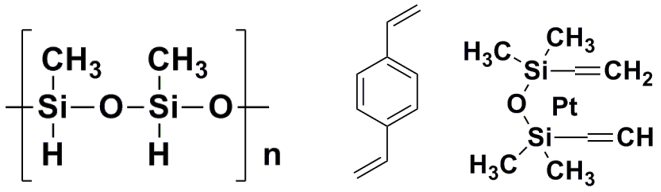

Figure 2-1 From left to right: PMHS, DVB and Karstedt's catalyst used for aerogel synthesis

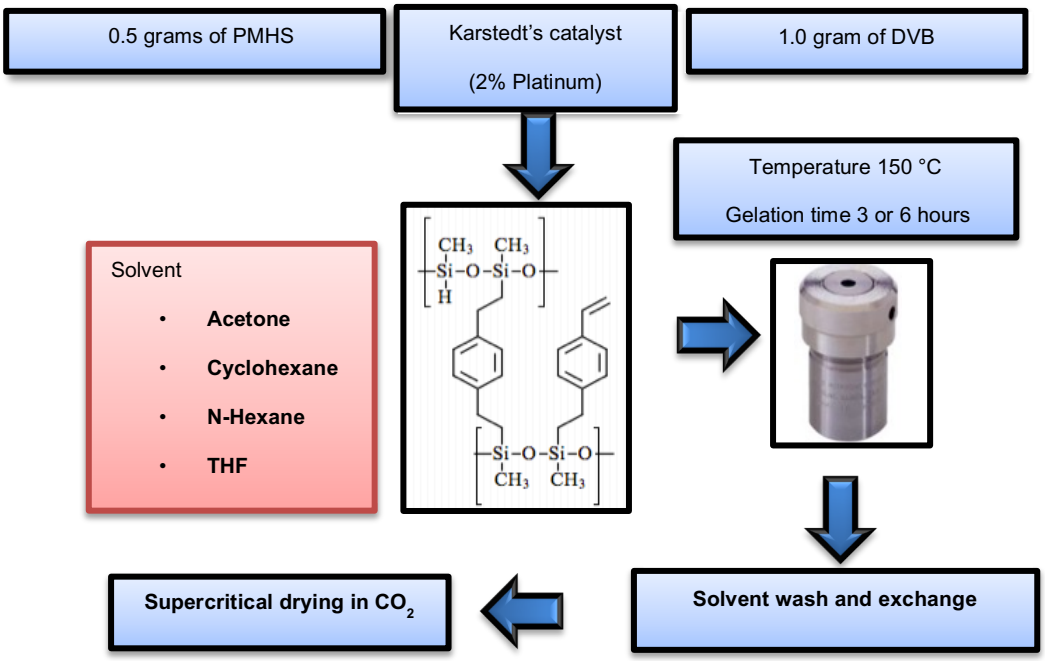

Figure 2-2 Aerogel synthesis scheme

The wet gels were extracted from the container and washed five times with fresh solvent to eliminate unreacted reagents and the Karstedt's catalyst. Figure 2-2 displays the aerogel synthesis scheme. After synthesis, the wet gel was transferred into a homemade CO_2-reactor equipped with two glass windows that allow visual control of the solvent exchange with CO_2 and supercritical drying process. Inside the reactor, the sample was washed with liquid CO_2 at 10 ºC twice a day for a total of ten solvent exchanges. As the final step of the drying process, the temperature in the dryer was slowly increased to 45 ºC at a pressure of 100-110 bar. Supercritical drying was then performed overnight. The complete procedure was performed using THF, cyclohexane, n-hexane, and acetone as solvents. Figure 2-3 shows the supercritical dryer instrument used for the solvent exchange and supercritical drying.

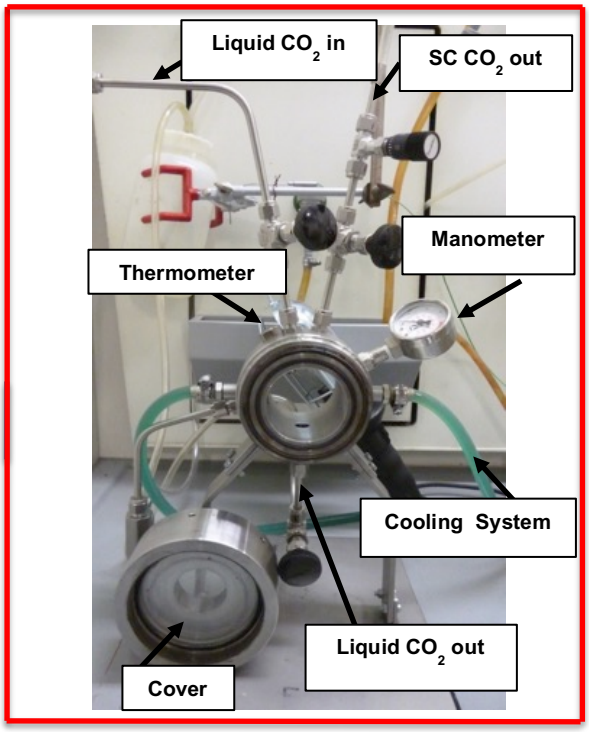

Figure 2-3 Homemade supercritical dryer

2.2.3 Characterization Procedure

2.2.3.1 Nitrogen Adsorption Analysis

Porosity characterization was performed by N_2 physisorption at -196 °C with a Micromeritics ASAP 2010 instrument (Micromeritics, Norcross, GA, USA). Specific surface area (SSA) of the samples was determined in the relative pressure (p/p_0) range between 0.05 and 0.30 using the BET equation. The total pore volume (TPV) was calculated as TPV= VαD, where Vα is the volume adsorbed at P/P_0 0.99, and D equals the density conversion factor (0.0015468) for the nitrogen gas as adsorbate gas. The assumption that the pores are open-ended and cylindrical is used. The average pore size is calculated using the equation 4000 TPV/SSA with the average pore size is given in nanometers.

2.2.3.2 FE-SEM Imaging

Microstructural characterization was performed by acquiring FE-SEM images of the fracture surface of PDC aerogels with a Zeiss supra 60 equipment (Carl Zeiss NTS GmbH, Oberkochen, Germany) operating in high-vacuum mode at 2.00 kV and after sputtering the samples with a thin gold film.

2.2.3.3 FT-IR Analysis

FT-IR spectra were recorded on a Bruker's ALPHA-P FTIR spectrometer in transmittance mode with a resolution of 4 cm^{-1}, and a scan time of 16 scans/s. Spectra were recorded between 4000 and 400 cm^{-1}. Prior to analysis, the samples were grinded using mortar and pestle.

2.3 Results and Discussion

2.3.1 Appearance

After aging in the digestion vessel, the samples appear white. The appearance does not change much after supercritical drying. The following figure illustrates a SiCO aerogel before and after supercritical drying.

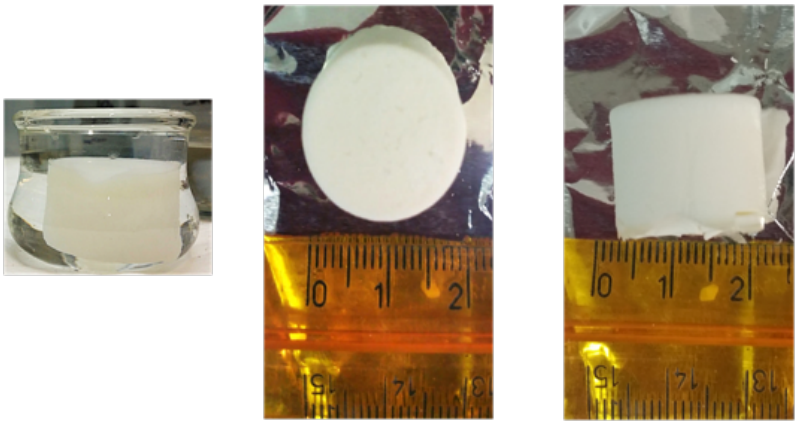

Figure 2-4 Aerogel before (left) and after (right) supercritical drying

2.3.2 Density and Linear Shrinkage

Extracting the solvent in the supercritical dryer causes significant shrinkage of samples. To account for the shrinkage, we measured the height and diameter of the (almost) cylindrical

samples before and after supercritical drying using a caliper. Bulk densities of samples were determined using measured volume and mass. As a caveat, these measurements carry a substantial error margin. Nevertheless, relative shrinkage and density data aligns with other quantitative data shown in Table 1 and displays two groups of polymer aerogels: samples synthesized in cyclohexane and THF exhibit linear shrinkage of over 30%, while samples synthesized in acetone and n-hexane contract only about 25%. Linear shrinkage correlates with bulk density of the aerogel. Densities of the first group (0.61-0.73 g/cm^3) are about twice as high as those of the second (0.27-0.38 g/cm^3). The shrinkage data agree with previous syntheses carried out using acetone and cyclohexane as solvents.[20] Necessary for the later discussion is the observation that in our experiments, the shrinkage occurs inside the CO_2 reactor already during the first washing with liquid CO_2. Although we cannot measure the linear dimension of the sample inside the reactor, we get the visual impression that supercritical extraction of CO_2 in the drying process does not cause further significant shrinkage, but that all changes in size happened before. The following table displays the density and linear shrinkage results.

Table 2-1 Density and Linear Shrinkage of PDC Aerogels

Sample	Density (g/cm^3)	Linear Shrinkage (%)
Cyclohexane-3 hours	N/A	N/A
Cyclohexane-6 hours	0.61	38
THF-3 hours	0.73	32
THF-6 hours	0.71	31
N-hexane-3 hours	0.28	26
N-hexane-6 hours	0.27	24
Acetone-3 hours	0.38	25
Acetone-6 hours	0.31	N/A

2.3.3 FT-IR Analysis

Decrease of the Si-H stretching band in the SiCO PDC aerogels

Hints to the kinetic progression of the reaction. The FT-IR analysis shows the decrease of the Si-H/Si-CH_3 with increasing reaction time, which suggests increased crosslinking or reaction or increased H_2 evolution when going from 3 to 6-hour gelation time. The stretching frequency for the C-H bond also is decreased upon crosslinking of PMHS with DVB.

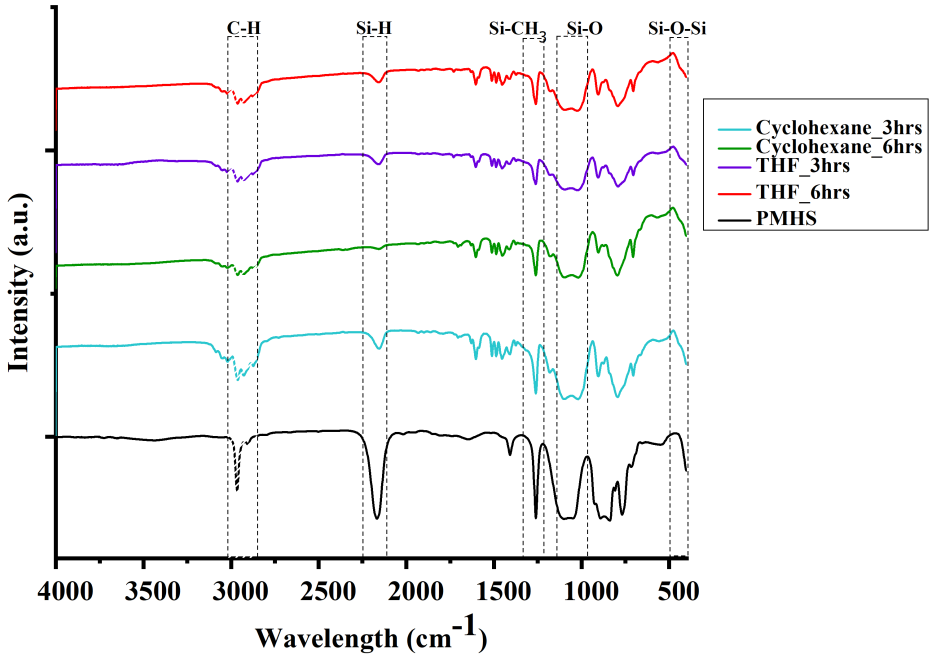

Figure 2-5 FT-IR spectra of SiCO PDC aerogels and precursor PMHS

The following table summarizes the results of the analysis of the FT-IR spectra displayed in the previous figure. The ratio of the integrated area of the Si-H/Si-CH_3 bonds is displayed below. Only data for cyclohexane and THF is displayed. The integrated area of Si-H/Si-CH_3 stretching frequencies decreases from 0.61 to 0.60 when gelation time is increased

from hours to 6 hours for the cyclohexane sample. For the THF sample, this ratio decreases from 0.50 to 0.30 when the gelation time is increased from 3 hours to 6 hours.

Table 2-2 FT-IR Results Including Peak Center, Integrated Area, and Ratio of Si-H/Si-CH_3 Stretching Frequencies

	Peak center (cm^{-1})	Integrated peak area	Integrated area Si-H/Si-CH_3
PMHS			
Si-CH_3	1261	1434.48	3.53
Si-H	2168	5067.14	
Cyclohexane-3hrs			
Si-CH_3	1261	1221.02	0.61
Si-H	2154	749.46	
Cyclohexane-6hrs			
Si-CH_3	1261	1268.04	0.60
Si-H	2158	757.95	
THF-3hrs			
Si-CH_3	1261	860.50	0.50
Si-H	2158	432.78	
THF-6hrs			
Si-CH_3	1261	1112.63	0.39
Si-H	2156	438.84	

2.3.4 N_2 Adsorption Analysis

Results of the porosimetry for the different samples with gelation time of 6 hours are given in Table 2-3. It is worth noting, that the porosimetry was performed only for samples synthesized with a 6-hour aging time. We find the highest Specific Surface Area (SSA) of 392 m^2/g for the aerogel synthesized in acetone, and the lowest SSA (120 m^2/g) for the aerogel synthesized in cyclohexane. The smallest average pore diameter in a sample is 6.4 nm (THF), and the largest is 25.7 nm (n-hexane). The highest pore volume of an aerogel is 1.99 cm^3/g using n-hexane as the solvent, and the lowest occurs for the aerogel synthesized in THF.

Table 2-3 N_2 Adsorption Analysis for SiCO PDC Aerogels

	N-hexane	Cyclohexane	THF	Acetone
SSA (m^2/g)	303	120	231	392
Porosity (cm^3/g)	1.99	0.59	0.43	1.82
Average Pore Diameter (nm)	25.7	14.7	6.4	18.8

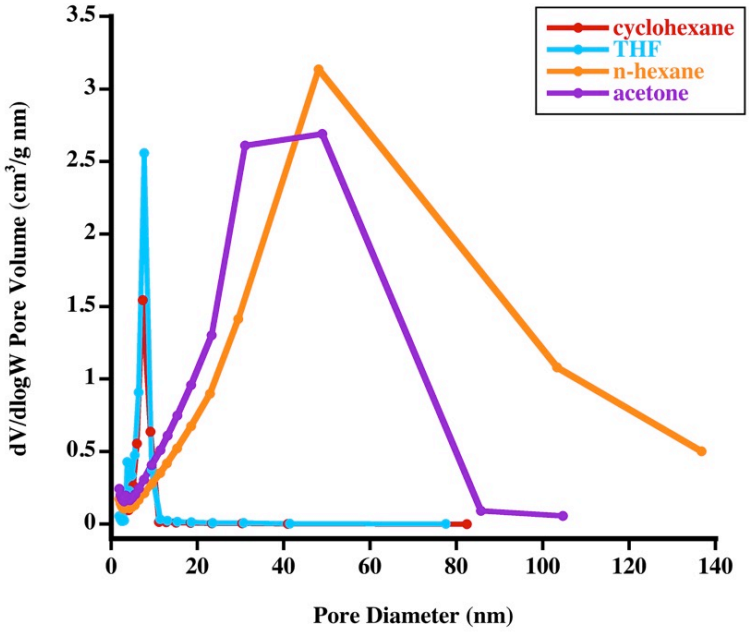

Figure 2-6 Pore size distribution of SiCO PDC aerogels (6 hour-aging)

The pore size distribution graphs for the SiCO PDC aerogels show that cyclohexane and THF have narrow pore size distributions and are smaller in average diameter. The n-hexane and acetone samples show larger average pore sizes as well as a broader pore size distribution. The isotherms for the SiCO PDC aerogels show that acetone and n-hexane adsorb a higher amount of nitrogen, in comparison to cyclohexane and THF. These results are consistent with the SSA calculated for the samples.

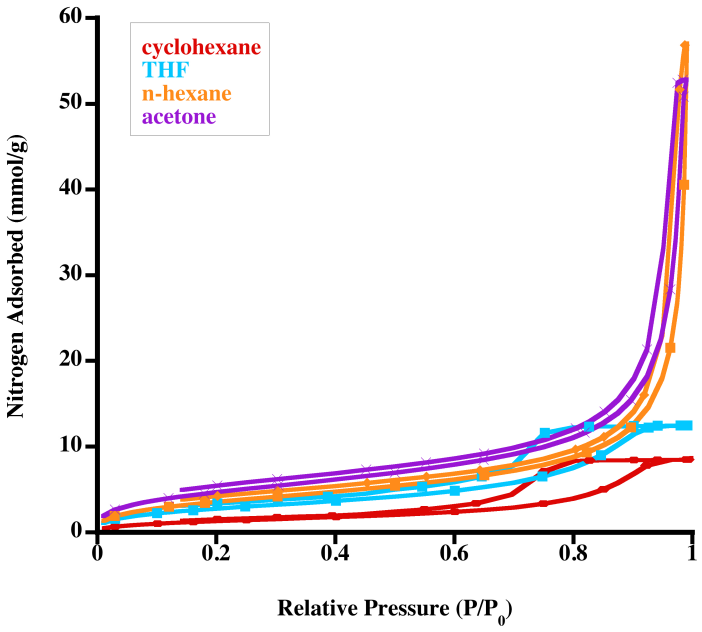

Figure 2-7 Isotherms of SiCO PDC aerogels (6 hour-aging)

2.3.4 FE-SEM imaging

FE-SEM pictures show microstructural results that are consistent with the values and trends. Samples obtained using cyclohexane or THF as solvent exhibit a denser microstructure and smaller pore sizes, consistent with the higher density. These results are complemented by small pore volume, small average pore diameter, and small specific surface area. On the other hand, samples synthesized in acetone and n-hexane display a more open porous microstructure, consistent with a lower measured density. Porosimetry of these samples yields larger pore volume, larger average pore diameter, and high specific surface area.

The observed porosities are typical for silica-based aerogels.[34] Pore and surface characteristics fall into the range of data reported for polymer aerogels from polysiloxane and polycarbosilane precursors.[23] In particular, our results are consistent with previous experiments of aerogels from PMHS and DVB.[20]

The following images show the FE-SEM images for PDC aerogels with 3-hour and 6-hour gelation time. The figures display the FE-SEM images, which show the formation of a

colloidal structure. The images show the comparison between the aerogels synthesized with the same solvent, but different synthesis times. FE-SEM for SiCO synthesized with acetone was only taken for the 6-hour gelation sample.

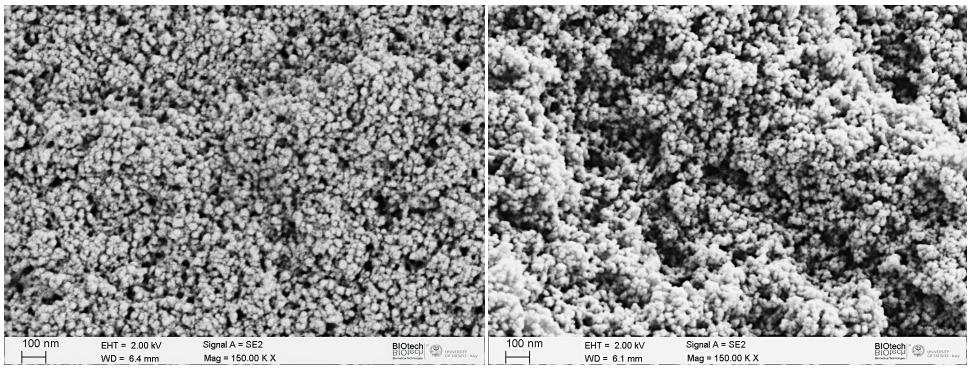

Figure 2-8 FE-SEM micrographs of SiCO aerogels synthesized with cyclohexane (to the left 3-hour aging time, to the right 6-hour aging time)

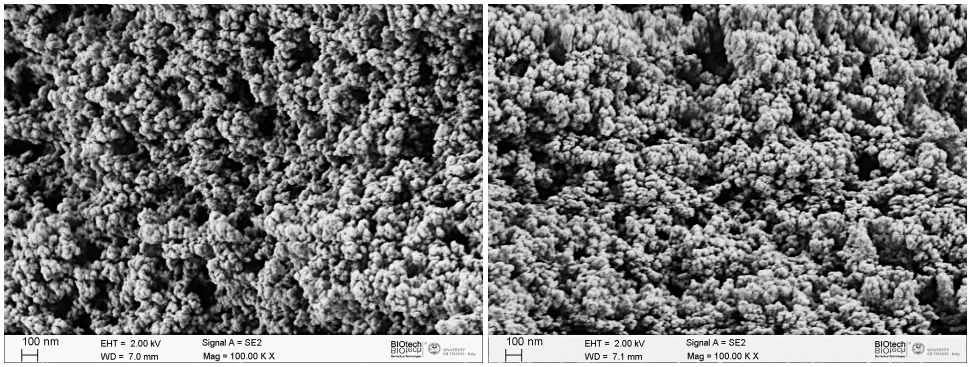

Figure 2-9 FE-SEM micrographs of SiCO aerogels synthesized with n-hexane (to the left 3-hour aging time, to the right 6-hour aging time)

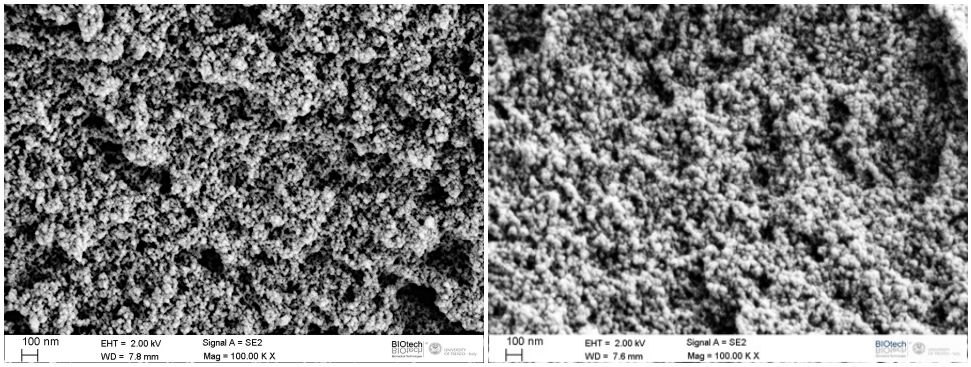

Figure 2-10 FE-SEM micrographs of SiCO aerogels synthesized with THF (to the left 3-hour aging time, to the right 6-hour aging time)

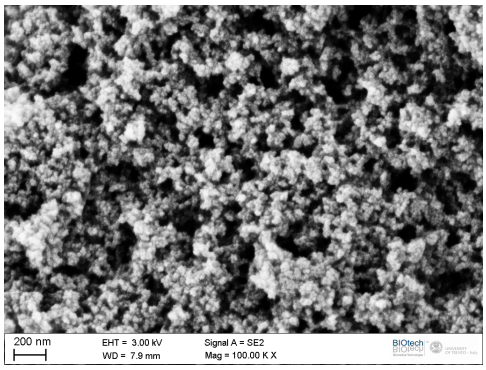

Figure 2-11 FE-SEM micrograph of SiCO aerogel synthesized with acetone (6-hour aging time)

There is no significant difference in the FE-SEM micrographs for the samples synthesized with 3 and 6 hours aging time using the same solvent. We will compare FE-SEM images of the samples that have the most distinct microstructural features and synthesized with a 6-hour aging time. These two samples are the samples synthesized with acetone and THF. In Fig. 2-12 we compare images for samples synthesized in THF and acetone. The porous microstructure of both polymer aerogels is typically explained by aggregation of small particles.[35-36] Results suggest that the aerogels were formed via the precipitation-polymerization mechanism. Precipitation-polymerization mechanism is the crosslinking of monomers or crosslinkers occurring in a homogeneous system. This formation eventually leads to

precipitation of the crosslinked polymer network. Particle sizes and pore diameters of the two samples are different; however, the sample synthesized in THF displays a finer microstructure in comparison to the coarser microstructure of the sample synthesized in acetone.

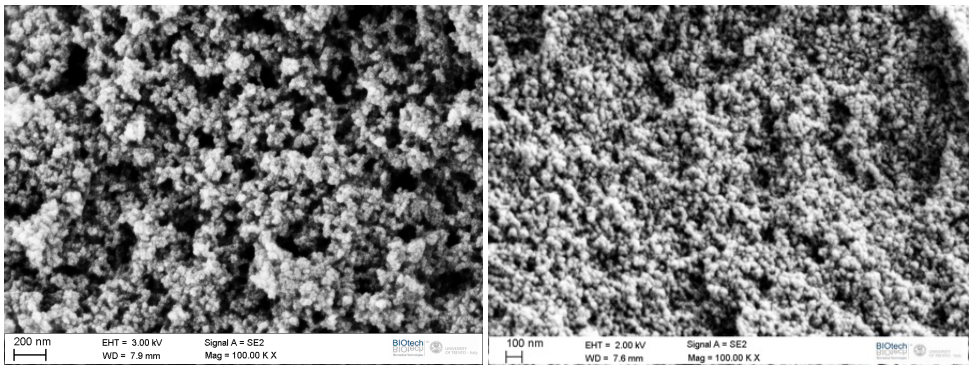

Figure 2-12 FE-SEM micrographs of SiCO aerogels synthesized with acetone (left) and THF (right). 6-hour aging time for both aerogels. Albeit the scale bar is different, the magnification is the same

2.3.5 TEM Imaging

The following TEM pictures give a qualitative appreciation of the pore size of the aerogels synthesized with acetone and cyclohexane with 6 hours of aging time. TEM images for the rest of the samples are not presented. The TEM pictures along with the FE-SEM micrographs help provide an approximation of the acetone sample pore size ranging from 20-30 nm, and for cyclohexane to be from 15 to 20 nm. In the FE-SEM pictures, it is possible to see a denser structure for the cyclohexane sample; this is consistent with the following TEM pictures.

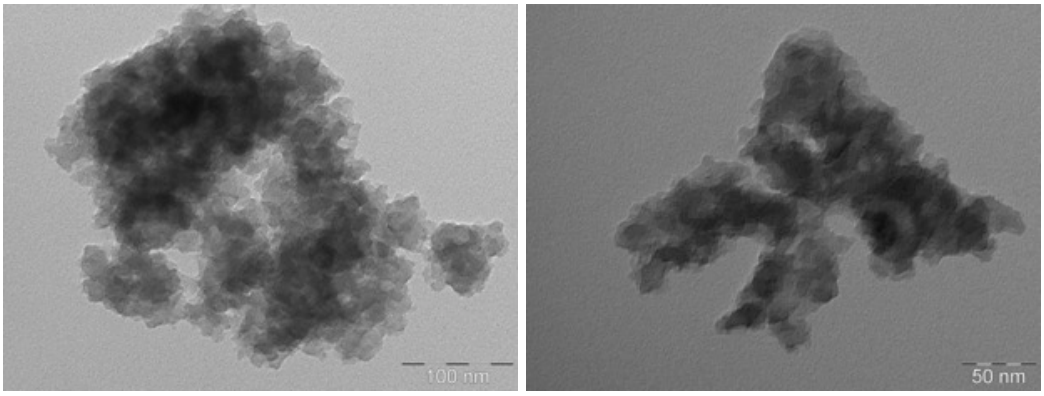

Figure 2-13 TEM pictures of SiCO PDC aerogel synthesized in acetone (6-hour aging) showing an approximate pore size of 20-30 nm in diameter

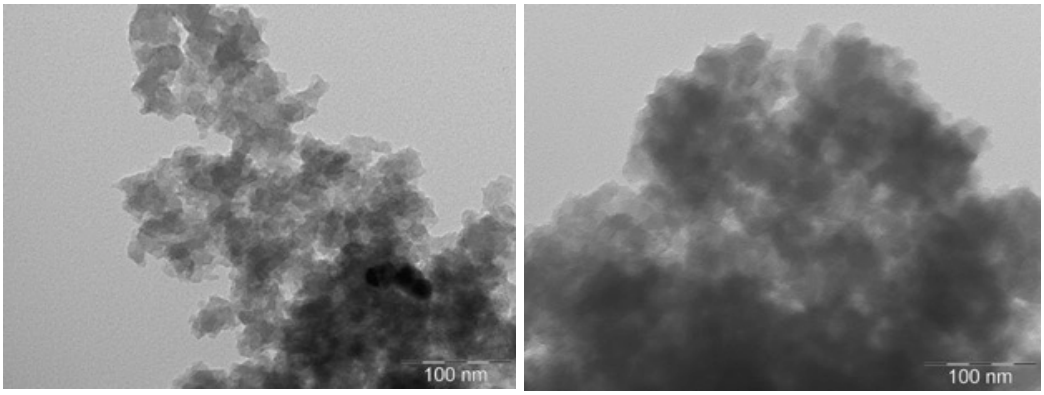

Figure 2-14 TEM pictures of SiCO PDC aerogel synthesized in cyclohexane (6-hour aging) showing an approximate pore size of 15-20 nm in diameter

2.3.6 Relating SSA to Solvent Properties

The use of solvents to modify and control the porosity of aerogels is well documented in the literature.[2, 18] Solvents impact reaction rates during gel formation, capillary stresses during drying, and, ultimately, the structure of final products. Solvents are used for the extraction of gels and to modulate the capillary stresses caused during drying. Mixtures of polar and non-polar solvents have been used to modify pore structures of silicon oxycarbide xerogels.[18]

In search of a rationale for the observations collected in Table 2-3, we related various solvents properties to the aerogel characteristics (SSA, average pore diameter, pore volume). We tested viscosity and solubility of solvents, polarity index and vapor pressure, no trend was seen in the surface morphology of aerogels (SSA, average pore diameter, and porosity). The only trend found was for solvent characteristics and vapor pressure. Vapor pressure of solvent correlates best with SSA of the aerogel. These results indicate that solvent parameters influence the development of the nano and microstructure of SiCO aerogels when the synthesis is started with the same preceramic materials and composition. However, vapor pressure alone does not offer a rationale to explain the observed trends.

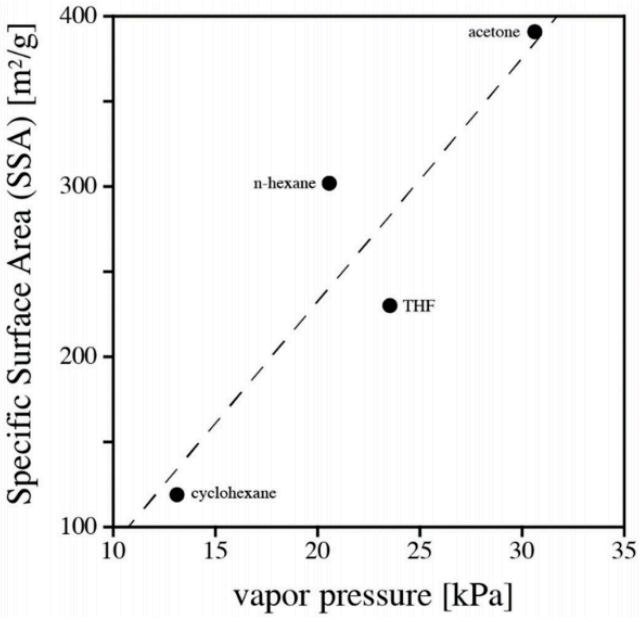

Figure 2-15 Specific Surface Area (SSA) plotted as a function of vapor pressure (at 25 °C) of solvent for the four solvents used in this study

We became more successful by considering the solubility of the PMHS/DVB polymer system in the respective solvent. Solubility is intertwined with the degree of swelling of a

polymer network in a solvent. We used solubility and swelling concepts, to provide a rationale for porosity and surface characteristics of the PMHS/DVB polymer aerogels. Solubility of polymers is best described using Hansen's approach to solubility.[37] [38] The three Hansen parameters, δ_d, δ_p, and δ_h, provide a semiquantitative measure of nonpolar (δ_d), polar (δ_p), and hydrogen-bond (δ_h) interactions for a system. They span the three-dimensional Hansen Solubility Parameter (HSP) space, and any molecular compound is represented by a point in HSP space. Mutual solubility is quantified by the distance R_A between two compounds (index 1 and 2) in HSP space: $R_A = 4(\delta_{d_1} - \delta_{d_2})^2 + (\delta_{p_1} - \delta_{p_2})^2 + (\delta_{h_1} - \delta_{h_2})^2$. Essentially, for a specific solute, a "good" solvent is found in short distance R_A, while a "bad" solvent has a large R_A. The set of "good" solvents for a given solute falls within a sphere, termed Hansen sphere, while solvents considered "bad" are located outside that sphere. Note that the radius of Hansen spheres of different solutes can be different. Moreover, since the parameters are related to Gibbs energies, Hansen spheres ultimately depend on temperature and pressure.

Table 2-4 Hansen Parameters (units $MPa^{0.5}$) of Solvents Used in this Study.[17] δ_T is the Total Solubility Parameter, $\delta_T^2 + \delta_d^2 + \delta_p^2 + \delta_h^2$

Solvent	δ_T	δ_d	δ_p	δ_h
cyclohexane	16.8	16.8	0.0	0.2
tetrahydrofuran	19.4	16.8	5.7	8.0
acetone	19.9	15.5	10.4	7.0
n-hexane	14.9	14.9	0.0	0.0

For solvents used in this study, Hansen solubility parameters are listed in Table 2-3. Unfortunately, no solubility parameters exist of the PMHS/DVB system. We estimate the parameters from small molecule data (e.g., styrene) and data for polydimethylsiloxane (PDMS). Hansen parameters of styrene are $\delta_d = 18.6$, $\delta_p = 1.0$, $\delta_h = 4.1$.[39] Multiple parameters have been reported for PDMS, for which solubility in organic solvents depends on the degree of cross-

linking (molecular weight) and temperature. For a high-weight (long-chain) PDMS polymer Hansen parameters of $\delta_d = 17$, $\delta_p = 4$, $\delta_h = 4$ have been suggested.[40] Combining data for styrene and PDMS, we find that solubility parameters of the PMHS/DVB system likely fall into the range $\delta_d = 17\text{-}18.5$, $\delta_p = 1\text{-}5$, $\delta_h \approx 4$, with some uncertainty about the exact values. It turns out that even with this uncertainty, the distinction between THF and cyclohexane as solvents for the PMHS/DVB system on one side, and acetone and n-hexane on the other side, are well explained by their respective distance R_A to PMHS/DVB in HSP space. Assuming a simple average of PDMS and styrene, we obtain solubility parameters for the PMHS/DVB polymer system of $\delta_d = 17.8$, $\delta_p = 2.5$, $\delta_h = 4.0$. Using these values, R_A to cyclohexane, THF, acetone, and n-hexane, is 5.0, 5.5, 9.6, and 7.5 respectively — and a clear distinction between cyclohexane and THF on one side, and n-hexane and acetone on the other side emerges. Variations of the parameters for PMHS/DVB within the proposed range do not change the grouping. Consequently, we establish that cyclohexane and THF are better solvents for PMHS/DVB than acetone and n-hexane. For the rest of our discussion, we may call them "good" and "bad" solvents, respectively.

However, how does solubility of the polymer impact pore formation in the corresponding aerogel? We emphasize here the importance of swelling of a polymer for pore modification of an aerogel. Swelling of a polymer and its solubility in a solvent are intertwined. Indeed, swelling data is used to determine solubility parameters.[41] [42] There is ample evidence in polymer chemistry that the higher the solubility, the higher is the degree of absorption of the solvent into the polymer and, as a consequence, the higher is the swelling of the polymer. Swelling happens for hydrogels (e.g. used in diapers). Linear swelling of a siloxane polymer (e.g. PDMS) can differ by more than a factor of 2 depending on the solvent. [43]

To provide a rationale for pore formation with swelled polymers, we assume that the size of precipitating microgel particles, their "radius of gyration," depends only on the polymer itself and is independent of the solvent used. Hence, the characteristic size of the microgel

particles is the same in all our experiments, no matter whether we use acetone or THF as solvent. Since a good solvent causes a high degree of swelling, the volume content of a “good” solvent – alternatively, the better swelling agent – within a gel particle is larger than that of a “bad” solvent. If the solvent is removed, the microgel particles shrink, and the higher the degree of swelling, the higher the particle shrinkage. The concept of microgel particle formation and shrinkage is illustrated in Fig. 2-16. This model agrees with the data of linear shrinkage in Table 2-1: the higher shrinkage occurs for the “good” solvents, THF and cyclohexane, and lower shrinkage is observed for the “bad” solvents. Since the wet gel is build up by coalesced particles, the smallest particles, which originated from the better swelling agent, build-up the structure with smallest average pore diameter. This conclusion agrees with the observed average pore diameters in Table 2-2. Since the PMHS/DVB polymer aerogels are essentially build up by similar units in the same way, and the only difference after solvent extraction is the size of the gel particles, a simple scaling yields that structures with larger shrinkage and smaller pore diameter also have the smaller SSA. This consequence should not be confused with trends according to which smaller particles yield higher SSA. SSA is a quantity specific per unit mass, and not per unit volume. According to the data in Table 2-1 polymer aerogels’ densities in this study differ by up to a factor of two. If indeed we are looking for the surface area per volume of sample, then we find that THF yields the highest surface area per volume of polymer aerogel.

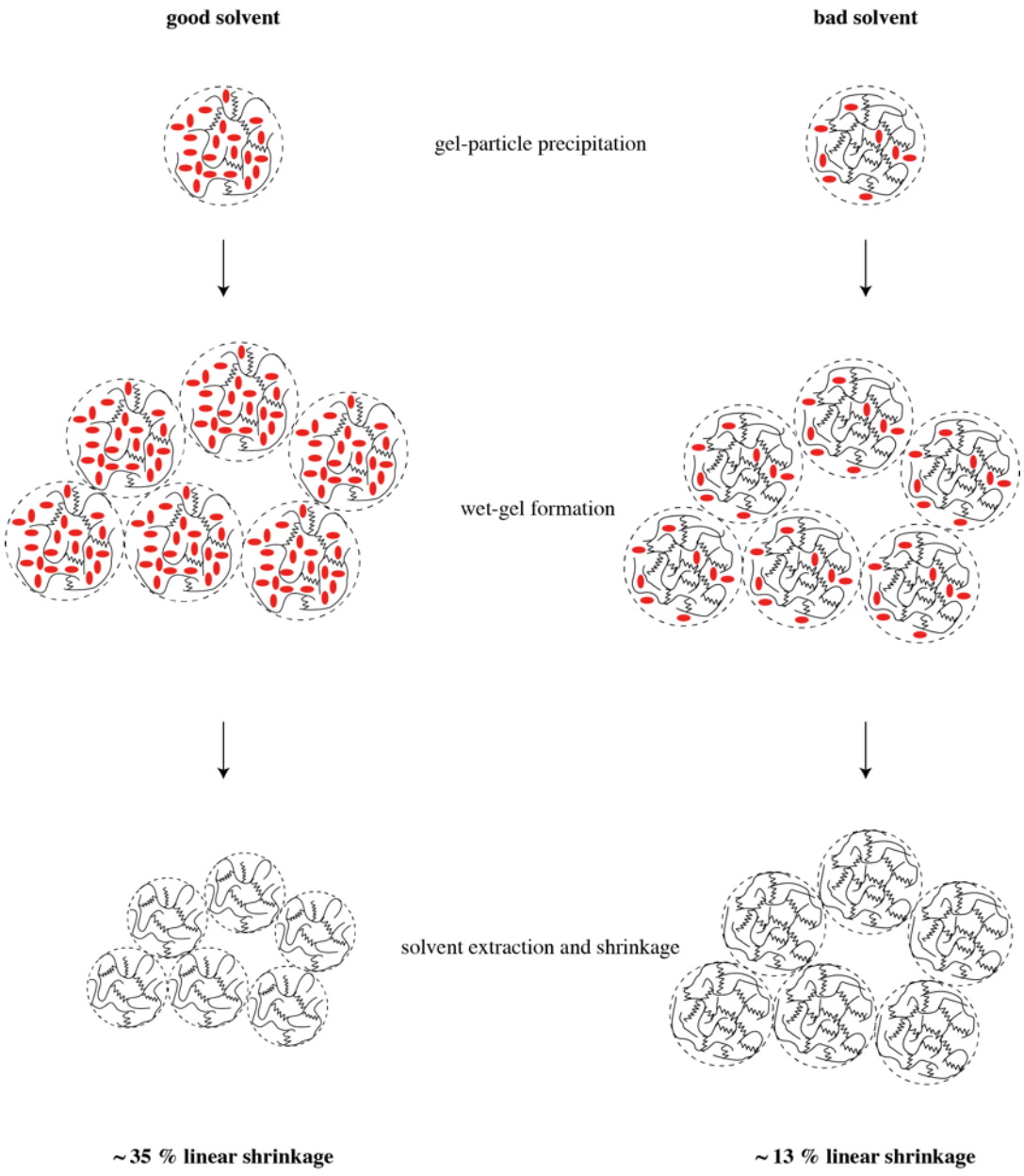

Figure 2-16 Illustration of microgel particle formation and shrinkage for PMHS/DVB polymer aerogel formation in a “good” solvent such as cyclohexane (left) and a “bad” solvent such as acetone (right). Solvent molecules are depicted in red; polymer strands are shown as black lines

The three solvent characteristics, namely vapor pressure, Hansen solubility parameters, and ability to swell a polymer, are strongly correlated. Only recently, Rumens et al. provided a fine study highlighting the connection between Hansen solubility parameters, vapor pressures of organic solvents, and the resulting degree of swelling of a polymer network based on PDMS.[44] Therefore, the correlation shown in Figure 2-16 only conforms to the discussion of solubility and swelling.

There may, however, be alternative paths available to explain the porosity and its relation with solubility. For instance, following standard arguments of the precipitation-polymerization mechanism, a good solvent will cause the formation of larger particles before precipitation, while a bad solvent causes small particles.[45] We would expect acetone and n-hexane to yield the smaller particle, and THF and cyclohexane to form the larger, which appears to contradict the FE-SEM observation in Fig. 2-12.

Moreover, without fundamental differences in the particle's internal structure, the larger nuclei will result in the larger pore size diameters, since the interstices between the nuclei are larger as for smaller nuclei as well. Smaller nuclei, produced using a "bad" solvent (acetone, n-hexane in our case) would produce smaller pore size diameters. This explanation, however, is in opposition to the observed data in Table 2-2. Consequently, a precipitation- polymerization mechanism does not seem to apply in our case.

Another concept is frequently invoked for porous co-polymeric resin (PCR) materials. [46-47] As a general guide, "good" and "bad" solvent porogons separate from polymer particles at different stages of the polymerization. "Bad" solvent porogons separate early, which allows microgel particles to fuse and aggregate quickly, resulting in a coarsening of the morphology. This yields pores with large average diameter and resins with rather low SSA. "Good" solvent porogons, on the other side, separate late and microgel particles retain more of their individuality. Average pore diameters are then lower, and SSA of such resins is larger. While porosity of many porous resin materials synthesized via suspension polymerization can be

tailored following this reasoning,[47] the explanation does not apply for the PMHS/DVB system we study. To provide further support for our hypothesis or to disprove it, we propose experiments that yield information about the size of the microgel particles during structure formation, for example, static and dynamic light scattering.[48-49] A synthesis approach will be to exchange "good" and "bad" solvents during the synthesis procedure to investigate, which step is most responsible for forming the morphology of the porous material.

2.4 Conclusion

Results show that the solvent influences porosity, average pore size, and specific surface area. The different gelation times did not show a significant difference in the structure of the SiCO aerogels. The vapor pressure of solvents has an impact on the SSA of the SiCO samples. The FE-SEM pictures show the colloidal gel structure of the aerogels, and the different microstructure obtained by changing the solvent. Characterization was done using FT-IR, TEM, SEM, BET, and BJH analysis. The maximum Specific Surface Area (SSA) obtained was 392 m^2/g for the aerogel synthesized with acetone with 6 hours. Average pore diameter ranges from 6.4 nm to 26.5 nm, and maximum porosity was 1.99 cm^3/g for the aerogel with n-hexane as solvent.

Results indicate that pore formation and control of pore morphology in processing PMHS/DVB polymer aerogels is strongly related to solubility and swelling of the polymer during synthesis. Our results show that the solvent influences porosity, average pore size, and specific surface area in a particular way, which is not explained by common pore- formation concepts. We outline a new hypothesis for pore formation of polymer aerogels synthesized by PMHS/DVB, which invokes solubility and swelling of a polymer. Further experiments in aerogel synthesis, in particular with mixtures of solvents, are needed to provide additional validation to it.

2.5 Acknowledgement

This work was supported by the National Science Foundation (NSF) through awards CMMI 1634448 and OISE-1743701.

Chapter 3

Synthesis of Ambient Dried SiCO Materials and Their Potential for Environmental Remediation

Abstract

Highly porous silicon oxycarbide ceramics were synthesized using sol-gel precursors. Annealing of these materials in inert atmosphere leads to SiCO ceramics. The sol-gel method and the polymer-derived ceramic (PDC) method allow for the synthesis of ceramic structures that are not attainable by typical solid-state methods.

The synthesis method involves hydrolysis and condensation reactions to obtain a cross-linked gel, which is slowly dried at 45 °C to obtain a porous material. Then, the porous SiCO materials are transformed via thermal treatment in a controlled atmosphere into SiCO ceramics. Characterization of adsorption efficiencies of porous SiCO, mesoporous silica, and activated carbon was evaluated. Porous SiCO had outstanding adsorption ability towards methylene blue (MB) organic dye in comparison to mesoporous silica and activated carbon. UV-Vis spectroscopy was used to monitor the disappearance of the characteristic absorbance peak of the dyes. SiCO shows about 90% adsorption towards MB in 15 minutes of contact time.

SiCO ceramic, mesoporous silica, and activated carbon's specific surface area (SSA), pore size distribution, average pore size, and total porosity were investigated using N_2 adsorption analysis. It was observed that the microstructural properties of SiCO materials are crucial for their performance in cleaning of organic dyes, but results indicated that the highest SSA is not the most important characteristic in the adsorption of dyes in these materials.

3.1 Introduction

Porous silicon oxycarbide ceramics are synthesized using sol-gel precursors[50], and polymer precursors. Porous silicon oxycarbide glasses have been made using methods such as sacrificial templating, HF etching, and others. These methods are covered in recent review papers.[51-52] These materials can contain a hierarchical porous structure.[53] Annealing of these materials in inert atmosphere leads to SiCO ceramics. The sol-gel method and the PDC method allow for the synthesis of ceramic structures that are not attainable by typical solid-state methods. SiCO structure is composed of an amorphous network of mixed silicon units SiC_xO_{4-x}, with $0<x<4$ where silicon is bonded to oxygen and carbon atoms.[54]

The chemical composition of these materials can be controlled by choice of synthesis conditions such as precursors options, annealing temperatures[55] and atmospheres.[27, 56] For example, adequate selection of precursors ratios and molecular structure allows synthesis of SiCO materials with a variety of compositions including stoichiometric ratios.[28, 57]

Recently, SiCO ambient dried (ambigels) were synthesized using the sol-gel synthesis method.[25] SiCO ambigels were synthesized from bis (triethoxysilyl) methane and bis (tryethoxysilyl) ethane and dried at ambient pressure at low temperatures.[27]

Reclaiming water and providing access to clean water are grand challenges for science and engineering. Human-made contaminants and industrial effluents are major environmental concerns. Production and disposal of synthetic chemicals from industries, agriculture, and general human activities increase at a faster rate than any other current environmental issue.[58] Quantity and variety of pollutants in textile wastewater is broad as it can include several dyes, detergents, and additives.[59] Specifically, dyes are used in several industries, including paper, dying, paint, pulp, tannery, and manufacturing. More than half of the dye in wastewater is released by the textile industry. Adsorption of water contaminants is a commonly used purification process. This relatively simple process is economically more feasible in comparison to oxidative processes, electrocoagulation, membrane separation, and others.[60]

In this study, the removal of cationic dyes using porous SiCO, mesoporous silica, and activated carbon was investigated using methylene blue (MB) solution.

3.2 Experimental

3.2.1 Chemicals

SiCO materials were synthesized using 1,2-Bis(triethoxysilyl) ethane (BTEE). BTEE was purchased from Sigma Aldrich and was used without any further purification. Mesoporous silica (28,860-8) was purchased from Aldrich Chemical Company, Inc, and activated charcoal (7631-86-9) was purchased from Sigma-Aldrich (100 particle size mesh). Methylene blue (MB) was purchased from Merck, Germany. These were used without any further purification. Distilled water was purified with Milli-Q water purification system to 18 MΩ (Millipore, Billerica, MA). 3M HCl and isopropanol were obtained from Macron Fine Chemicals and EMD Millipore.

3.2.2 Synthesis of SiCO Ambigels

Ambient dried porous SiCO materials were synthesized using 1,2-Bis(triethoxysilyl) ethane (BTEE). Following the synthesis outlined in Dire et al.[27] BTEE was dissolved in isopropanol and stirred until the solution appeared completely homogenous. 3M HCl was added dropwise to achieve a molar ratio BTEE: isopropanol: HCl of 1:5:0.006. After addition of HCl, the solution was stirred and placed in an oven to dry at low temperatures (40 °C to 50 °C) for 60 days. Subsequently, ambient-dried SiCO was annealed in a tube furnace under Argon flow (high purity Argon, Airgas Company). The heating rate was 5 °C/min up to 400 °C, followed by a holding of 2 hours at 400 °C. The temperature was further raised to 1000 °C with a rate of 5 °C/min and kept for 4 hours at 1000 °C. Subsequently, the furnace was shut off, and the material was cooled to ambient conditions.

3.2.3 Characterization Procedure

3.2.3.1 TGA Analysis

A Shimadzu TGA-50H was used to investigate the polymer to ceramic conversion of the SiCO ambigel. Analysis was performed in a platinum crucible in nitrogen atmosphere, with gas flow of 20 mL/min, and a heating rate of 5 °C/min up to 900 ºC.

3.2.3.2 FE-SEM Characterization

FE-SEM characterization of SiCO sample was done in a Hitachi S-4800 II FE-SEM. Fracture surfaces of the SiCO material were studied. Prior to imaging, samples were coated on a CRC-100 sputtering system using a carbon target with two-minute sputtering time.

3.2.3.3 TEM Imaging

TEM imaging for the SiCO sample was done in a Hitachi H-9500 High-resolution TEM (Transmission Electron Microscope), which is a high-resolution microscope with an accelerated voltage of 300 kV.

3.2.3.4 Nitrogen Adsorption Analysis

Nitrogen adsorption analysis was performed at 77 K using an ASAP 202 Micromeritics Instrument (Micromeritics, Norcross, GA). Ambigel samples were degassed using an evacuation ramp rate of 10 °C/min up to 90 °C. We used an evacuation rate of 5 mmHg/s with a vacuum setpoint of 10^{-3} mm of Hg. To calculate specific surface area, we apply the BET equation (SSA_{BET}) using a molecular cross-sectional area of 0.1620 nm^2 and a correlation coefficient of 0.9571864. Pore size distribution and average pore diameter are obtained from the desorption branch of the isotherm using the BJH model using the Faas correction and Halsey thickness curve.[61-62] Micropore surface area was obtained using the t-plot method.

3.2.3.5 UV-Vis Absorption Analysis

For the investigation of dye adsorption, UV-Vis absorption characterization was performed using a UV-VIS-NIR spectrophotometer (Shimadzu UV-3600). A stock solution of 10 ppm methylene blue (MB) (Merck, Germany) was prepared using Millipore DI water. The

solution was prepared so that it fulfills Beer's Law to ensure linearity. No further changes were made to the stock solution.

Solution pH was 5 during the performance of the experiments. The temperature throughout the experiments was 20 °C. In an initial experiment, 100 mg of powdered porous SiCO material was added to 100 mL of MB solution (100 mL of a 10 ppm MB solution corresponds to 1 mg of MB dye). After overnight stirring, 1 mL aliquot was taken from the vessel, and the solution was centrifuged at 17800 rpm for 10 minutes. The supernatant was analyzed using UV-Vis spectrophotometry, and after stirring the solution overnight at room temperature, we found no significant absorption in the visible range remaining of the solution. With this initial result; it was estimated that porous SiCO has a specific adsorption greater than 10 mg/g, but more detailed experiments needed to be performed.

For subsequent absorption experiments, we added 15 mg of porous material – either SiCO, porous silica, or activated carbon – to 50 mL of MB solution. The solution was magnetically stirred, and 0.5 mL aliquots were obtained at given time intervals. The aliquots were quickly (within 15 s) transferred to a UV-Vis spectrophotometer. We characterized the visible range between 400 and 800 nm (within 60 s), which shows an absorption maximum at λ_{max} = 664 nm for MB solutions. We calculated the relative absorbance according to $abs\ (\text{in}\ \%) = (A_0 - A)/A_0 * 100$. A_0 corresponds to the absorbance of the MB solution at λ= 664 nm before adding the porous material; A is the absorbance at λ= 664 nm after stirring for a determined time.

3.3 Results and Discussion

3.3.1 SiCO Ambigel TGA Analysis

Thermogravimetric analysis was performed under N_2 atmosphere up to a 1000 °C with a heating rate of 5 °C/min. TGA gives a residual mass percent of 85%. Experimental residual mass after annealing corresponds to 90%. The high percentage of residual mass is thought to be related to the sample's long drying times. The weight loss below 200 °C is reported to be

due to H_2O evolution and decomposition of Si-OEt moieties and the weight loss starting from around 400 °C is related to polymer to ceramic conversion process. [17, 63 64]

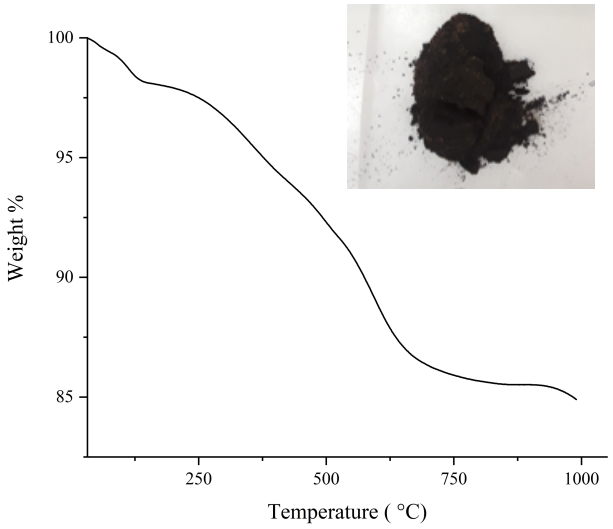

Figure 3-1 TGA analysis of SiCO ambigel performed in nitrogen atmosphere, inset corresponds to the digital image of resulting SiCO material

3.3.2 FE-SEM Imaging

The following images show the unannealed SiCO ambigel and the annealed SiCO ambigel. The FE-SEM image of the unannealed SiCO ambigel shows particle agglomeration and provides a general idea of the microstructural feature of the material. The structural features of the unannealed ambigel are defined by the particle arrangement. The following image displays the FE-SEM image of the unannealed material.

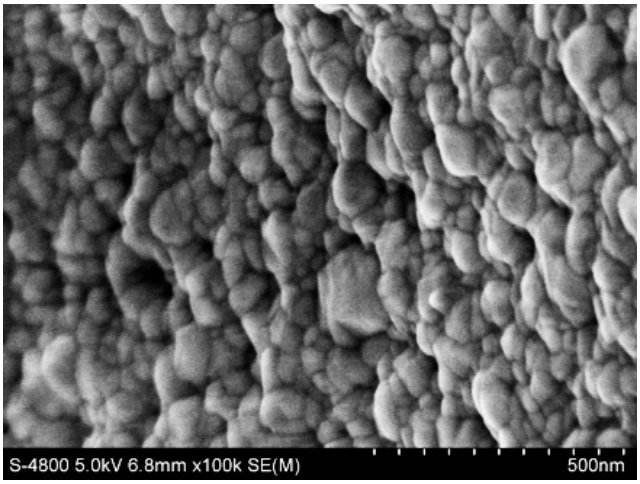

Figure 3-2 FE-SEM image of unannealed SiCO ambigel

The following images represent the annealed SiCO ambigel (1000 ºC in Argon). Materials were coated before FE-SEM imaging.

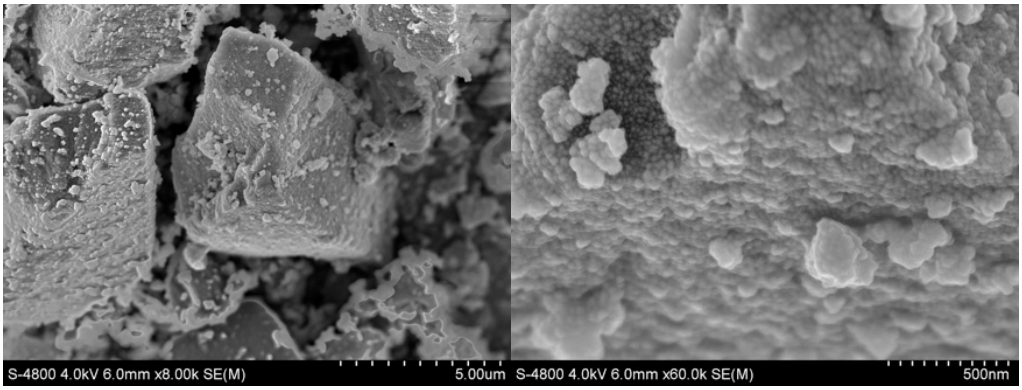

Figure 3-3 FE-SEM image of annealed SiCO ambigel (1000 ºC in Argon atmosphere)

Figure 3-14 shows the microstructural features of the SiCO ambigel material densified after the annealing process. Densification of SiCO materials after annealing is reported in literature papers and reviews.[51, 65]

3.3.3 TEM Imaging

TEM imaging of the unannealed SiCO material is shown before. TEM imaging provides qualitative insight into the structure of the material.

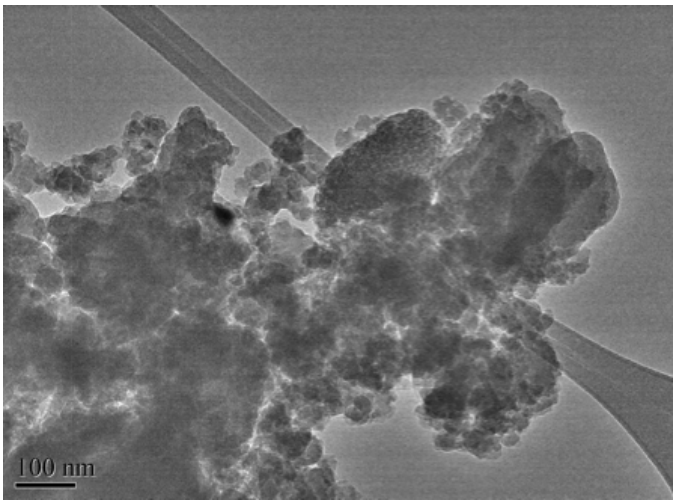

Figure 3-4 TEM image of unannealed SiCO material

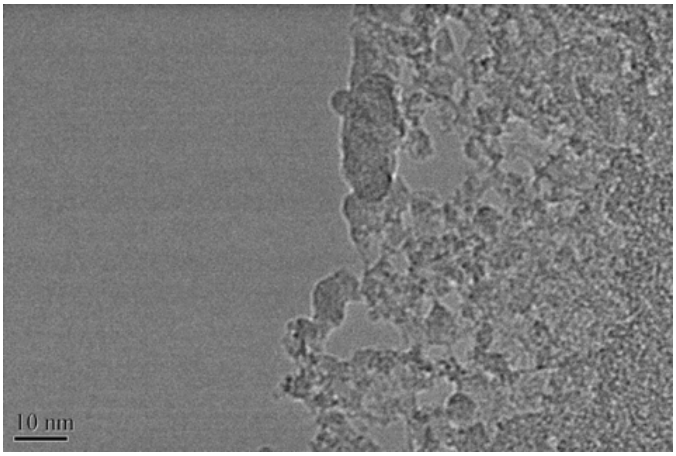

Figure 3-5 TEM image of annealed SiCO ambigel

One of the main differences between annealed and unannealed SiCO is the finer microstructure of the annealed material. The unannealed material appears more agglomerated and clumped together. Distinctive features are not very visible on high magnification. For the

annealed material, higher magnification provides insight into the porosity of the sample. The approximate particle size in the annealed material is around 10 and 30 nm.

3.3.4 Nitrogen Adsorption Analysis

The porosimetry analysis using nitrogen adsorption of porous SiCO, mesoporous silica, and activated carbon was done prior to their use in adsorption experiments. In Figure 3-6, the N_2 isotherms of the three materials are shown. Figure 3-7 displays the pore size distribution and figure 3-8 the cumulative pore volume. The gathered microstructural information is summarized in Table 3-1.

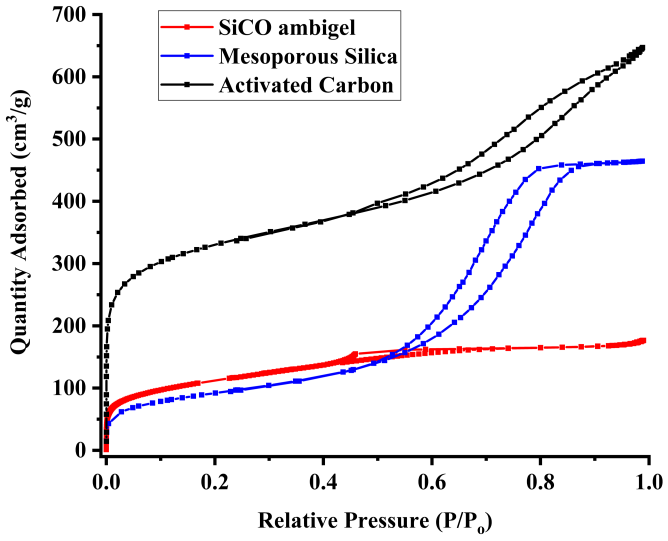

Figure 3-6 Nitrogen isotherms for SiCO ambigel, mesoporous silica, and activated carbon

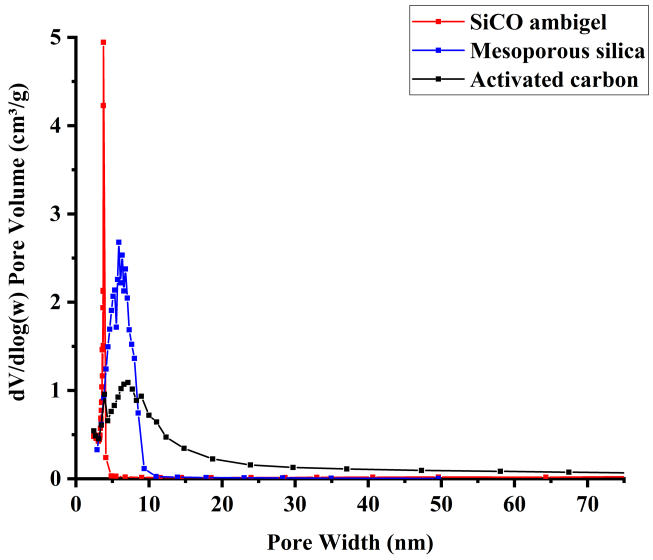

Figure 3-7 Pore size distribution dV/dlog (w) vs. pore width (nm) for SiCO ambigel, mesoporous silica, and activated carbon

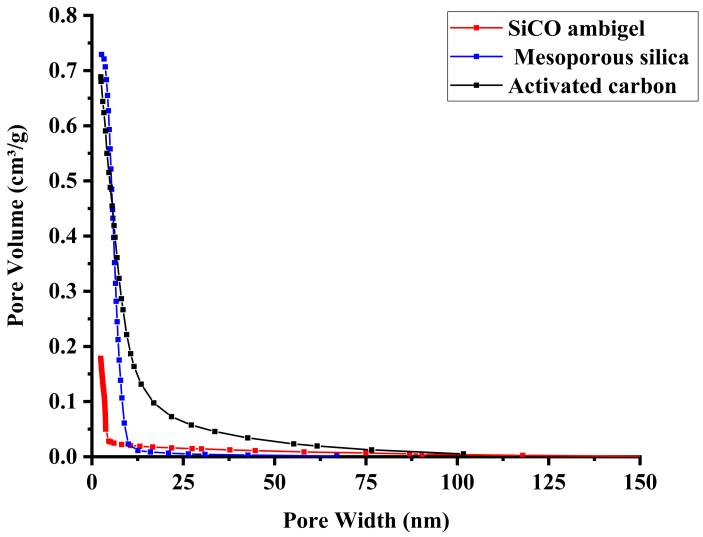

Figure 3-8 Cumulative pore volume (cm^3/g) vs. pore width (nm) calculated using the BJH method from the desorption branch of the isotherm

According to the 1985 IUPAC recommendations, physisorption isotherms were sorted into six types. These six isotherm types have been updated in the last 30 years as new isotherm characteristics have been identified.[66] Considering the updated IUPAC classification. We have identified the isotherms presented here for further analysis of the results. Isotherms for SiCO, mesoporous silica, and activated carbon are presented in Figure 3-1.

The isotherms for all samples display a hysteresis loop. Hysteresis loops occur in the multilayer adsorption process present in an isotherm and are associated with capillary condensation. All isotherms resemble isotherm IV (a) more closely. This type of isotherm is given by mesoporous materials such as porous oxides and molecular sieves. In mesoporous materials, the adsorption behavior is defined by the adsorbent-adsorptive interactions as well as the condensed state molecule interactions. One representative feature of type IV isotherms is a final saturation plateau which can be of different lengths, or it can be an inflection point.[66]

There are many different shapes of hysteresis loops. In the original IUPAC classification from 1985, there were four hysteresis types identified[67], but this list has grown due to recent findings. Currently, there are six IUPAC hysteresis loop types associated with specific pore structural features and adsorption mechanisms.[66] The hysteresis loop that is most resembled by SiCO sample is H2(a) hysteresis loop. H2 hysteresis loops are given by complex pore structures in which network effects are significant. H2(a) has a steep desorption branch caused by pore blocking or percolation present in a narrow distribution of pore necks. From the pore size distribution, it is possible to see that the SiCO sample possesses a narrow pore size distribution around 3 nm. This description is consistent with the IUPAC hysteresis loop H2(a).

The hysteresis loop exhibited by mesoporous silica resembles the H2(b) hysteresis loop. This hysteresis loop is seen for samples that display pore-blocking with large neck width size distributions. Some materials that display these features are mesocellular silica foams, some hydrothermally treated mesoporous ordered silicas.

Activated carbon exhibits a hysteresis loop similar to the H4 IUPAC hysteresis loop. A feature of this hysteresis loop is a pronounced nitrogen adsorption uptake at low pressures due to the presence of micropores. These loops are often seen for some zeolites, crystalline and mesoporous zeolites and micro and mesoporous carbons.[66] Figure 3-4 and figure 3-5 display IUPAC isotherm and hysteresis loop IUPAC classification.

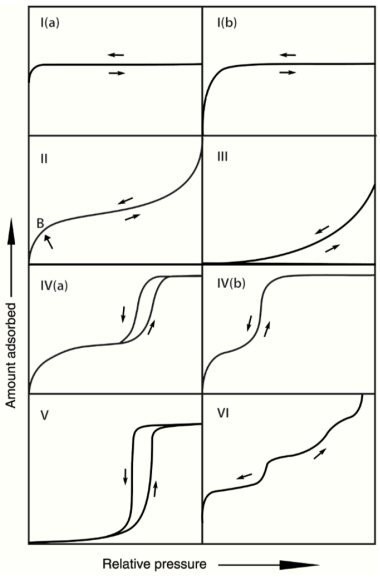

Figure 3-9 IUPAC classification of isotherms using adsorption analysis

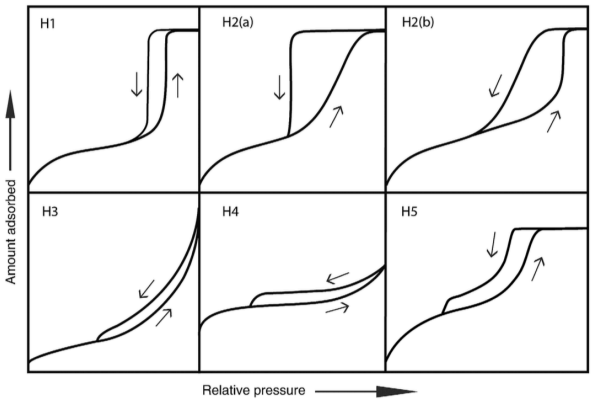

Figure 3-10 IUPAC classification of hysteresis loops encountered in physical adsorption

Methods for the determination of surface area, pore volume, average pore diameter, and pore size distribution include using physical adsorption. Most models assume uniform pore shapes. Figure 7 exemplifies standard simple pore models.

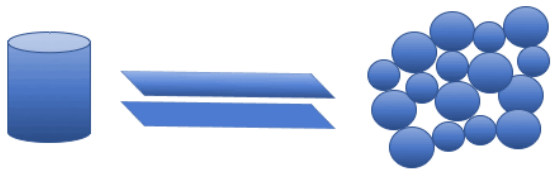

Figure 3-11 Examples of simple pore models (from left to right): cylinders, slits, and voids

In actual porous solids, the pore structure is generally more complex and irregular. Figure 8 displays some pore possibilities. These pore structures are encountered in more complex porous materials. That is why it is important to keep in mind that actual microstructural features of materials can be a combination of pore/sizes and shapes.

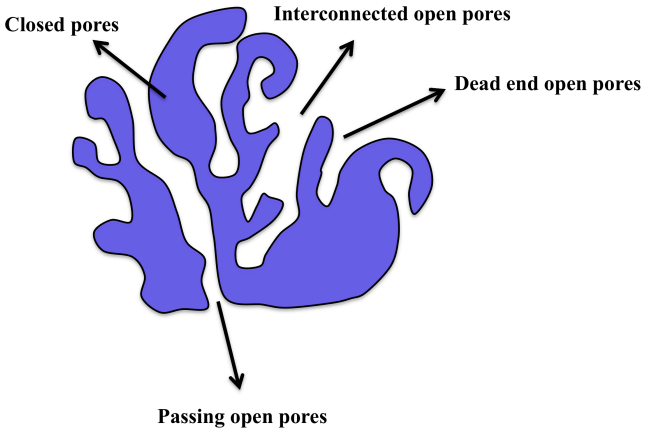

Figure 3-12 Open and closed pore types present in porous solids

The following table summarizes the results of the nitrogen adsorption analysis for porous SiCO, mesoporous silica, and activated carbon.

Table 3-1 Summary of Specific Surface Area, Average Pore Diameter and Porosity Calculated using N_2 Adsorption Analysis

	Porous SiCO	Silica	Activated carbon
Brunauer-Emmett-Teller Analysis			
BET Surface Area (SSA_{BET}) (m^2/g)	274	332	587
Desorption average pore width (4V/A by BET) (nm)	3.9	8.7	6.8
Barret-Joyner-Halenda Analysis			
Mesopore volume (cm^3/g)	0.17	0.73	0.64
Average mesopore diameter (nm)	3.9	6.0	6.5
t-plot			
Micropore Area (m^2/g)	-	27	-

3.3.5 Absorption Results

Initial experiments of MB adsorption using 100 mg of SiCO and 100 mL of 10 ppm MB solution are displayed below in Figure 3-13. These results are after overnight stirring and centrifugation at 17800 for 10 min.

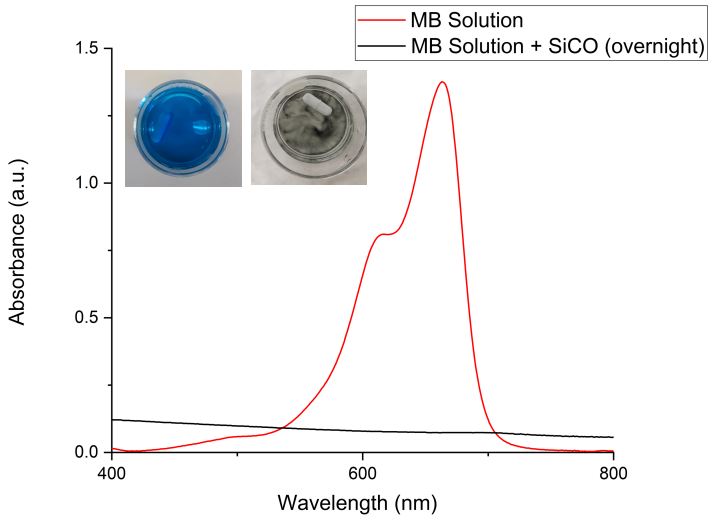

Figure 3-13 UV-Vis spectra of 10 ppm of MB solution before and after overnight stirring with porous SiCO

Initial results show that MB solution displays no characteristic peak of the MB dye after overnight contact with the porous SiCO material. Further adsorption studies were conducted using solutions of MB organic dye into which the absorbing material, porous SiCO, mesoporous silica, or activated carbon, is added. Adsorption is measured as a function of contact time to examine the maximum capacity. To illustrate the adsorption process that goes along with a decrease of color intensity, we show digital images of the initial MB stock solution and the development of the solution with time after adding porous SiCO in Figure 3-14.

Digital pictures for this process were taken before the start of the experiment, with only MB solution, and then SiCO ambigel was added to the solution, and the color change progression was followed at specific time intervals.

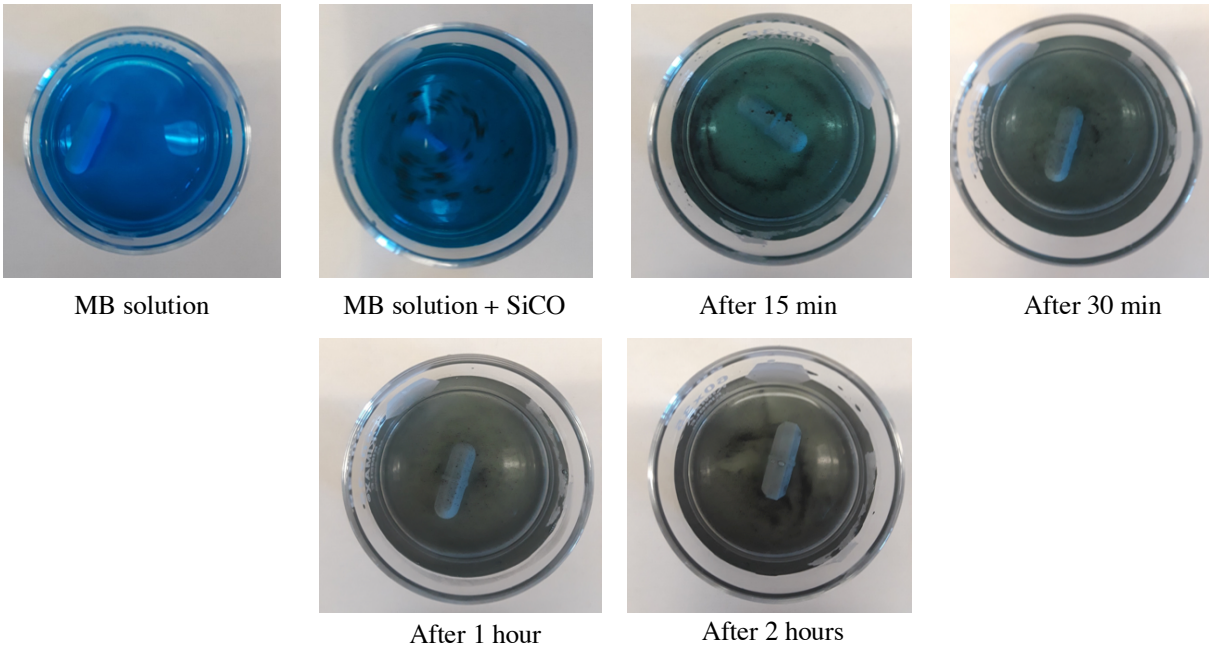

Figure 3-14 Digital images of MB solution and SiCO ambigels after stirring for determined time intervals

The variations in the absorption band at λ_{max} (664 nm) at the given time intervals were analyzed. The following table summarized the results after MB solution contact with SiCO powder. The adsorption percentage was calculated using the following equation:

$$\textit{Adsorption}\ \% = \frac{A_0 - A}{A_0}\ \mathbf{x\ 100}$$

Where A_0 corresponds to the initial UV-Vis absorbance of the MB solution and A is the final absorbance after stirring for a determined time. The following table summarizes the UV-Vis results after contact with SiCO powder.

Table 3-2 Adsorption Percent of MB Solution after Indicated Contact Time with Porous SiCO Powder

	Abs at λ_{max} (664 nm)	Adsorption %
MB solution	0.908	-
2 min	0.222	76
5 min	0.135	85
7 min	0.050	95
10 min	0.036	96
15 min	0.021	98

Porous SiCO displays an adsorption percentage of 98% after 15 minutes of contact time with MB solution. The following experiment consisted of utilizing a commercially available activated carbon powder (100 particle (mesh) and decolorizing) from Sigma Aldrich. The same procedure was performed as in the previous experiment, and the adsorption percentage was calculated for the UV-Vis absorption results and displayed in Table 3-3.

Table 3-3 Adsorption Percent of MB Solution after Indicated Contact Time with Activated Carbon Powder

	Abs at λ_{max} (664 nm)	Adsorption %
MB solution	1.213	-
2 min	1.072	12
6 min	0.952	21
10 min	0.942	22
15 min	0.913	25
20 min	0.877	28
60 min	0.692	43
21 hours	0.427	79

The adsorption percentage of MB is significantly lowered using activated carbon. The adsorption percentage of MB at 15 min of magnetic stirring with activated carbon is 25% in

comparison to 98% when using porous SiCO. The adsorption efficiency of SiCO was also compared to mesoporous silica (Sigma Aldrich. USA). The experiment was done following the same procedure as before. The following table summarizes the results.

Table 3-4 Adsorption Percent of MB Solution after Indicated Contact Time with Mesoporous Silica Powder

	Abs at λ_{max} (664 nm)	Adsorption %
MB solution	1.186	-
2 min	0.908	23
6 min	0.751	37
10 min	0.486	60
15 min	0.397	67
20 min	0.336	72
45 min	0.276	78
24 hours	0.223	81

The following figure displays the time-dependent UV-Vis spectra of the three solutions. The top right figure of UV-Vis spectra shows the time-dependent UV-Vis spectra of the MB solution with SiCO added. The top left figure displays UV-Vis spectra corresponding to activated carbon, and bottom spectra correspond to mesoporous silica.

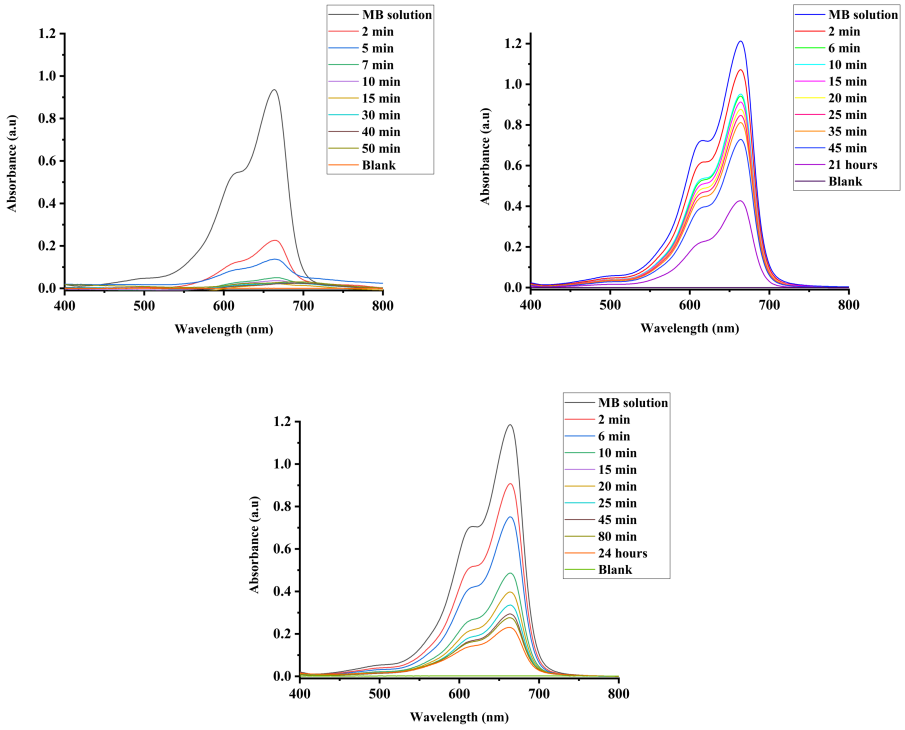

Figure 3-15 UV-Vis characterization of MB solutions (top left) with activated carbon, (top right) SiCO material, and (bottom) with mesoporous silica

The adsorption percentage for the three different materials in respect to time is compared in Figure 3-14. Overall, a higher adsorption percentage (%) is achieved in shorter times using SiCO. SiCO adsorbs MB solution significantly faster and at higher amounts in comparison to activated carbon and mesoporous silica.

Mesoporous silica adsorbs MB solution significantly higher in comparison to activated carbon. At 15 minutes of contact time, the adsorption percentage (%) of mesoporous silica is 67% in comparison to the 25% adsorption of activated carbon. The same initial concentration (10 ppm in Millipore DI water) was used for all 3 runs. The 98% adsorption (in 15 minutes of contact time) of porous SiCO accounts for the adsorption of 9.8 mg/L of MB solution. In contrast to the activated carbon and mesoporous silica % adsorption (in 15 minutes of contact time) of 2.5 mg/L and 6.7 mg/L of MB solution. This result corresponds to porous SiCO having 3 times

as much adsorption percent (%) as activated carbon, and 32% as much as mesoporous silica in 15 minutes of contact time. 15 mg of sample were used for each run correspondingly. The following figure displays the adsorption percentage vs. time for all materials.

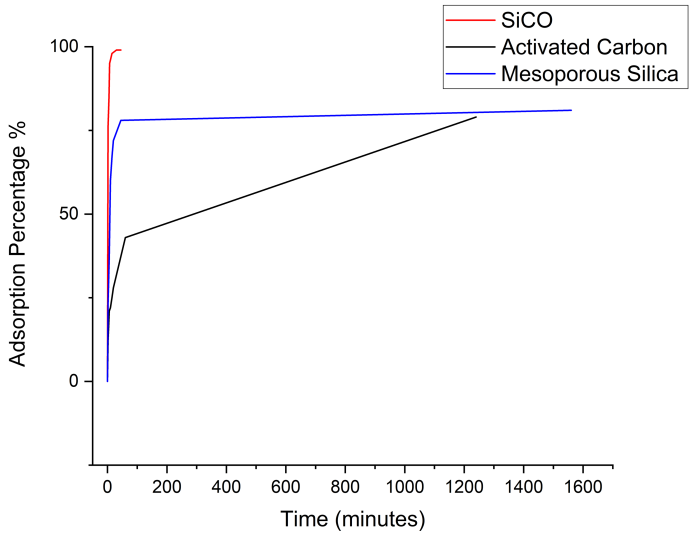

Figure 3-16 Adsorption percentage (%) for SiCO, activated carbon and mesoporous silica

The following digital pictures illustrate the MB solutions after the end of the adsorption procedure. Figures illustrate the appearance of the final solution after the end of the experiment for each different material, respectively. For the SiCO material and MB solution, this final time corresponds to 50 minutes, for activated carbon and mesoporous silica added to the MB solution the time corresponds to overnight stirring.

Figure 3-17 Digital images of MB solution + SiCO, MB solution + activated carbon and MB solution + mesoporous silica (from left to right) after the experiment

To understand the adsorption mechanism is critical to know about the experimental conditions and the MB charge at the time of the experiment. The pK_a of MB dye is 3.8. The adsorption studies were performed at pH 5. Under these conditions; MB is positively charged in solution. MB is a cationic dye which can be adsorbed in two different ways:

Cation exchange capacity: in which there is an irreversible exchange that corresponds to the number of exchange sites available in the adsorbent

Surface adsorption: reversible physical adsorption

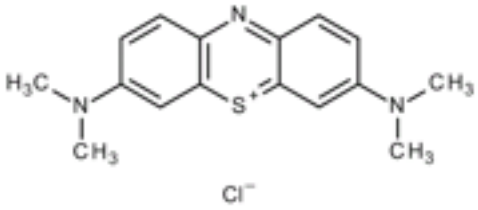

Figure 3-18 Molecular structure of Methylene Blue (MB) dye

3.4 Conclusion

These results show a complete reduction of MB dye characteristic UV-Vis absorption peak after overnight contact. In contrast; overnight contact with activated carbon and mesoporous silica resulted in an 80 % reduction of UV-Vis characteristic absorption peak of MB

dye; despite of their higher SSA_{BET}. Results are an example that the adsorption process is not only governed by SSA, but also by microstructural features and surface functional groups.

These results point out the relevance of SiCO chemical properties. Recent studies conducted by Bruzzoniti et al.[21] demonstrated PDC SiCO's adsorption ability in comparison to SiC foams and commercially available materials. The reason for porous SiCO to have higher adsorption ability might be accounted for by its structure, comprising of an amorphous silicon oxycarbide phase and a free carbon phase (turbostratic carbon). These materials possess hierarchical porosity and different chemical bonds (Si-C, Si-O, C=C), which could make it possible for SiCO to target a variety of contaminants. Porous SiCO materials are promising candidates to target adsorption of contaminants.

Pore structure is another variable influencing the microstructure of these materials. Pore structure arises from synthesis conditions. For example, sol-gel SiCO materials form by agglomeration and precipitation. These materials form a 3D network of connected spheres that precipitate and form a gel. This synthesis method forms void shaped pores that are irregular in shape due to their connectivity, and generally possess a hierarchical structure. Commonly these materials have irregular pore structure shapes. These irregular pore structures, along with SiCO ceramic structural features might play a role in its capacity for adsorbing MB dye.

Further experiments will need to be performed to understand the adsorption mechanisms of SiCO materials as well as investigating the applicability of these materials to adsorb different dyes or contaminants. Further investigations can also include the regeneration of these materials after the adsorption process.

Chapter 4

Sol-gel SiCO Ambigels Microstructural Evolution Upon Pyrolysis Temperature

Abstract

Silicon oxycarbide (SiCO) porous materials were synthesized using the sol-gel method. SiCO porous materials were synthesized using BTEE as precursor and catalyzed using and HCl solution and slowly dried at low temperature. Materials were annealed in inert atmosphere starting from 400 °C up to 1000 °C. SiCO ambigels were characterized using FT-IR, FE-SEM, nitrogen adsorption analysis to investigate the surface evolution upon increasing temperature. BJH analysis shows that the average pore diameter remains almost constant up to 1000 °C, and SSA_{BET} is decreased by up to 55 % at 1000 °C. These results suggest that pore development, as well as particle shrinkage of SiCO ambigels, play a role in the microstructural properties of sol-gel derived SiCO ambigels.

4.1 Introduction

The sol-gel method is a low-temperature synthesis method that allows for ease of processing and shaping.[68] The synthesis of silicon oxycarbide glasses using the sol-gel method has been the target of several studies.[50, 69-70] Silicon oxycarbide materials are synthesized using a silicon alkoxide with the general formula Rn-Si(OR)4-n. The Si-C bonds are maintained in the structure during the hydrolysis and condensation process and through the pyrolysis step. This result was first confirmed by ^{29}Si magic angle NMR experiments performed by Babonneau et al., and Zhang and Pantano.[70-71]

Porous silicon oxycarbide glasses have been synthesized from a variety of precursors using the sol-gel method as described in Singh and Pantano.[72] Insight of microstructural stability upon pyrolysis temperature can help to tailor properties such as pore size distributions and average pore diameter.

BTEE derived ambigels have been prepared previously with and without aging in silane solution and with high and low hydrolysis ratios. Aging in silane solutions has been utilized for

strengthening the 3D network of aerogels synthesized using ambient conditions. [73-74] It was reported in Aravind and Sorarù 2011 that aging the gels in silane solutions did not strengthen the gel network when using the1,2 BTEE precursor and that high and low hydrolysis ratios had an effect on SSA found in the SiCO ambigels.[25] We do not investigate aging in silane solution or hydrolysis ratios in this present study.

Applications of porous silicon oxycarbide ceramics include drug delivery[53, 75], supercapacitors[76], and Li-ion battery applications.[77-78] The purpose of this study is the investigation of the microstructural stability of SiCO porous materials with pyrolysis temperature and ceramic conversion.

4.2 Experimental

4.2.1 Chemicals

1,2 Bis(triethoxysilyl)ethane (1,2 BTEE; Aldrich catalogue number: 447250; used without further purification). Isopropanol was bought from EMD Millipore, and HCl was obtained from Macron Fine Chemicals, and all chemicals were used without further purification.

4.2.2 Ambigel Synthesis

Synthesizing ambient dried SiCO porous materials (ambigels) we follow the procedure outlined in Dire et al. 2015.[27] In brief, starting with 1,2 Bis(triethoxysilyl)ethane (1,2 BTEE; Aldrich catalogue number: 447250; used without further purification) we dissolved the silicon alkoxide in isopropanol under constant stirring until we obtained a homogeneous mixture. For the one-step acid sol-gel synthesis, we added 3M HCl dropwise to initialize hydrolysis and condensation and continued stirring for another 15 minutes. Overall, the molar ratio between the reactants 1,2 BTEE: isopropanol: HCl was chosen to 1:5:0.006. The starting mass of BTEE was 16.19 grams. The chemical composition of the crosslinked non-pyrolyzed material is calculated from the precursor assuming complete condensation.[27] This assumption provides a hypothetical formula of $H_2CSiO_{1.5}$ for the non-pyrolyzed sample.

The clear and homogenous solution was then covered with parafilm and placed in an oven at 50 °C. Every 12 hours (twice a day) we exchanged the solvent with fresh isopropanol until after about two weeks the gel was visibly dry. Thereafter, we kept the gels in the oven for another month to dry completely. Samples obtained after the complete process were typically broken, see Figure 4-1.

4.2.3 Pyrolysis Procedure

Pieces of the SiCO ambigel were pyrolyzed in a quartz tube under flowing N_2 atmosphere (flow of 1 L/min) at different temperatures. To investigate the development during pyrolysis, we set maximum pyrolysis temperatures T_{max} of 400 °C, 600 °C, 800 °C, and 1000 °C. Samples were heated with a rate of 5 °C/min up to T_{max}, then kept at T_{max} for 2 hours, and cooled thereafter by switching off the furnace. Initial and final masses were recorded to calculate mass loss. Shrinkage of samples could not be quantified due to their irregular shape. The precursor, together with T_{max}, is used to identify the different samples: e.g. BTEE1000 for the sample exposed to 1000 °C.

4.2.4 Characterization Procedure

4.2.4.1 Microstructural Analysis

Nitrogen adsorption analysis was performed at 77 K using an ASAP 202 Micromeritics Instrument (Micromeritics, Norcross, GA). Ambigel samples were degassed using an evacuation ramp rate of 10 °C/min up to 90 °C. We used an evacuation rate of 5 mmHg/s with a vacuum setpoint of 10^{-3} mm of Hg. To calculate specific surface area, the BET equation (SSA_{BET}) was applied using a molecular cross-sectional area of 0.1620 nm^2 and a correlation coefficient of 0.9571864. Pore size distribution and average pore diameter are obtained from the desorption branch of the isotherm using the BJH model using the Faas correction and Halsey thickness curve.[61-62]

4.2.4.2 Vibrational Spectroscopy: FT-IR Characterization

FT-IR spectroscopy and (Bruker's ALPHA-P FTIR spectrometer) was recorded for the BTEE samples. For analysis, the sample was grounded with pestle and mortar. Spectra were recorded in transmittance mode between 4000 and 400 cm^{-1} with a resolution of 4 cm^{-1}.

4.2.4.3 Surface Characterization: FE-SEM imaging

FE- SEM (Field Emission Scanning Electron Microscopy) images were obtained using a Hitachi S-4800-II FE-SEM. Samples were broken using tweezers to create a small crack to form a fracture surface. Prior to SEM imaging, we coated samples for 2 minutes using a CRC 100 sputtering system. Particle sampling and measuring were performed using ImageJ software(include reference). We collected diameters for 50 individual particles in each between 30 (for BTEE50), and 50 (for BTEE400-BTEE1000) particles were collected for each sample, with the exception of BTEE50 for which only 30 particles were observed due to agglomeration and apparent fusing. Testing for outliers using the first and third quartiles was performed, but none was detected.

4.3 Results and Discussion

4.3.1 Physical Appearance

SiCO ambigels received after gelation are translucent and cracked see Figure 4-1 (far left). Even after annealing at 400°C the sample retains is white/ translucent appearance, while further annealing yields to strong changes: BTEE600 takes an orange color and BTEE800 and BTEE1000 appear black and glassy. The following image displays the resulting SiCO ambigels.

Unannealed SiCO sample is at the far left, and SiCO annealed at 1000 ºC (BTEE1000) is at the far right.

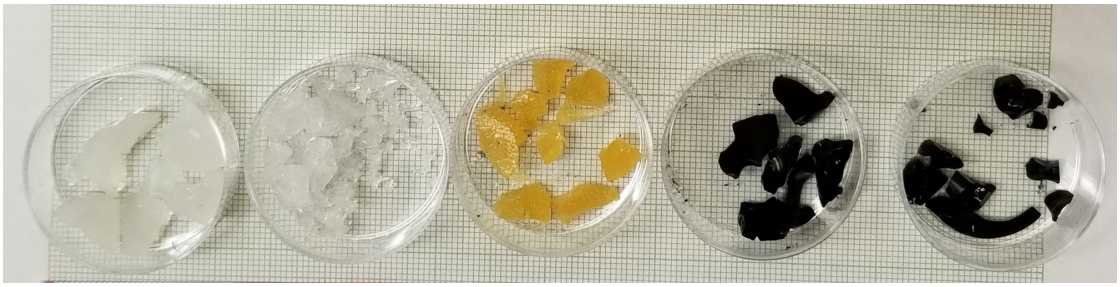

Figure 4-1 SiCO ambigel samples obtained after annealing. From left to right: BTEE50, BTEE400, BTEE600, BTEE800, and BTEE1000

4.3.2 Mass Loss

The mass losses of samples, relative to BTEE50, are given in Table 4-1. While the mass loss of BTEE400 is below 1%, a significant mass loss of 15% occurs only between 400 and 600 °C. Samples annealed at 600, 800, and 1000°C have almost identical masses. The magnitude of mass loss, as well as the temperature range in which it occurs, are characteristic for pyrolysis of sol-gel derived SiCO materials,[10, 79] although variations depending on precursors used do occur. In a previous study, the pyrolysis of BTEE-derived SiCO ambigels in flowing Ar showed a mass loss of 10% up to 300 °C and another 10% between 400 and 600 °C.[25] The first step is typically associated with water evolution, while the second mass loss relates to condensation reactions of Si-OH and Si-OEt. Table 4-1 summarized the mass loss percentage results and the physical appearance of the resulting materials.

Table 4-1 Mass Loss Percentage and Physical Appearance of SiCO Ambigels as Received and Annealed at Different Temperatures

Sample	% Mass Loss	Physical Appearance
BTEE50	N/A	Translucent, hard chunks
BTEE400	0.8	Transparent, cracked
BTEE600	15	Yellowish
BTEE800	16	Shiny, black, hard chunks
BTEE1000	16	Shiny, black, hard chunks

4.3.3 Surface Characterization: FE-SEM Imaging

Electron micrographs of the fresh fracture surface of samples are presented in Figure 4-2. The microstructure of the ambigels resembles an agglomeration of particles of different sizes densely packed together. The apparent size of particles is largest for BTEE50 and decreases with increasing annealing temperature. Individual particles in BTEE50 are difficult to distinguish while they appear more defined for BTEE1000. Using the FE-SEM images, we quantified particle size distributions with the help of the ImageJ software.[80] Only primary particles defined as the smallest identifiable units in a particulate system, are used in the analysis.[81] Particle sizes fall into the range from 30 to 400 nm for all samples and are shown as histograms in Figure 4-3.

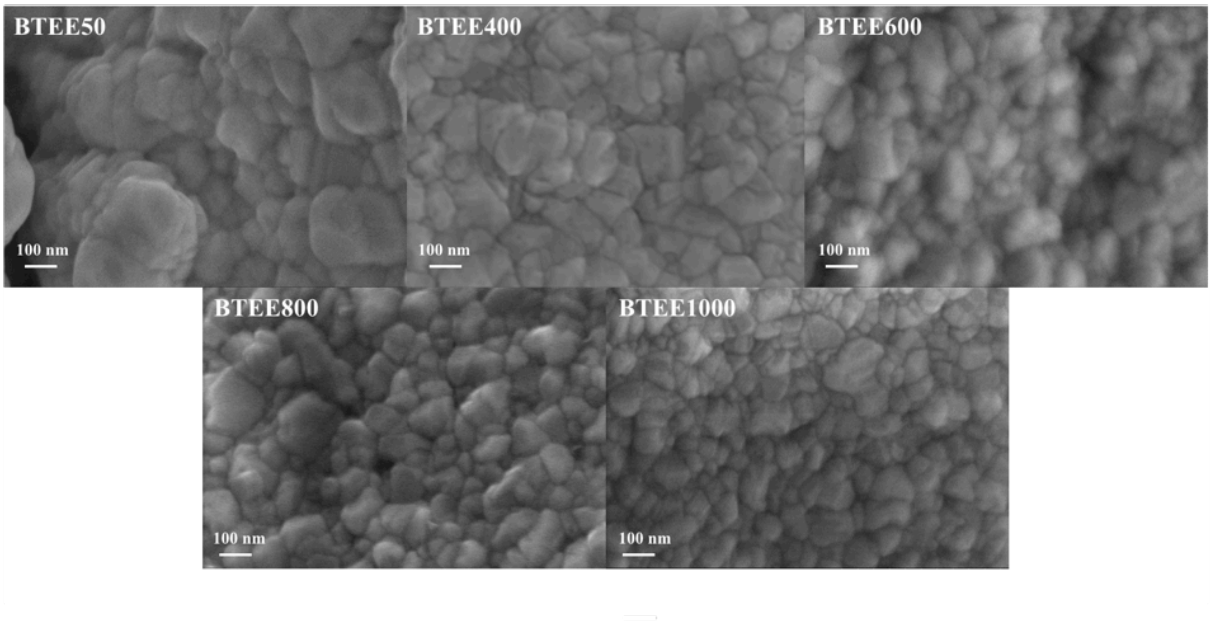

Figure 4-2 FE-SEM images with scale bar (equivalent) of BTEE50 to BTEE1000

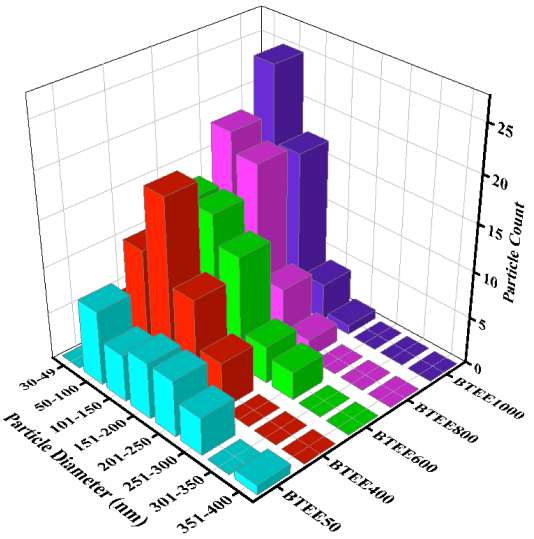

Figure 4-3 Histograms for particle size sampling for SiCO ambigels based on FE-SEM images

Using the sampling data of the FE-SEM images, we calculated the average size of particles in the microstructure, see Table 4-2. Overall, with increasing temperature, the average particle size decreases. The average particle size found in BTEE50 is 168 nm and decreases to almost half its value, 90 nm, in BTEE1000. Since the standard deviation also decreases as temperature increases, it turns out that the dispersion of the distribution, characterized by the relative standard deviation, remains approximately constant ($\sigma/\mu \approx ½$). Thus, the particle sizes encounter a homogeneous change during annealing, with no particular preference for small or large particles. Particle size analysis of some silica aerogels showed that functional groups on the surface such as methyl groups were oxidized or decomposed, but that the aerogel structures were stable up to 550 °C, and when the temperature was increased up to 800 °C micropores collapsed. Their results also showed that the diameter of a primary silica aerogel particle first expands and then shrinks upon heating and that the volume of a single particle generally decreases with increasing holding time (at 1000 °C) due to the elimination of destruction of the porous structure. Their results showed a dependence on particle size and

densification. The largest shrinkage was around 70 % for 75 μm diameter silica aerogel particles.[82] The results were related to pore shrinkage and collapse.[82]

The following table displays the average particle length along with the standard deviation for samples BTEE50 to BTEE1000.

Table 4-2 Average Particle Size and Standard Deviation of the Particle Size Analysis for SiCO Ambigels

Sample	Average Particle Length (nm)
BTEE50	168±78
BTEE400	125±48
BTEE600	140±60
BTEE800	106±43
BTEE1000	90±42

4.3.4 Porosity Analysis

The following figures display nitrogen isotherms, pore volume, and pore size distribution for all samples. From the nitrogen isotherms, it is possible to observe that the maximum amount of N_2 adsorbed decreases with increasing temperature for all samples, except for BTEE400 and BTEE600. The same trend is observed for the pore volume and pore size distribution results.

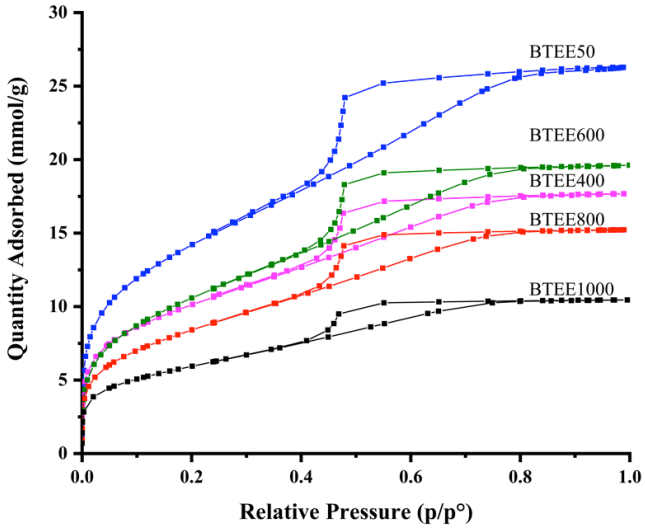

Figure 4-4 Nitrogen isotherms of BTEE-derived SiCO ambigels

Gas sorption analysis is an established technique for the characterization of porous solids. Adsorption and desorption curves are determined by the interaction between adsorbent and adsorbant species as well as by condensed state interactions. Nitrogen isotherms of SiCO ambigels are displayed in Figure 4. According to IUPAC nomenclature, they are classified as IV(a).[66] In these isotherms, capillary condensation follows a hysteresis loop, which occurs when a critical width is exceeded by the pore width.[83] The hysteresis loop present in these materials resemble an H2(a) hysteresis loop. The steep desorption branch is a characteristic that can be attributed to pore-blocking/percolation in a narrow range of pore necks or cavitation-induced evaporation. This type of hysteresis loop is found in many silica gels, some porous glasses and some ordered mesoporous materials such as SBA-16 and KIT-5 silicas.[66]

The BTEE50 isotherm displays the highest quantity of adsorbed of nitrogen of all samples. This amount decreases with increasing temperature for all the samples, with a notable exception for BTEE600.

Figure 4-5 displays the cumulative pore volume (cm^3/g) vs. pore width and figure 4-6 and the pore size distribution of the samples. The data was obtained from the desorption branch of the isotherm using the BJH model. BTEE50 displays the largest pore volume of 0.77 cm^3/g and the largest average pore width of 3.65 nm. With increasing temperature, pore volume and average pore size decrease. An exception is present with BTEE600 since it falls slightly out of the trend. Pore volume and average pore sizes decrease to 0.30 cm^3/g and 3.50 nm, respectively, for BTEE1000. Note that in all samples, almost the complete pore volume is accumulated in small pores with diameters below 5 nm.

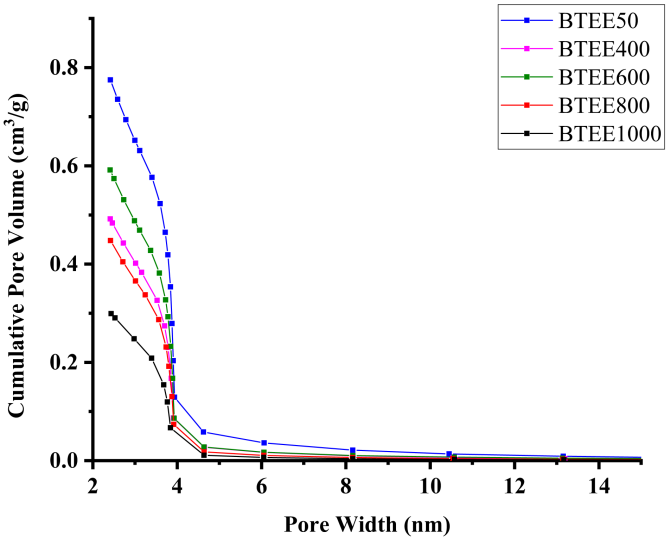

Figure 4-5 BJH desorption cumulative pore volume of BTEE-derived SiCO ambigels

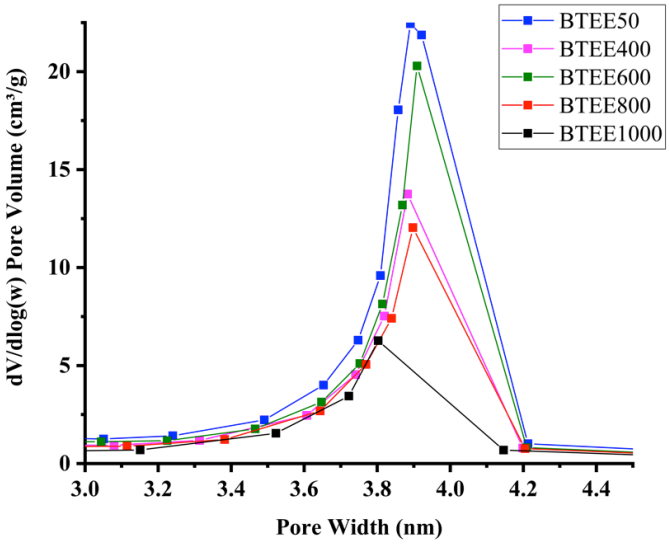

Figure 4-6 dV/dlog(w) pore volume (pore size distribution) derived from the BJH desorption branch for BTEE-derived SiCO ambigels

The following table summarizes the results of the nitrogen adsorption analysis of the SiCO ambigels using the BET and BJH methods.

Table 4-3 Summary of BET and BJH Analysis of SiCO Ambigels

Sample	SSA_{BET} (m^2/g)	BJH Pore Volume (cm^3/g)	BJH Pore diameter (nm)
BTEE50	736±41	0.77	3.64
BTEE400	551±30	0.49	3.56
BTEE600	620±29	0.59	3.56
BTEE800	472±26	0.45	3.53
BTEE1000	329±21	0.30	3.50

The specific surface area SSA_{BET} of annealed SiCO ambigels decreases with increasing temperature, see Table 4-3. This result parallels the observed changes in pore volume and average pore diameters. The highest SSA_{BET} of 736 m^2/g is achieved for BTEE50 and

decreases to 329 m^2/g for BTEE1000. Previous work on BTEE derived SiCO ambigels reported 1131 m^2/g and 430 m^2/g for the SSA_{BET} of dried and annealed (at 1000°C) SiCO ambigels.[25] Using methyl-tryethoxisilane (MTES) as precursor to synthesize SiCO ambigels produced dried ambigels with SSA_{BET} of 727 m^2/g with a BJH pore volume and average pore diameter of 1.43 cm^3/g and 8 nm respectively.[26] The various "discontinuities" in property changes that occur between BTEE400 and BTEE600 are due to significant changes in the SiCO ambigel during annealing between 400 and 600°C. This temperature range, for which the highest mass loss is reported, is most crucial in the conversion of carbon-bearing siloxanes into SiCO ceramics.[10] A transient increase in porosity has been reported for other SiCO materials, and it attributed to the evolution of gaseous compounds.[84-86]

The average pore diameter of the SiCO ambigels, extracted from the desorption branch of the isotherm (see method section), is 3.64 nm in the dried gel and decreases slightly to 3.50 nm in BTEE1000. This small change in linear dimension is significantly smaller than the almost 50% decreases in particle size analysis observed earlier. Moreover, a mere 4% change in pore diameter does not relate to the much larger changes in surface area and pore volume. Hence, relative to particle size, surface area, and pore volume — quantities that change considerably upon annealing – the diameter of pores remains remarkable "stable" throughout the temperature range up to 1000 ºC. Previous experiments of BTEE-derived SiCO ambigels yielded a similar result.[25] While SSA_{BET} decreased from 1131 m^2/g to 430 m^2/g, and BJH pore volume decreased from 1.29 cm^3/g to 0.46 cm^3/g in dried gel and sample annealed at 1000 °C, the average pore diameter remained "stable" at 4.2 nm. The MTES-derived SiCO ambigels mentioned earlier were not annealed and characterized.[26]

The observation of an almost "constant" average pore diameter is somewhat puzzling. A decrease in SSA_{BET} is usually associated with the collapse of pores due to material densification. Given the gradual shrinkage of the particle size, one can expect that pores show a similar gradual change as well. A possible explanation is related to the hysteresis observed in

the gas sorption curve. Such hysteresis occurs, for example, if pores are not cylindrical but are ink-bottle shaped with a wide body and a small window.[87] In that case, the diameter extracted from the desorption branch reflects only the diameter of the window, while the diameter of the body behind the window remains secluded. A method such as Differential Hysteresis Scanning can provide further insight.[88]

4.3.5 Vibrational Spectroscopy: FT-IR characterization

FT-IR spectra of the SiCO ambigel samples are displayed in Figure 4. The spectra for BTEE50 and BTEE400 display a very subtle peak around 1630 cm^{-1} but not a noticeable peak around 4000-3000 cm^{-1}. These two bands correspond to water adsorbed in the sample. Also, set those samples apart from samples annealed at higher temperatures. It has been reported in the literature that due to the expected hydrophobic properties of similar gels (bearing Si-CH_3 units) absorption bands around 1635 around 4000-3000 cm^{-1} due to water adsorbed in the sample are not present in these materials.[64]

BTEE50 and BTEE400 display small bands around 1414 and 1273 cm^{-1}, these bands are close to what corresponds to methyl group vibrations.[89] For BTEE600, bands at 1414 cm^{-1} and 1273 cm^{-1} are still present but are quite small. For BTEE800, the bands are decreasing even more, and for BTEE1000 the bands are basically gone. All samples show characteristic Si-O asymmetric stretching frequencies at around 1005 cm^{-1}. BTEE50 and BTEE400 display a clear shoulder at 1152 cm^{-1} on the peak around 1005 cm^{-1}. BTEE600 displays a more diffuse shoulder at 1152 cm^{-1}, and for BTEE800 and BTEE1000 this shoulder is even less prominent. Bands at 1150 cm^{-1} are reported to be due to Si-O bonds in a siloxane network.[64] The disappearance of this shoulder in the FT-IR spectra signals the conversion of the sol-gel to ceramic. The decrease of the CH_3 stretching frequencies with increasing temperature can be related to the demethanation of the gels, which has been observed previously in FT-IR analysis of sol-gel SiCO ceramics.[90] Bands positioned around 900- 700 cm^{-1} are caused by the overlay

of Si-O, Si-C stretching vibrations. Figure 4-7 displays the FT-IR spectra of all BTEE- derived SiCO ambigels.

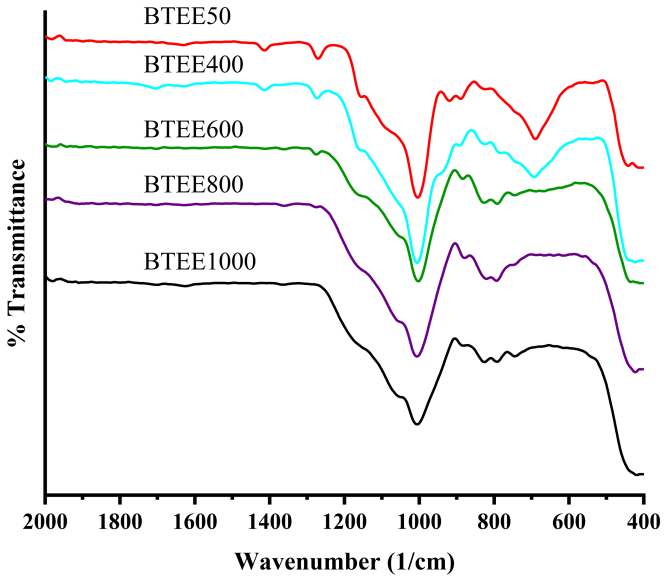

Figure 4-7 FT-IR spectra of BTEE50 to BTEE1000 (SiCO ambigels)

4.3.6 Discussion

BTEE50 to BTEE400

BTEE50 is translucent and in pieces after the gelation and drying process. From BTEE50 to BTEE400 there is a mass loss of 0.8%. BTEE400 sample is shrunk and cracked after heat treatment and looks transparent in appearance. The BTEE50 sample shows the highest SSA_{BET} with a value of 736 m^2/g, and it decreases to 551 m^2/g for BTEE400. This value corresponds to a decrease of 25% in SSA_{BET}. The BTEE50 BJH pore volume is 0.77 cm^3/g, and it drops to 0.49 cm^3/g for BTEE400, and this is a 36% decrease while the average pore diameter drops from 3.64 to 3.56 nm corresponding to a 2% decrease.

The particle size investigation using FE-SEM imaging yielded an average particle length of 168±78 for BTEE50 and 125±48 for BTEE400.

Unannealed BTEE-derived SiCO ambigels were synthesized with a high and low hydrolysis ratio. SiCO ambigel synthesized with the low hydrolysis ratio had an SSA_{BET} of 938 m^2/g with a total pore volume of 0.61 cm^3/g and 2.6 nm average pore diameter. SiCO ambigels synthesized with the lower hydrolysis ratio had an SSA_{BET} of 1131 m^2/g, a pore volume of 1.29 cm^3/g and an average pore diameter of 4.5 nm.[25]

Intermediate temperatures for these materials have not been investigated to the best of our knowledge.

In a different study, SiCO materials synthesized using triethoxysilane and methyldiethoxysilane were synthesized with three different T_H/D_H ratios. They found that from the gel state to 400 °C SSA_{BET} increased for samples with T_H/D_H ratios of 1 and 2, but decreased for the sample with T_H/D_H ratio of 9. Also, the sample with T_H/D_H ratio of 9 had the highest SSA_{BET} in the gel state.[68]

BTEE400 to BTEE600

From BTEE400 to BTEE600 there is a mass loss of 15%. The appearance of BTEE600 is yellowish. There is a mass loss of 15% after the heating process. BTEE400 has a SSA_{BET} of 551 m^2/g while BTEE600 has an SSA_{BET} of 620 m^2/g this corresponds to an 11% increase. The BTEE400 pore volume is 0.49 cm^3/g while for BTEE600 is 0.59 cm^3/g; this is a 17% increase. The average pore volume for BTEE400 and BTEE600 remains at 3.56 nm.

Average particle size for BTEE400 was 125±48 and 140±60 nm for BTEE600, so the average particle size increases by 11%.

Samples synthesized using triethoxysilane, and methyldiethoxisilane showed that there was a decrease in SSA_{BET} for samples including 1, 2 and 9 T_H/D_H ratios going from 400 to 600 °C.[68]

BTEE600 to BTEE800

BTEE800 is dark and shiny. There is a mass loss of 16%. SSA_{BET} of BTEE600 decreases from 620 m^2/g to 472 m^2/g. This change corresponds to a decrease of 24%. Pore

volume decreases from 0.59 cm^3/g to 0.45 cm^3/g, and average pore diameter decreased from 3.56 to 3.53 nm. These are a decrease of 24% and 0.8% respectively. The average particle length for BTEE800 is 106±43, which corresponds to a particle length decrease of 24%.

Nitrogen adsorption analysis was performed for samples synthesized using triethoxysilane and methyldiethoxisilane showed that there was a decrease in SSA_{BET} for samples including 1, 2 and 9 T_H/D_H ratios from 600 to 800 °C.[68]

BTEE800 to BTEE1000

BTEE1000 is dark and shiny, and it appears almost identical to BTEE800. It has a mass loss of 16%. After rounding the mass loss of BTEE800 and BTEE1000 is the same. SSA_{BET} of BTEE1000 is 329 m^2/g, constituting an SSA_{BET} loss of 30% from BTEE800. The pore volume was 0.30 cm^3/g, and the average pore diameter was 3.50 nm. This is a pore volume decrease of 33% and a pore diameter decrease of 1%. Particle length average decreases to 90±43 for BTEE1000, and this represents a 15% decrease from BTEE800.[68]

BTEE-derived SiCO ambigels were annealed at a 1000 °C. The resulting materials had an SSA_{BET} of 430 m^2/g, a pore volume of 0.46 cm^3/g and an average pore diameter of 4.2 nm. This constitutes a decrease of 62% in SSA_{BET}, a decrease of 64% in pore volume and a 7% decrease in average pore diameter.[25]

In the same study of SiCO glasses outline above; SSA_{BET} decreased for all samples with different T_H/D_H ratios.

4.4 Conclusion

We synthesized SiCO porous materials using sol-gel synthesis using a solvent with low surface tension (isopropanol) as prepared in the literature.[25, 27] Ambient dried SiCO aerogels with high SSA_{BET} and narrow pore size distributions were obtained in this work. Nitrogen adsorption analysis can be summarized as follows: SSA_{BET} decreases 25% from BTEE50 to BTEE400 and increases 10% from BTEE400 to BTEE600, and there is an overall final SSA_{BET} loss of 55% from BTEE50 to BTEE1000.

The pore volume calculated using the BJH model shows a decrease from BTEE50 to BTEE400 of 36%. There is a 13% increase in pore volume from BTEE400 to BTEE600 and an overall final decrease of 61%. The average pore diameter for all the samples is 3.56±0.05 nm. There is an overall average pore diameter decrease of 4%. These results indicate that the calculated average pore diameter does not change significantly up to 1000 ºC.

The sampling particle size of SiCO ambigels was performed using ImageJ software on FE-SEM. The average particle length for BTEE50 is 168 nm and decreases to 90 nm for BTEE1000. Average particle size decreases by almost up to 50% at 1000 °C. These results suggest the importance of particle size as well as pore size changes upon heat treatment of SiCO ambigels.

Chapter 5

Investigation of Microstructural Evolution of Bulk SiCO Ceramics Annealed up to 1500 °C

Abstract

The motivation for this work is to investigate the properties of bulk SiCO ceramics when exposed up to 1500 °C in Argon atmosphere. Dense monolithic SiCO ceramics are synthesized through the polymer-derived ceramic (PDC) route using polymethylhydrosiloxane (PMHS) and divinylbenzene (DVB).

This work is a systematic investigation of a 1:2 mass ratio of PMHS: DVB SiCO ceramic annealed from 1000-1500 °C. In this work we have prepared samples in 100 °C increments to provide a detailed study in this temperature range.

Materials were characterized using powder XRD, SEM, FT-IR, and Raman spectroscopy. These materials show phase separation above 1200 °C. Phase separation evolution depending on exposure temperature is an important characteristic of these materials since this affects properties such as crystallization and oxidation.

The XRD analysis provides information about the progressive increment of SiC crystalline growth as well as the presence of small and decreasing graphite peaks with increasing annealing temperature. The XRD analysis provides information about the formation of graphite in these materials, and along with Raman analysis, we investigate the free carbon phase present in these SiCO ceramics.

5.1 Introduction

Silicon oxycarbide materials belong to the polymer derived ceramics or PDC's. They have the general formula $SiC_xO_{2-2x} + yC_{free}$ where SiC_xO_{2-2x} corresponds to the oxycarbide phase (SiO_2 and SiC) and yC_{free} to the free carbon phase.[90] Where the atomic composition is related to the precursor in the precursor structure.[91] SiCO materials are amorphous and metastable compounds up to temperatures about 1300 °C.[92]

The use of polymer precursors with a variety of compositions allows for control of the oxycarbide phase and the graphitic like or free carbon phase.[79] The PDC process consists of a starting material (polymer or alkoxide) that is shaped, crosslinked and converted to a ceramic material through pyrolysis in controlled atmospheres at temperatures above 800 °C. Through the PDC route; it is possible to obtain materials with complex nanostructures; comprised of nanocrystalline and amorphous phases.[57]

SiCO materials possess a low steady-state creep rate up to 1300 °C[93] and resistance to crystallization up to 1300 °C having a primarily amorphous structure.[28] Carbon content in these materials influences oxidative stability and thermal expansion.[55] These materials have been characterized through ^{29}Si NMR and XPS spectroscopy.[94] ^{29}Si NMR studies show Si-C bonds retained after pyrolysis. ^{29}Si NMR shows Silicon having: SiO_4, $SiCO_3$, SiC_2O_2, SiC_3O, and SiC_4 possible sites.[79, 91] Carbidic carbon atoms (in the oxycarbide phase) should be bonded only to silica giving rise to CSi_4 units, but the local bonding of carbon is more complex. Residual hydrogen cannot be disregarded, and can still be present in the structure in CH or CH_2 units. Also, C-O-Si units can be in the SiCO structure.

SiCO materials structural characterization has been the topic of several literature papers.[16, 55, 92, 95-96] Graphitic carbon in SiCO materials is known to undergo structural ordering with increasing temperatures at about 1500 °C. Also, quantitative NMR studies show phase separation into SiO_4 and SiC_4 groups, and XRD analysis shows β-SiC crystallites around 1400-1500 °C. This is consistent with the onset of carbothermal reduction of silica with the free carbon phase; forming silicon carbide and carbon monoxide.[97]

5.2 Experimental

5.2.1 Chemicals

PMHS (polymethylhydrosiloxane, average M_n : 1.700-3200), DVB (divinylbenzene technical grade 80%), and Karstedt's catalyst (Platinum(0)-1,3-divinyl-1,1,3,3-tetramethyldisiloxane complex solution in xylene, Pt ~2%) were purchased from Sigma Aldrich. All chemicals were used without further purification.

5.2.2 SiCO Bulk Synthesis

We placed 2 g of DVB in a small glass container with a diameter of 3.5 cm, added 1 g of PMHS and stirred the solution for 5 min. Given the structure of PMHS and DVB, this yields a ratio of Si-H to C=C bonds of 1:2. We then added 10 μL of Karsted's catalyst to the solution and stirred for another 5 min. The solution was covered with parafilm and left for gelation at room temperature overnight. This procedure follows precedence in Blum et al. 2005.[28] Resulting materials are disk-shaped, transparent, and resin-like with a diameter of about 3 cm. The thickness of the disks was about 0.5 cm.

5.2.3 Pyrolysis (Polymer to Ceramic Conversion)

The PMHS/DVB disk samples were pyrolyzed in N_2 atmosphere (flow of 1 L/min) using a quartz tube. Using a heating rate of 5 °C/min samples were heated up to 400 °C and kept at 400 °C for 2 hours. Then temperature was increased at a rate of 5 °C/min up to 1000 °C. After holding at 1000 °C for 4 hours the furnace was switched off; no particular cooling rate was selected. The initial and final masses of the sample were recorded to calculate the mass loss percentage. The linear extension of the samples was measured before and after pyrolysis.

5.2.4 High Temperature Annealing

Annealing at higher temperatures was done in flowing Argon to at 1100, 1200, 1300, 1400 and 1500 °C in a tubular furnace. We used an even heating rate of 5 °C/min from room temperature to the maximum temperature and applied a holding time of 5 hours at the

maximum temperature. After heating, the furnace was turned off, with no cooling rate selected. The SiCO samples are labeled using the maximum temperature of exposure.

5.2.5 Characterization Procedure

5.2.5.1 FE- SEM Imaging

FE-SEM micrographs were taken on a Hitachi S-4800 II FE-SEM. Surfaces of the materials are studied. Prior to imaging, samples were coated on a CRC-100 sputtering system using a carbon target with two-minute sputtering time.

5.2.5.2 X-Ray Diffraction (XRD) Characterization

XRD data was accumulated on a BrukerD8 Advance powder X-Ray diffractometer equipped with an LYNXEYE XE detector. Spectra were taken in flat sample transmission geometry using a Cu Kα radiation source (λ= 1.54184 Å).

The Scherrer equation, which assumes a spherical model was used for the estimation of crystalline domains. Jade Software was used to calculate the mean size of the ordered (crystalline) domains. Calculations were possible for SiCO-1300, SiCO-1400 and SiCO-1500 using the peaks located at ~ 60 and 72° in 2θ.

5.2.5.3 Raman Characterization

Raman spectra were recorded with a Horiba LabRam Aramis Raman Spectrometer with an integrated confocal micro Raman system (Horiba Jobin Yvon, Bergheim, Germany). For high-resolution purposes, measurements were performed using 1200 lines/mm grating with a confocal magnification of 50 x with a laser power of 20 mW. Prior to analysis, the samples were grinded using mortar and pestle. All presented Raman data has been subjected to baseline correction using the Origin Software.[98]

5.2.5.4 FT-IR Characterization

FT-IR spectra were recorded on a Bruker's ALPHA-P FTIR spectrometer in transmittance mode with a resolution of 4 cm^{-1}, and a scan time of 16 scans/s. Spectra were

recorded between 4000 and 400 cm^{-1}. Before the analysis, the samples were grinded using mortar and pestle.

5.2.5.5 TGA Analysis

A Shimadzu TGA-50H was used to investigate the polymer to ceramic conversion as well as the oxidation of samples. For the polymer to derived conversion investigation, the analysis was performed in a platinum crucible in nitrogen atmosphere, with 20 mL/min gas flow, and a heating rate of 5 °C/min up to 900 ºC. For oxidation studies, the analysis was performed in a platinum crucible in air atmosphere, with no gas flow, and a heating rate of 5 °C/min up to 900 ºC.

5.3 Results and Discussion

5.3.1 Pyrolysis: Physical Characterization

After cross-linking but before pyrolysis the PMHS/DVB sample is a transparent and slightly yellowish resin, see Figure 5-1. Pyrolysis turns the sample black with metallic luster as seen by the reflections of SiCO-1000. SiCO-1000, SiCO-1100 and SiCO-1200 are similar in appearance, not at least since they remained in one piece. Samples SiCO-1000 to SiCO-1200 are hard and rigid and tough to break for analysis purposes. Samples annealed at 1300 °C and higher appear dull, brittle, and easily broken with handling, causing them to crack into several pieces.

Ceramic yield after pyrolysis, hence after exposing the material to 1000 °C, was 66% (±1%). This mass loss is consistent with previous TGA characterization for the same composition as presented here, where a yield of 60% was reported.[99] Another study of PMHS/DVB derived SiCO reports 60-65% ceramic yield.[63] Since disk samples retained their shape we could measure a linear shrinkage of 28% (±1%) between the cross-linked resin and pyrolyzed sample.

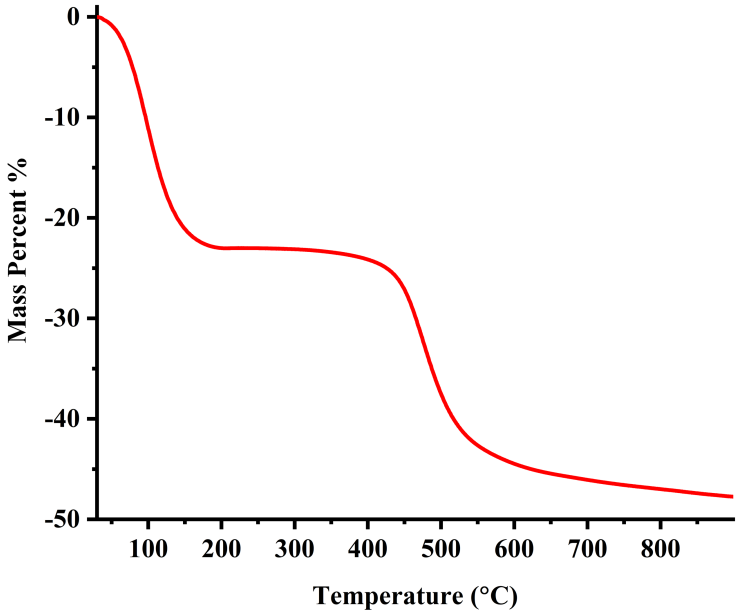

Figure 5-1 TGA analysis of cross-linked PMHS/DVB annealed in nitrogen atmosphere

We also report the additional mass loss due to annealing, hence, relative to material exposed to 1000 °C obtained after pyrolysis, see Table 5-1. The mass loss for SiCO-1100, SiCO-1200, and SiCO-1300 is less than 1%. Hence, while SiCO-1300 cracked during annealing, it did not lose significant mass. Mass loss observed for SiCO-1400 is 12.3%, and that of SiCO-1500 is 30%. Mass loss encountered at 1400 and 1500 °C is related to the evolution of gaseous species, e.g. SiO and CO, during carbothermal reduction. Carbothermal reduction along with sample mass loss at these temperatures is reported in literature results.[12]

Figure 5-2 shows the PMHS/DVB crosslinked material, and Figure 5-3 shows the SiCO ceramics after being exposed to higher annealing temperatures.

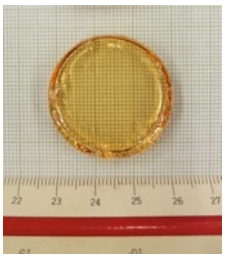

Figure 5-2 Optical image of PMHS/DVB crosslinked

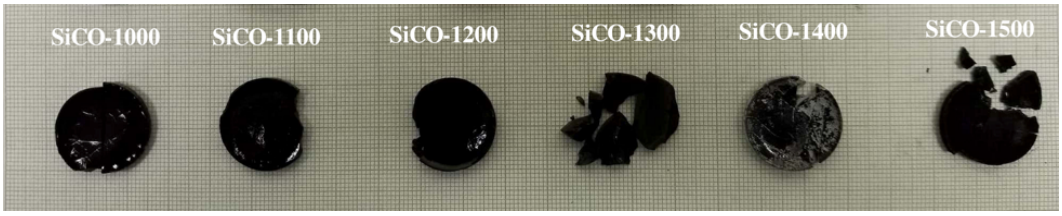

Figure 5-3 Optical images of SiCO ceramics from SiCO-1000 to SiCO-1500

Table 5-1 displays the mass loss percentage after pyrolysis up to 1500 ºC and physical appearance. Samples are identified with SiCO and the final temperature of annealing.

Table 5-1 Mass Loss % of SiCO PDC Samples up to 1500 ºC

Sample	Mass Loss %	Physical Appearance
SiCO-1100	0.2	Bulk, shiny, hard
SiCO-1200	0.3	Bulk, shiny, hard
SiCO-1300	0.7	Opaque, powdery
SiCO-1400	12.3	Broken, white areas, fragile
SiCO-1500	30	Broken, white edges, fragile

5.3.2 FT-IR Analysis

FT-IR spectra of PMHS, DVB, the crosslinked gel and SiCO-1000 are displayed in Figure 5-4. Stretching bands corresponding to polymer functional groups are present in the crosslinked (pre-ceramic) gel. Spectrum for crosslinked material shows an almost complete reduction of the Si-H peak indicating successful crosslinking through hydrosilylation reaction.

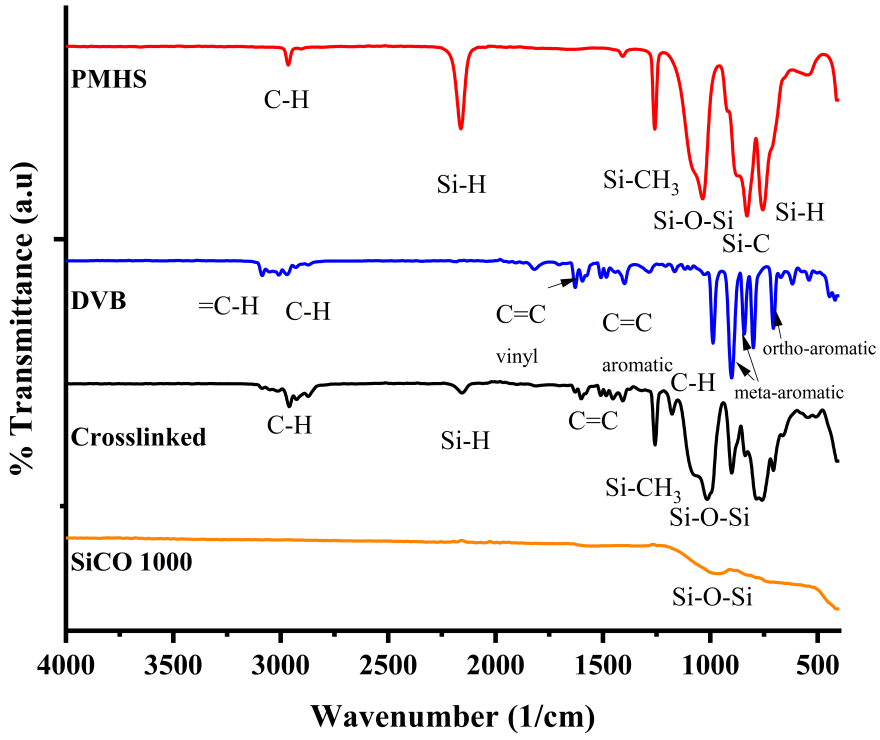

Figure 5-4 FT-IR spectra of PMHS, DVB, crosslinked gel and SiCO-1000 (from top to bottom)

5.3.3 FE-SEM Imaging

FE-SEM micrographs for annealed samples SiCO-1000 to SiCO-1500 are shown in Figure 5-5. Images of SiCO-1000 and SiCO-1100 appear smooth and without any cracks on the surface with no particular features. First cracks are visible for SiCO-1200, and SiCO-1300 shows cracks together with pores on the surface. In the micrograph for SiCO-1400, we observe whisker-like structures on the surface of the sample. These whiskers can be observed more closely in the in-set image.

Formation of these whiskers leads to cracks formed in the ceramic, which have a strong effect on the material properties. The fiber-like structures present in this SiCO ceramic were

attributed to the formation of nanocrystalline SiC.[31] The formation of whiskers at this temperature is consistent with carbothermal reduction leading to the formation of SiC nanocrystallites. The formation of SiC nanocrystallites is reported in the literature according to the following reaction: [12, 30]

$$SiO_2 + C_{(s)} \rightarrow SiO_{(g)} + CO_{(g)} \text{ and } SiO_{(g)} + 2C_{(s)} \rightarrow CO_{(g)} + SiC_{(s)}$$

Sample SiCO-1500 shows formation of spheres. As observed from the FE-SEM images, these spheres are seemingly formed as part of amalgamation or possible growing of whiskers. The FE-SEM image for SiCO-1500 shows whisker-like structures covering and around the spheres. Using this information, we suggest that spheres present on SiCO-1500 are likely formed by agglomeration or by the growth of the whiskers present in SiCO-1400. We arrived at this conclusion doing a visual analysis on the FE-SEM images, but we also use the XRD particle size analysis for SiC nanocrystallites in this work. SiC nanocrystallites are present in the XRD pattern starting from SiCO-1300 and grow in SiCO-1400, and SiCO-1500. This data is presented in detail next, but we use our XRD results to support our suggestion on the nature of the growth of the spheres present in SiCO-1500.

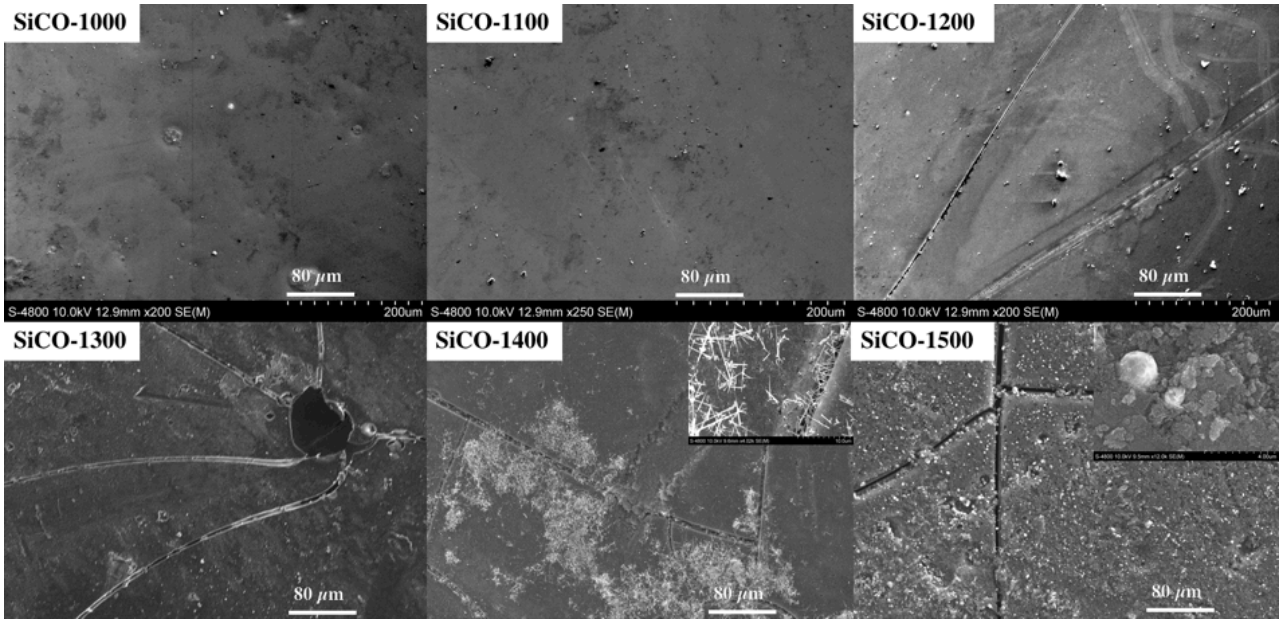

Figure 5-5 FE-SEM images for SiCO-1000 to SiCO-1500

5.3.4 XRD Results

XRD patterns of the annealed samples are shown in Figure 4. SiCO-1000, SiCO-1100, and SiCO-1200 show XRD patterns typical for amorphous SiCO.[100]

A broad “glass” hump around 22º dominates the spectrum, and no sharp diffraction peaks are visible. While the “glass” hump persists even up to 1500 °C, sample SiCO-1300 exhibits diffraction peaks at 36, 60 and 72°. These lines emerge due to the formation of β-SiC nanocrystallites.[12, 31] The “glass” hump decreases visibly in SiCO-1400 and SiCO-1500, while the peaks at 36, 60 and 72° grow sharper and more intense. Note that even the sample SiCO-1500 displays a “glass” hump besides sharp diffraction peaks, indicating a considerable amount of amorphous substance besides crystalline phases.

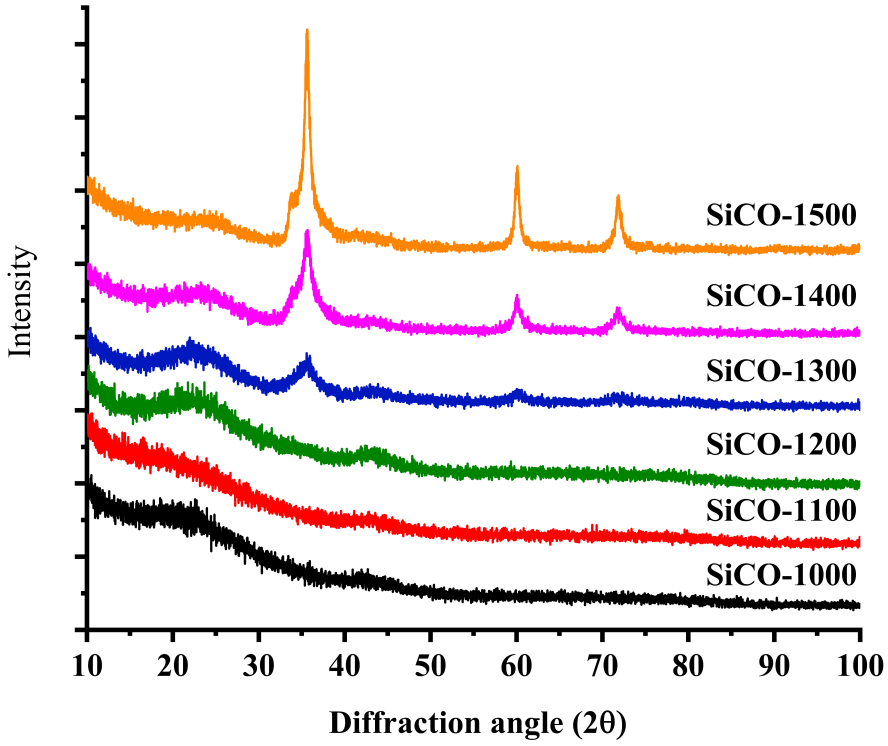

Figure 5-6 Powder XRD data for SiCO samples up to 1500 ºC (1000 to 1500 ºC from bottom to top)

It has been reported that the broad hump around 22° corresponds to the silica present in the glassy phase of these materials.[99] Diffraction peaks at 36, 60 and 72° are assigned to the formation of β-SiC nanocrystallites. SiCO-1000 to SiCO-1200 diffraction patterns reveal that the material is amorphous at these temperatures as they do not present diffraction peaks in the pattern. From literature; This result is consistent with previous studies.[99] The phase development observed in the XRD patterns is consistent with previous studies of SiCO materials produced by different routes. SiCO remains non-crystalline without sharp diffraction peaks up to 1200 °C.[57, 101] Resistance to crystallization of SiCO ceramics has been reported in the literature with phase separation starting around 1200 ºC.[31] Phase development of sol-gel

derived SiCO glasses was followed with XRD analysis.[96] The results of these analyses show that SiCO remains non-crystalline without sharp diffraction peaks up to 1200 ºC.[96, 102-103]

Notably, no diffraction peaks related to polymorphs of silica are observed up to 1500 °C.[96] An XRD pattern of PMHS and DVB system with the same composition as presented here shows a hump related to the amorphous structure at 1000 °C, and starting at 1300 °C the hump was due a glass "silica" network in the structure. Also at this temperature reflections for β-SiC nucleation starts to develop.[99] Phase separation of SiCO into SiO_2 and SiC-rich amorphous regions is typically followed by ^{29}Si NMR and traceable already in samples annealed at 1000 °C.[96] However, only SiC then crystallizes at temperatures above 1200 °C, while SiO_2 remains amorphous.

XRD patterns for some sol-gel derived SiCO ceramics were already developing XRD diffraction peaks at 1200 °C. Their results also showed that the size of β-SiC nanocrystals remained nearly constant with increasing temperature and that the size of the β-SiC nanocrystals depended on initial composition. The maximum size of the crystallites for all compositions was about 3 nm at 1500 °C.[100]

We used the diffraction peaks of Figure 5-6 related to β-SiC and estimated the grain size using the Scherrer equation.[104] We obtain diameters of β-SiC crystallites between 5±1, 9.5±2.1 and 15.5±2.1 nm for SiCO-1300, SiCO-1400, and SiCO-1500, respectively.

Previous studies have investigated the growth of SiC nanocrystals in SiCO materials. XRD analysis of sol-gel derived SiCO glasses pyrolyzed at 1400 °C have been estimated to have SiC crystallites up to 2 nm.[57]

HR-TEM studies of sol-gel derived SiCO ceramics with different compositions confirmed the presence of silicon and silicon carbide nanocrystallites with a diameter of 300 and 80 Å respectively. These results were found for SiCO ceramics annealed at 1200 °C for the TH

DH 9 composition. These crystallites grow up to a maximum of 500 Å at 1500 °C, and they are embedded in an amorphous silica matrix as identified by EDP (Electron Diffraction Patterns).[96]

Further analysis of the XRD patterns of samples SiCO-1300, SiCO-1400, and SiCO-1500 allowed us to identify small diffraction peaks for (002) reflections related to the presence of ordered graphite.

The total area covered under the diffraction line decreases with increasing temperature, consistent with the consumption of graphite in carbothermal reduction. From SiCO-1300 to SiCO-1400, the total area of the graphite peak decreases by 79%. From SiCO-1400 to SiCO-1500 the remaining area decreases by a 51% decrease in the total area of the graphite peak, yielding an overall reduction by 90%. The peak position shifts as well, from 2θ = 22.3° to 23.6° and 24.9° from SiCO-1300 to SiCO-1400 and SiCO-1500. The corresponding d-value, thus, decreases from 3.98 Å in SiCO-1300 to 3.76 Å in SiCO-1400 and 3.56 Å in SiCO-1500. Applying the Scherrer equation, we calculate a correlation length of smaller than 1 nm of the ordered domains for all samples.

High-quality graphite (SP-1), a standard crystalline graphite for research and industry, exhibits a d-value for the (002) reflection of 3.3553 Å.[105] Moreover, the interlayer distance of graphite decreases with increasing crystallinity.[106] Typical values for 2θ of graphite are 26.37° or 26.6 ° depending on the graphite reactant used in the synthesis.[107,108] Therefore, the increase in 2θ for the position of graphite diffraction lines in our data is consistent with a progressive ordering of carbon in the SiCO material as temperature is increased. However, while annealing leads to a more organized carbon phase, the diffraction patterns indicate that the extent of the ordered domains is limited.

The presence of graphitic domains and turbostratic carbon in SiCO annealed at high temperatures has been established in various TEM studies.[12,76] In another study, Raman mapping was utilized for the investigation of carbon domains in PMHS/DVB derived SiCO ceramics. It was possible to identify two different types of carbon in the vicinity of SiC

nanocrystallites. The results showed a well-organized sp^2 carbon and a disordered sp^2 carbon phase. They found that carbon domains with low-intensity D band were found in close proximity to SiC nanocrystallites, and that disordered carbon appeared to be located in the interface between the SiCO matrix and ordered sp^2 carbon.[30] Our results are consistent with the presence of an organized sp^2 carbon phase present in these materials.

Polymer derived SiCO ceramics show a decrease in carbon content percent as pyrolysis temperature is increased. This decrease can be due to volatile species being more likely to escape at higher temperatures. [32]

5.3.5 Raman Results

Raman spectroscopy is particularly well suited for the investigation of carbon-based materials. Bands in Raman spectroscopy correspond to a vibrational frequency in the material. Raman spectra of graphite show the G band that is caused by an in-plane sp^2 stretching of carbon atoms.[109] Raman spectra of (disordered graphite) carbon-based materials also display the E_{2g} symmetry (G band) positioned between around 1575 to 1595 cm^{-1}, as well as an A_{ig} symmetry band, positioned around 1350 cm^{-1}.[109]

The D and G bands are characteristic features of carbon-based materials. The D band is related to sp^2 breathing modes, and the G band is related to sp^2 bond stretching.[110] The vibrational frequency depends on laser wavelength.[111] Figure 5-6 displays the Raman spectra for samples SiCO-1000 to SiCO-1500.

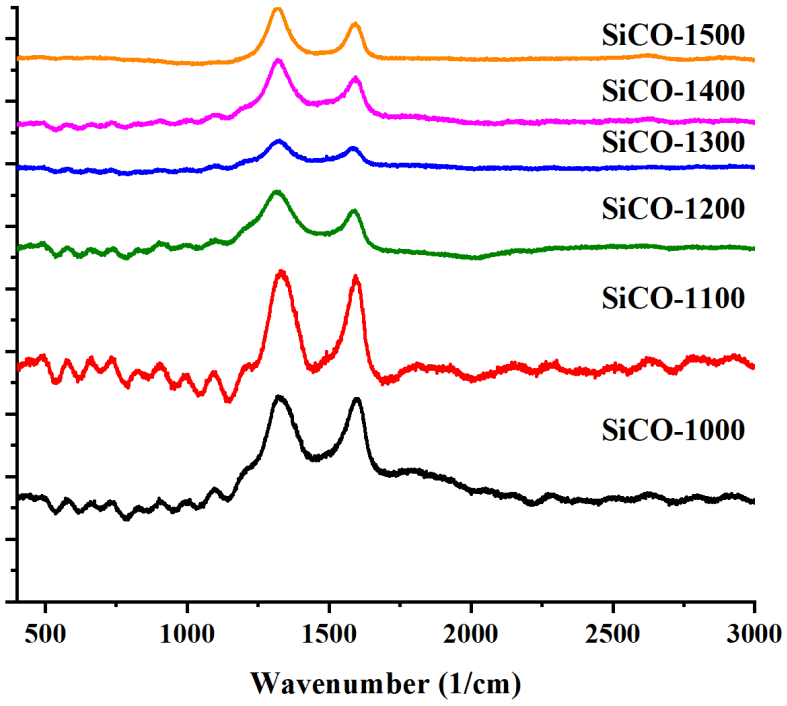

Figure 5-7 Raman spectra for SiCO samples up to 1500 ºC (1000 to 1500 ºC from bottom to top)

The Raman spectrum of single crystal graphite has been reported to have one band at 1575 cm^{-1}. For the Raman spectra of carbonaceous materials such as carbon black, vitreous carbon, or activated carbon, a second band is present around 1355 cm^{-1}.[112] The intensity increase of this second band is related to the increase of unorganized carbon structures and the decrease of the crystalline size of carbon domains.[112]

Samples SiCO-1000 to SiCO-1500 show features of a carbon-based material with disordered carbon. SiCO-1000 also displays a shoulder around 1205 cm^{-1} as well as a broad contribution that does not display maxima around (1512 cm^{-1}), but that it is positioned between the D and G bands. SiCO-1000 also displays a very broad shoulder around 1780 cm^{-1}.

SiCO-1100 also shows the D and G bands positioned at1334 and 1596 cm^{-1}, respectively. The shoulders around 1212 cm^{-1} and 1549 cm^{-1} are less prominent in comparison to SiCO-1000 and shifted to higher wavenumbers. SiCO-1200 has D and G bands positioned at 1318 and 1589 cm^{-1} respectively. Shoulders are positioned at 1271 and 1515 $cm^{-1.}$ SiCO-1300's G and D bands are positioned at 1319, and 1582 cm^{-1} and shoulders are positioned at 1214 and 1502 cm^{-1}. SiCO-1400 has D and G peaks positioned at 1333, and 1589 cm^{-1} and shoulders are located at 1277 and 1447 cm^{-1}. SiCO-1500's D and G peaks are located at 1318, and 1590 cm^{-1} and small shoulders are present at 1236 and 1478 cm^{-1}.

Samples SiCO-1000 to SiCO-1500 display a shoulder around 1200 cm^{-1} that shifts to higher wavelengths from SiCO-1000 to SiCO-1500 and decreases with increasing temperature. This shoulder can be related to C-C-sp^3 vibrations.[111] This shoulder is also reported in the literature to correspond to hydrocarbons or aliphatic moieties connected to graphitic basic structural units[113]. Also, around 1500 cm^{-1} a shoulder is visible for SiCO samples and becomes increasingly smaller at 1500 °C. This shoulder is related to amorphous carbon.[113] The decrease of the shoulder around 1500 cm^{-1} is consistent with higher ordering of carbon domains as temperature is increased.

The presence of D and G bands for SiCO ceramics obtained at 1000 °C is supported by literature data.[114] SiCO aerogels (PMHS: DVB, mass ratio of 1:2) annealed at 900 °C show D and G bands at 1331 and 1598 cm^{-1} respectively (using a 514 nm laser).[20] These band positions correspond to the ones presented here for the SiCO-1000 sample. These bands correspond to disordered carbon domains.[109-110] As temperature increases, the D & G bands become narrower, and FWHM decreases, indicating increasing ordering of carbon domains.[31, 99] D and G peaks slightly move to lower wavenumbers for samples SiCO-1200 to SiCO-1500. For sample SiCO-1500, D and G are positioned at 1316 and 1589 cm^{-1}. Therefore, there is an overall shifting to lower wavenumbers for the D and G peaks in these samples.

Formation of disordered carbon as evidenced by Raman is facilitated by using a carbon enhancer as DVB. Using DVB as a crosslinker enhances the free carbon in the SiCO ceramic.[12, 28, 32, 115] Previous studies have investigated the thermal conversion of PMHS and DVB.[30, 32] The results show that the use of DVB as a crosslinker increases the carbon content in a more controlled manner in comparison to tetramethyl tetravinyl cyclotetrasiloxane (TMTVS) or methyl, vinyl, or phenyl groups connected to silicon atoms. It was noted that the aromatic groups present in DVB in the pre-ceramic stage allow for the formation of graphitic like carbon starting at 800 °C in inert atmosphere and shown in the Raman spectrum.[114] DVB promotes the formation of sp^2 carbon because it already contains aromatic groups in the structure.

It is possible to gain more information about the carbon present in these samples by using graphitization indicators. These can provide information about the carbon domain size in these materials. The lateral crystal size (L_a) of segregated carbon sites can be obtained[116] as well as the inter-defect distance using the ratio of the D and G peaks.[117] For the calculation of the lateral size of carbon domains and inter-defect distance, the following formulas were applied, respectively. Table 5-2 summarizes the results for the graphitization indicators.

$$L_a\,(\text{nm}) = 2.4\ x\ 10^{-10} \cdot \lambda_L^4 \cdot \left(\frac{A_D}{A_G}\right)^{-1}$$

$$L_D^2\,(\text{nm}^2) = 1.8\ x\ 10^{-9} \cdot \lambda_L^4 \cdot \left(\frac{A_D}{A_G}\right)^{-1}$$

Table 5-2 Graphitization Indicators Calculated Using Raman Results

Sample	D-band Center Position	G band center Position	D-band Area	G band area	A_D/A_G	L_a (nm)	L_d (nm)
SiCO-1000	1329	1597	215170	74944	2.87	13.42	10.03
SiCO-1100	1334	1596	162923	72233	2.26	17.08	11.32
SiCO-1200	1318	1589	89611	33647	2.66	14.47	10.42
SiCO-1300	1319	1582	36249	12528	2.89	13.32	9.99
SiCO-1400	1321	1589	50256	30073	1.67	23.06	13.15
SiCO-1500	1318	1590	67901	31333	2.17	17.78	11.55

From the graphitization indicators; we calculated for SiCO-1000 to SiCO-1500 a lateral domain (L_a) of 13.42 nm, 17.08, 14.47, 13.32, 23.06, and 17.78 nm respectively. Also, the inter-defect distance (L_d) for SiCO-1000 to SiCO-1500 was 10.03, 11.32, 10.42, 9.99, 13.15, and 11.55 nm, respectively. Overall, the lateral size for the graphitic domains and the inter-defect distance increase with increasing temperature for SiCO-1000 to SiCO-1500.

SiCO samples synthesized with the same PMHS: DVB ratio showed narrowing from D and G peaks in Raman spectra when going from 1000 to 1300 ºC. Their results showed an increase in the estimated graphite crystal size from 11.1 nm at 1000 C to 13.1 nm at 1300 ºC. As well as a shifting to lower wavenumbers for the D and G peak with temperature increase.[99] Our results show similar lateral size domains for SiCO-1000 and SiCO-1300 around 13 nm and shifting D and G bands to lower wavenumbers as well. Our results for lateral size domains for SiCO-1000 to SiCO-1300 decreases slightly in this study, but the overall trend is an increase of lateral size domains with increasing temperature. These results show that the trend is not consistent for all samples. SiCO-1400 displays the largest L_a. of all samples, and we believe that this inconsistent growth of graphitic-like domains can be related to the loss of carbon, related to carbothermal reduction, which is well reported for SiCO materials.

In another study, sol-gel derived SiCO ceramics have shown a decrease in carbon content of about 6 % and a decrease of more than half in the size of carbon nano-domains when

samples are annealed from 1100 to 1500 °C.[118] This loss of carbon content is related to the onset of carbothermal reduction around 1400 °C.[12]

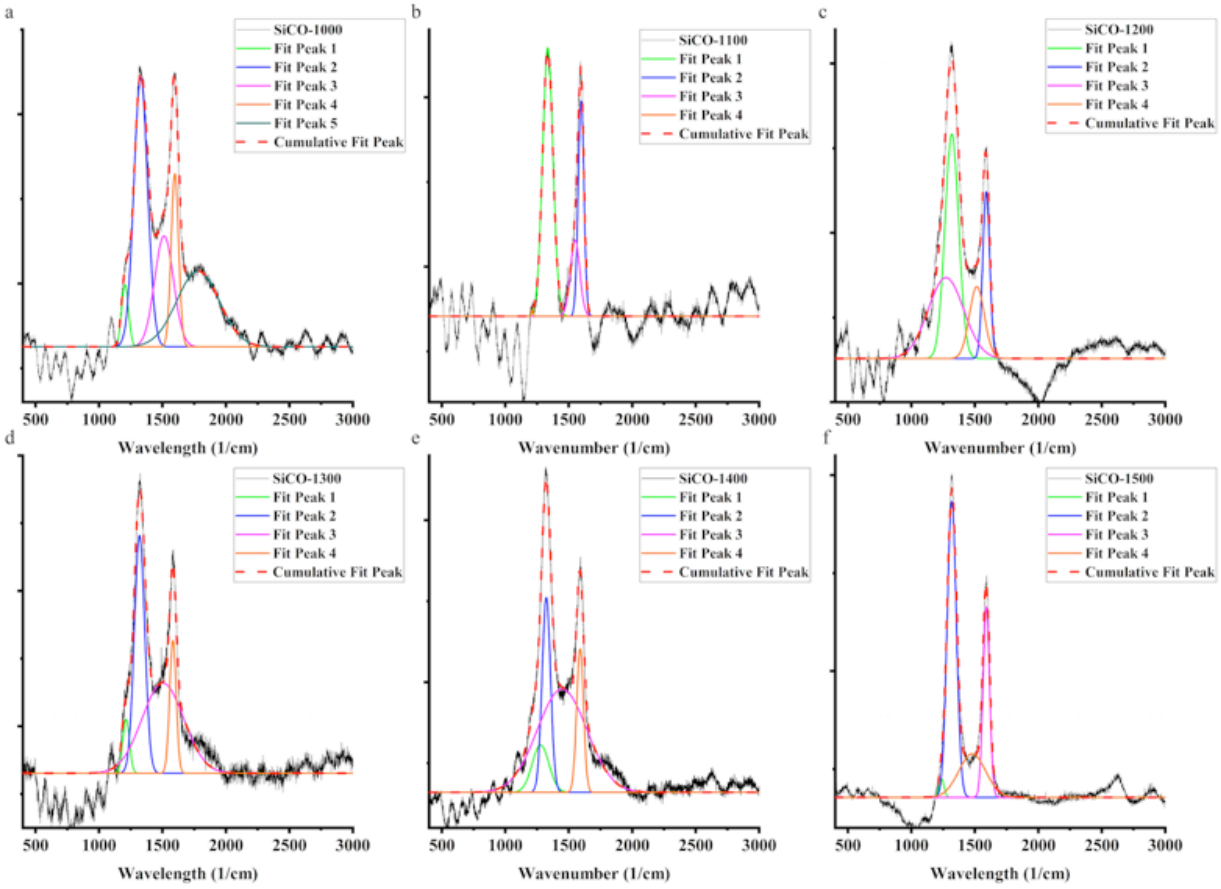

Figure 5-8 SiCO-1000 to SiCO-1500 (from a) to f)) fitted using Origin software after baseline correction

Figure 5-8 compares the Raman spectra of the SiCO-1000 to SiCO-1500 samples. All samples are fitted using 4 Gaussians but SiCO-1000. SiCO-1000 displays a prominent peak that is centered at 1780 cm^{-1}. This peak has been fitted because it proved necessary to achieve a good fit. This large shoulder does not correspond to shoulders or peaks reported in

literature for carbonaceous materials.[113, 119-120] We suspect that it can be related to fluorescence effects. Fluorescence effects have been reported in the literature for SiCO materials, and D & G peaks have not been discernible due to a large fluorescence background.[111] In our results, D & G peaks are still observable for all samples, but we suggest that fluorescence could be causing shoulders in the spectra not reported to be part of D and G peak deconvolution for carbonaceous materials. Also, this shoulder decreases with increasing temperature, and it has been reported that D & G peaks are easier to observe and more defined at higher temperatures.[96,111] This observation is consistent with Raman results we have obtained here. Results show that with increasing annealing temperature, the D and G peaks become narrower and more defined.

5.3.6 TGA Results

TGA in air was done to investigate the oxidation resistance of these ceramics up to 900 °C in air. For sample SiCO-1000, a final mass loss of 3.5% is observed. SiCO-1100 and SiCO-1200 show a mass loss of less than 1%. Mass loss from SiCO-1200 to SiCO-1300 is 3.5%, from SiCO-1300 to SiCO-1400 there is a mass loss of 15%, and this increases to a final mass loss of 33% for SiCO-1500.

Thermal analysis coupled with emission gas analysis shows hydrogen evolution of SiCO ceramics up to 1200 °C. Mass loss is attributed to hydrogen presence being significant in SiCO ceramics at these temperatures.[65]

The large mass loss % present in SiCO-1400 and SiCO-1500 can be attributed to the high amount of carbon present in the structure[121], which is related to the incorporation of DVB in the material. In a previous report, a TGA analysis in air of SiCO foams annealed up to 1200 °C showed a mass drop around 600 °C, this mass loss was attributed to free carbon in the ceramic material.[122] This free carbon produced CO_2 gas evolution. In this report, the free carbon was attributed to the polyurethane foam residue in the SiCO foams. In this study, reheating the SiCO foams up to 1000 °C caused little weight loss when TGA was performed in air or oxygen

atmosphere. This result showed that a SiCO foam ceramic annealed at 1200 °C presents high oxidation resistance up to 1000 °C.[122] In our results, SiCO-1200 has a mass loss of 0.62% when exposed to air up to 900 °C.

In a separate study, the oxidation of SiCO ceramics with different compositions (annealed at 1200 °C) and derived from silsesquioxanes was studied.[123] This study showed that the most critical oxidation process causing the largest mass loss occurred within 0.5 hours of the initial oxidation procedure. Also, their results showed that SiCO ceramics with high excess free carbon were fully oxidized to silica (SiO_2) at 600 and 800 °C and still contained quantifiable amounts of excess carbon content after 500 hours of oxidation time at 1000 and 1200 °C. In contrast, for SiCO ceramics with low carbon content, there was no complete oxidation to SiO_2 with up to 500 hours of oxidation time. Results also showed that for all compositions, 800 °C was the most critical temperature in terms of more composition changes due to oxidative processes. They also observed that lower oxidation temperatures (600 and 800 °C) are associated with loss of carbon in the form of CO and CO_2. This reaction creates pores in the sample, which provides oxygen better accessibility to bulk sample and allows Si-C bond oxidation. At higher oxidation temperatures (1000 and 1200 °C) SiO_2 is formed on the surface of the ceramic that slows down the oxidation processes throughout the bulk material. [123]

In our results, SiCO-1400 and SiCO-1500 show significant mass loss % around 600 °C. This mass loss % could be associated with SiCO phase separation at higher temperatures and materials having a high amount of carbon content forming a free carbon phase. A turbostratic carbon phase is shown to be present in these materials in the Raman analysis.

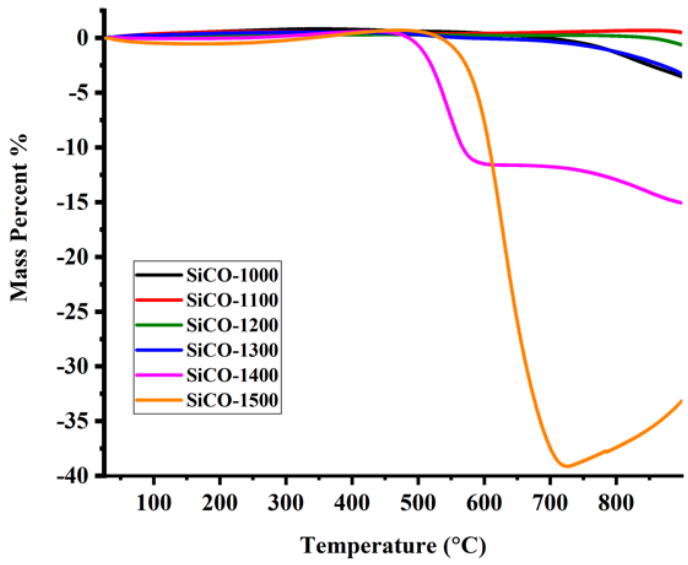

Figure 5-9 TGA analysis in air for samples SiCO-1000 to SiCO-1500

Table 5-3 Final Mass Loss % for TGA in Air for Samples SiCO-1000 to SiCO-1500

Sample	Final Mass Loss %
SiCO-1000	3.5
SiCO-1100	0.50
SiCO-1200	0.62
SiCO-1300	3.2
SiCO-1400	15
SiCO-1500	33

In a study performed by Lu et al., 2016, PMHS crosslinked with 80% content of DVB was studied. The samples show oxidation resistance in air up to 1000 ºC with a maximum weight gain of less than 0.5%. This study also showed a correlation between mass loss percentage and pyrolysis temperature. TGA analysis shows that PMHS/DVB derived SiCO ceramics exposed to lower pyrolysis temperatures show lower mass changes, and higher pyrolysis temperatures lead to weight gain before the onset of weight loss at around 800 °C.

Less than 0.2% weight loss was obtained for samples annealed at 1200 and 1300 ºC, and a 0.5% weight loss was obtained for a sample annealed at 1500 ºC.[32] Their results pointed out to the decreased stability of the SiCO network with increasing temperature as well as increased segregation of the SiCO ceramic. Our results show a significant increase in the weight loss percentage as annealing temperature is increased, but it is also important to note that the carbon content in our samples corresponds to 200% content of DVB with respect to PMHS.

In another TGA study, oxidation stability of sol-gel derived SiCO ceramics was compared to PMHS/DVB derived ceramics. This study showed that PMHS/DVB derived SiCO ceramics show increased resistance to oxidation in comparison to sol-gel SiCO ceramics. Results obtained for sol-gel derived SiCO show increased oxidation at 700 °C in comparison to PMHS/DVB derived SiCO ceramics with comparable amounts of carbon.[55] These results suggest that the PDC route can have improved oxidation resistance in comparison to the sol-gel method. Figure 5-9 illustrates the TGA of the SiCO-1000 to SiCO-1500 performed in air atmosphere, and table 5-3 summarizes the results.

5.3.7 Discussion

SiCO ceramics were synthesized using PMHS and DVB with an average ceramic yield was 66±1, and linear shrinkage was 28±1. Literature reports yields between 60 and 65% for these materials.[63, 99] Our results are consistent with reported data.

Further annealing in Argon atmosphere up to 1500 ºC for SiCO ceramics yielded a mass loss of less than 1% for SiCO-1000 to SiCO-1300, and increased mass loss for SiCO-1400 and SiCO-1500, having a final mass loss of 30%.

Samples SiCO-1000 to SiCO-1200 are black and shiny, SiCO-1300 starts to appear fragile and powdery, and SiCO-1400 and SiCO-1500 are broken with white areas on the surface.

FE-SEM imaging results show almost featureless surfaces for SiCO-1000 and SiCO-1100, SiCO-1200 shows the formation of some large cracks on the surface. In SiCO-1300, cracks become more pronounced, and pores are formed. SiCO-1400 whisker-like structures form on

the surface of the sample. The formation of whiskers at this temperature is consistent with the formation of SiC nanocrystallites. For SiCO-1500, spheres are formed on the surface of the sample. These spheres are formed from the agglomeration or growth of whiskers present in SiCO-1400.

Powder XRD results show typical amorphous XRD patterns for SiCO-1000 to SiCO-1200. SiCO-1300 displays small peaks 36, 60 and 72° start developing. These peaks are assigned to the formation of β-SiC nanocrystallites. Also, at this temperature, a more pronounced hump around 22° in 2θ corresponds to silica in the glassy phase[99]. SiCO-1400 and SiCO-1500 show more pronounced peaks corresponding to β-SiC nanocrystallites.

Scherrer particle size analysis for SiCO-1300 to SiCO-1500 showed an increasing β-SiC particle size estimation. SiCO-1300 β-SiC particle size was estimated to be between 4 and 6 nm. β-SiC particle size increased up to a range of 14-17 nm for SiCO-1500. This result shows an increase in crystallite size with increasing temperature of annealing, which has been reported before for sol-gel SiCO ceramics[57], and the growth of SiC nanocrystallites is reported for PDC ceramics.[31]

From the powder XRD pattern, it was possible to locate small and decreasing peaks related to graphite. The correlation length was less than 1 nm for SiCO-1300 to SiCO-1500. The d(Å) decreased with increasing temperature, and 2θ value shifted from 22.3º to 24.9º, which suggests increasing ordering of the graphitic like carbon phase present in these materials. These results are consistent with increased ordering of carbon domains with increasing temperature. This result is consistent with Raman spectra, and it is well reported in literature. Also, with increasing temperature, the D & G bands become narrower, and FWHM decreases, indicating increased ordering of carbon domains as reported in the literature.[31, 99]

To calculate L_a and L_d, graphitization indicators were used in this study. Our results indicate that L_a increase with increasing temperature but decrease around 1200 and 1300 ºC, and there is a final L_a of 17.78 nm. L_d increase with increasing temperature except for 1200 and 1300 ºC

as well. We do not have conclusive reasoning for this effect yet, but it can be related to carbon distribution changes.

Previous studies performed with the same material show an increase in L_a domains from 1000 to 1300 ºC from 11.1 nm to 13.1 nm. Our results at these temperatures show a slight decrease in L_a from 13.42 to 13.32 nm from 1000 to 1300 ºC. However, our results show an overall increase when going from 1000 to 1500 ºC.

TGA analysis in air was done up to 900 ºC show that SiCO-1000 has a final mass loss of 3.5%. SiCO-1100 and SiCO-1200 show a mass loss of less than 1%. Also, SiCO-1300 to SICO-1500 mass loss increases from 3.2% to 15% (for SiCO-1400), and there is a final mass loss of 33% for SiCO-1500.

5.4 Conclusion

We investigated bulk SiCO ceramics when annealed up to 1500 ºC using Raman, XRD, FE-SEM, and TGA analysis. Using Raman Spectroscopy, we found that L_a domains of graphitic carbon increase with increasing temperature up to 17.8 nm and L_d increase with increasing temperature of annealing up to 11.6 nm.

From XRD analysis, we obtained information about the progressive increment of SiC crystalline growth as well as the presence of small and decreasing graphite peaks with increasing annealing temperature. The XRD analysis provides information about the formation of graphite in these materials, and a correlation length of less than 1 nm was calculated for SiCO-1300 to SiCO-1500. XRD and Raman analysis support the increasing arrangement of the free carbon phase present in these SiCO ceramics.

Chapter 6

General Summary

6.1 Chapter 1

Chapter 1 of this thesis dissertation introduces the term aerogel, which was first coined by Kistler; we also introduce aerogel properties and applications. Also, in chapter 1, we introduce silicon oxycarbide ceramics which belong to the PDC materials. These materials possess a free carbon phase that affects stability and thermal conductivity.

Due to the low solubility of around 1% of carbon in silica, conventional solid-state methods are not feasible for the synthesis of SiCO materials. This limitation is why the PDC route provides a synthesis method that allows SiCO materials in a range of compositions, shapes, and properties. More specifically, we talked about SiCO aerogels; these are porous materials synthesized using the PDC method and subsequent supercritical drying. The supercritical method allows for minimal pore collapse due to the almost complete elimination of capillary forces. SiCO aerogels have been synthesized and characterized for gas sensing, anodes for Li-ion batteries, water cleaning and more.

6.2 Chapter 2

In chapter 2, we investigate how the synthesis conditions of PDC SiCO aerogels influence their microstructural properties. After having established a successful synthesis method, we look at solvent effects on aerogel microstructure. We synthesized SiCO aerogels by crosslinking poly(methylhydrosiloxane) and divinylbenzene (PMHS and DVB) in highly diluted conditions. We used four different solvents (n-hexane, cyclohexane, tetrahydrofuran, and acetone). We performed the synthesis using a digestion vessel and a Pt catalyst. We used solvent exchange with liquid CO_2 and supercritical drying in CO_2 to obtain a porous material. We investigated the microstructural features of the resulting aerogels and found that solubility and swelling of the crosslinked polymer play a significant role in the pore formation process of these materials.

6.3 Chapter 3

In chapter 3, we synthesized SiCO porous materials using a different synthesis method. In this chapter, we present the synthesis of highly porous silicon oxycarbide ceramics synthesized using the sol-gel method. We used 1,2 Bis(triethoxysilyl)ethane and dissolved it in isopropanol and used HCl as the catalyst. These materials were slowly dried at 45 ºC until the material dried. Then we anneal these materials in inert atmosphere to convert them to SiCO ceramics. We investigate their microstructural features before and after annealing. We also characterize SiCO ceramics and their ability to adsorb Methylene blue (MB) dye. We compare SiCO porous materials to mesoporous silica and activated carbon. Our results conclude that the material with the highest specific surface area (SSA) does not necessarily display the highest adsorption capacity. In this study, SiCO outperforms mesoporous silica and activated carbon even though it possesses the least SSA. Our results show a complete reduction of MB dye characteristic UV-Vis absorption peak after overnight contact. In contrast; overnight contact with activated carbon and mesoporous silica resulted in an 80 % reduction of UV-Vis characteristic absorption peak of MB dye; despite of their higher SSA_{BET}.

6.4 Chapter 4

In chapter 4, we take a close look into the structural evolution of SiCO porous materials (ambigels) synthesized through the sol-gel method and using ambient drying. We annealed the SiCO ambigels at 400, 600, 800 and 1000 ºC. For all samples, we obtained narrow pore size distributions using the BJH method using nitrogen adsorption analysis. We also observed a decrease of 4 % in the average pore diameter of these materials upon annealing. FE-SEM imaging was used to investigate the microstructure of SiCO ambigels. The average particle size decreased upon annealing temperature. These results point out that particle size, as well as pore diameter, play a role in the specific surface area of these SiCO ambigels. Further experiments such as dynamic hysteresis scanning can be required to investigate the pore properties of these materials further.

Nitrogen adsorption analysis is summarized with the following results: SSA_{BET} decreases 25% from unannealed material to SiCO material annealed at 400 ºC and increases 10% from 400 to 600 ºC. There is an overall final SSA_{BET} loss of 55% from unannealed material to SiCO material annealed at 1000 ºC.

The pore volume calculated using the BJH model shows a decrease of 36% from unannealed SiCO to annealed material at 400 ºC. There is a 13% increase in pore volume from 400 to 600 ºC and an overall final decrease of 61%. The average pore diameter for all the samples is 3.56±0.05 nm. There is an overall average pore diameter decrease of 4%. These results indicate that the calculated average pore diameter does not change significantly up to 1000 ºC.

6.5 Chapter 5

In the last chapter, we present an investigation of bulk SiCO ceramics; we characterized the properties of bulk SiCO ceramics when exposed up to 1500 °C in Argon atmosphere. Dense monolithic SiCO ceramics are synthesized through the polymer-derived ceramic (PDC) route using polymethylhidrosiloxane (PMHS) and divinylbenzene (DVB). We present a systematic investigation of a 1:2 mass ratio of PMHS: DVB SiCO ceramics annealed from 1000 to 1500 °C.

In this chapter, we show the phase separation of these materials. XRD analysis shows β-SiC nanocrystalline growth; along with small graphite peaks starting at 1300 ºC, which decrease with increasing annealing temperature. Also, using Raman analysis, we show the increasing ordering of carbon domains present in these materials.

Using Raman spectroscopy, we found that L_a domains of graphitic carbon increase with increasing temperature up to 17.8 nm and L_d increase with increasing temperature of annealing up to 11.6 nm. The XRD analysis provides information about the formation of graphite in these materials, and a correlation length of less than 1 nm was calculated for SiCO-1300 to SiCO-1500.

6.6 Overall Summary and Future Directions

The goal of this research was to contribute to the field of ceramics by the investigation of the ternary system of SiCO materials synthesized through the PDC (Polymer Derived Ceramic) route and sol-gel route. Results in chapter 2 can be of interest to researchers performing investigations of polymer-derived aerogels. We synthesized SiCO aerogels and studied polymer solubility and swelling as important factors in the microstructural features of SiCO aerogels. We used our results to provide a rationale for “good” and “bad” solvents. Future research can be performed to obtain Hansen solubility parameters for PMHS polymer as well as providing a rationale for their importance in the synthesis of aerogels.

Chapters 3 and 4 show the synthesis of porous SiCO ambient-dried materials. This synthesis method offers advantages over the aerogel method. Advantages include ease of synthesis, no need for digestion vessel and supercritical dryer chamber. This synthesis method makes the ambient drying method less expensive and less complicated. One disadvantage of the ambient dried method is long drying times. A critical advantage of the ambient dried method is that the SSA of materials can be significantly higher in comparison to the aerogel synthesis method.

This synthesis method can be further explored to gain information about applications in the field of environmental remediation. Future experiments in this field would provide insight into the applicability of SiCO materials in water cleaning of different contaminants and concentrations. A systematic comparison of porous SiCO to commercially and currently available materials could provide an alternative to alleviate water pollution issues.

Results from chapter 4 provide insight into pore and particle size development during the annealing process. Findings can be useful to tailor porous SiCO materials. More insight into the temperature-dependent microstructural feathers can facilitate the understanding of the

effects of heating treatment in these materials. Further experiments can be focused on pore and particle size development as a function of higher times and temperatures of exposure.

Chapter 5 focuses on the high-temperature behavior of SiCO ceramics up to 1500 ºC. SiCO ceramics are investigated for their high-temperature applications. The results provided in this thesis provide a comprehensive analysis looking closely at the temperature-dependent changing SiCO structure. Future experiments will be needed to understand the chemical bonding evolution of these PMHS/DVB materials using XPS and NMR experiments.

Appendix A

Publication Information and Contributing Authors

Chapter 2. Parts of this chapter correspond to a manuscript published in Materials. Aguirre-Medel, S., Jana, P., Kroll, P., & Sorarù, G. D. (2018). Towards Porous Silicon Oxycarbide Materials: Effects of Solvents on Microstructural Features of Poly(methylhydrosiloxane)/Divynilbenzene Aerogels. *Materials (Basel, Switzerland)*, *11*(12), 2589. doi:10.3390/ma11122589

Chapter 3. A manuscript in preparation. Aguirre-Medel, S., Kroll, P. Synthesis of ambient dried SiCO materials and their potential for environmental remediation

Chapter 4. A manuscript in preparation. Aguirre-Medel, S., Kroll, P. Sol-gel SiCO Ambigels Microstructural Evolution Upon Pyrolysis Temperature

Chapter 5. A manuscript in preparation. Aguirre-Medel, S., Hendrix, K., Kroll, P. Investigation of Microstructural Evolution of Bulk SiCO Ceramics Annealed up to 1500 °C

References

1. Pierre, A. C.; Pajonk, G. R. M. Chemistry of Aerogels and Their Applications. *Chem. Rev.* **2002**, *102*, 4243-4265.

2. Gesser, H. D.; Goswami, P. C. Aerogels and Related Porous Materials *Chem. Rev.* **1989**, *89*, 765-788.

3. Mulder, C. A. M.; Lierop, J. G. V. *In Aerogels*. Springer: Berlin, 1986.

4. Gurav, J. L.; Jung, I.-K.; Park, H.-H.; Kang, E. S.; Nadargi, D. Y. Silica Aerogel: Synthesis and Applications. *J. Nanomat.* **2010**, *2010*, 1-11.

5. Du, A.; Zhou, B.; Zhang, Z.; Shen, J. A Special Material or a New State of Matter: A Review and Reconsideration of the Aerogel. *Materials.* **2013**, *6* (3), 941-968.

6. Kistler, S. Coherent Expanded Aerogels and Jellies. *Nature.* **1931**, *137* (3211), 741.

7. Colombo, P.; Mera, G.; Riedel, R.; Sorarù, G. D. Polymer-Derived Ceramics: 40 Years of Research and Innovation in Advanced Ceramics. *J. Am. Chem. Soc.* **2010**, *93* (7), 1805-1837.

8. Vomiero, A.; Modena, S.; Soraru, G. D.; Raj, R.; Blum, Y.; Della Mea, G. Investigation on the Oxidation Process of SiCO Glasses by the Means of Non-Rutherford Backscattering Spectrometry. Nucl. Instrum. Methods Phys. Res. **2003**, *211* (3), 401-407.

9. Riedel, R.; Mera, G.; Hauser, R.; Klonczynsky, A. Silicon-Based Polymer-Derived Ceramics Synthesis, Properties and Applications- A Review. *J. Ceram. Soc. Jpn.* **2006**, *114* (6), 425-444.

10. Sorarù, G. D.; Pederiva, L.; Latournerie, J.; Raj, R. Pyrolysis Kinetics for the Conversion of a Polymer into an Amorphous Silicon Oxycarbide Ceramic. *J. Am. Ceram. Soc.* **2002**, *85* (9), 2181-87.

11. Martínez-Crespiera, S.; Ionescu, E.; Kleebe, H.-J.; Riedel, R. Pressureless Synthesis of Fully Dense and Crack-Free SiOC Bulk Ceramics via Photo-crosslinking and Pyrolysis of a Polysiloxane. *J. Eur. Ceram. Soc.* **2011**, *31* (5), 913-919.

12. Kleebe, H.-J.; Blum, Y. D. SiOC Ceramic with High Excess Free Carbon. *J. Eur. Ceram. Soc.* **2008**, *28* (5), 1037-1042.

13. Saha, A.; Raj, R. Crystallization Maps for SiCO Amorphous Ceramics. *J. Amer. Ceram. Soc.* **2007**, *90* (2), 578-583.

14. Kroll, P. Searching Insight into the Atomistic Structure of SiCO Ceramics. *J. Mater. Chem.* **2010**, *20* (46), 10528.

15. Nimmo, J. P.; Kroll, P. First-Principles Calculations and Analysis of ^{29}Si Nuclear Magnetic Resonance Chemical Shifts in Silicon Oxycarbide Ceramics. *J. Phys. Chem. C.* **2014**, *118* (51), 29952-29961.

16. Stabler, C.; Roth, F.; Narisawa, M.; Schliephake, D.; Heilmaier, M.; Lauterbach, S.; Kleebe, H.-J.; Riedel, R.; Ionescu, E. High-Temperature Creep Behavior of a SiOC Glass Ceramic Free of Segregated Carbon. *J. Eur. Ceram. Soc.* **2016**, *36* (15), 3747-3753.

17. Godoy, N. V.; Segatelli, M. G. Kinetic Investigation of Thermal Formation Processes of SiOC Glasses Derived from C-Containing Hybrid Polymeric Networks. *J. Braz. Chem. Soc.* **2015**, *26* (5), 899-909.

18. Tamayo, A.; Rubio, J.; Rubio, F.; Oteo, J. L.; Riedel, R. Texture and Micro-Nanostructure of Porous Silicon Oxycarbide Glasses Prepared from Hybrid Materials Aged in Different Solvents. *J. Eur. Ceram. Soc.* **2011**, *31* (9), 1791-1801.

19. Karakuscu, A.; Ponzoni, A.; Aravind, P. R.; Sberveglieri, G.; Soraru, G. D.; Kleebe, H. J. Gas Sensing Behavior of Mesoporous SiOC Glasses. *J. Amer. Ceram. Soc.* **2013**, *96* (8), 2366-2369.

20. Vallachira Warriam Sasikumar, P.; Zera, E.; Graczyk-Zajac, M.; Riedel, R.; Soraru, G. D.; Dunn, B. Structural Design of Polymer-Derived SiOC Ceramic Aerogels for High-Rate Li Ion Storage Applications. *J. Amer. Ceram. Soc.* **2016**, *99* (9), 2977-2983.

21. Bruzzoniti, M. C.; Appendini, M.; Rivoira, L.; Onida, B.; Del Bubba, M.; Jana, P.; Sorarù, G. D. Polymer-Derived Ceramic Aerogels as Sorbent Materials for the Removal of Organic Dyes from Aqueous Solutions. *J. Amer. Ceram. Soc.* **2018**, *101* (2), 821-830.

22. Zhao, W.; Shao, G.; Jiang, M.; Zhao, B.; Wang, H.; Chen, D.; Xu, H.; Li, X.; Zhang, R.; An, L. Ultralight Polymer-Derived Ceramic Aerogels with Wide Bandwidth and Effective Electromagnetic Absorption Properties. *J. Eur. Ceram. Soc.* **2017**, *37* (13), 3973-3980.

23. Sorarù, G. D.; Dalcanale, F.; Campostrini, R.; Gaston, A.; Blum, Y.; Carturan, S.; Aravind, P. R. Novel Polysiloxane and Polycarbosilane Aerogels via Hydrosilylation of Preceramic Polymers. *J. Mater. Chem.* **2012**, *22* (16), 7676.

24. Pradeep, V. S.; Ayana, D. G.; Graczyk-Zajac, M.; Soraru, G. D.; Riedel, R. High Rate Capability of SiOC Ceramic Aerogels with Tailored Porosity as Anode Materials for Li-ion Batteries. *Electrochim. Acta* **2015**, *157*, 41-45.

25. Aravind, P. R.; Soraru, G. D. Porous Silicon Oxycarbide Glasses from Hybrid Ambigels. *Micropor. Mesopor. Mat.* **2011**, *142* (2-3), 511-517.

26. Aravind, P. R.; Soraru, G. D. High Surface Area Methyltriethoxysilane-Derived Aerogels by Ambient Pressure Drying. *J. of Porous Mat.* **2010**, *18* (2), 159-165.

27. Dirè, S.; Borovin, E.; Narisawa, M.; Sorarù, G. D. Synthesis and Characterization of the First Transparent Silicon Oxycarbide Aerogel Obtained through H_2 Decarbonization. *J. Mater. Chem. A* **2015**, *3* (48), 24405-24413.

28. Blum, Y. D.; MacQueen, D. B.; Kleebe, H.-J. Synthesis and Characterization of Carbon-Enriched Silicon Oxycarbides. *J. Eur. Ceram. Soc.* **2005**, *25* (2-3), 143-149.

29. Kleebe, H.-J.; Gregori, G.; Babonneau, F.; Blum, Y. D.; MacQueen, D. B.; Massed, S. Evolution of C-rich SiOC Ceramics Part I. Characterization by Integral Spectroscopic Techniques: Solid-state NMR and Raman Spectroscopy. *Int. J. Mat. Res* **2006**, *97* (6).

30. Hourlier, D.; Venkatachalam, S.; Ammar, M.-R.; Blum, Y. Pyrolytic Conversion of Organopolysiloxanes. *J. Anal. Appl. Pyrol.* **2017**, *123*, 296-306.

31. Sasikumar, P. V. W.; Blugan, G.; Casati, N.; Kakkava, E.; Panusa, G.; Psaltis, D.; Kuebler, J. Polymer Derived Silicon Oxycarbide Ceramic Monoliths: Microstructure development and associated materials properties. *Ceram. Int.* **2018**, *44* (17), 20961-20967.

32. Lu, K.; Erb, D.; Liu, M. Thermal Stability and Electrical Conductivity of Carbon-Enriched Silicon Oxycarbide. *J. Mater. Chem. C.* **2016**, *4* (9), 1829-1837.

33. Brus, J.; Kolar, F.; Machovic, V.; Svitilova, J. Structure of Silicon Oxycarbide Glasses Derived from Polyhydridomethlysiloxane and Poly[methyl(phenyl)siloxane]. *J. Non-Cryst. Solids* **2001**, *289*, 62-74.

34. Hüsing, N.; Schubert, U. Aerogels—Airy Materials- Chemistry, Structure, and Properties. *Angew. Chem. Int. Ed.* **1998**, *37*, 22-45.

35. Pierre, A. C.; Rigacci, A., SiO_2 Aerogels. *Eds. Springer New York: New York, NY* **2011**, 21-45.

36. Maleki, H.; Durães, L.; Portugal, A. An Overview on Silica Aerogels Synthesis and Different Mechanical Reinforcing Strategies. *J. Non-Cryst. Solids* **2014**, *385*, 55-74.

37. Hansen, C. M. The Three Dimensional Solubility Parameter and Solvent Diffusion Coefficient, Their Importance in Surface Coating Formulation. Dissertation, Technical University of Denmark (DTU), Danish Technical Press, Copenhagen. **1967**.

38. Hansen, C. M.; Durkee, J.; Kontogeorgis, G.; Panayiotou, C.; Williams, L.; Poulsen, T.; Priebe, H.; Redelius, P. Hansen Solubility Parameters A User's Handbook; 2nd Edition, CRC Press: Boca Raton. **2007**.

39. Zeng, W.; Du, Y.; Xue, Y.; Frisch, H. L. *Solubility Parameters in Physical Properties of Polymers Handbook*. Springer Science+Business Media, LLC: 2007.

40. Hansen, C. M. https://www.Hansen-Solubility.com/Hsp-Examples/Double-Sphere.Php.

41. Gee, G. Interaction between Rubber and Liquids. Iv. Factors Governing the Absorption of Oil by Rubber. *Rubber Chem. Technol.* **1943**, *16*, 818-833.

42. Kwei, T. K. *Crc Handbook of Polymer-Liquid Interaction Parameters and Solubility Parameters by Allan F M Barton, crc Press (1990)*. crc Press: 1992; Vol. 3.

43. Lee, J. N.; Park, C.; Whitesides, G. M. Solvent Compatibility of Poly(dimethylsiloxane)-Based Microfluidic Devices. *Anal. Chem.* **2003**, *75*, 6544-6554.

44. Rumens, C. V.; Ziai, M. A.; Belsey, K. E.; Batchelor, J. C.; Holder, S. J. Swelling of PDMS Networks in Solvent Vapours; Applications for Passive RFID Wireless Sensors. *J. Mater. Chem. C* **2015**, *3* (39), 10091-10098.

45. Zhang, D.; Yang, X. *Precipitation Polymerization. In Encyclopedia of Polymeric Nanomaterials*. Springer Berlin Heildelberg: Berlin, Heidelberg, 2012.

46. Macintyre, F. S.; Sherrington, D. C. Control of Porous Morphology in Suspension Polymerized Poly(divinylbenzene) Resins Using Oligomeric Porogens. *Macromolecules* **2004**, *37*, 7628-7636.

47. Mohamed, M. H.; Wilson, L. D. Porous Copolymer Resins: Tuning Pore Structure and Surface Area with Non Reactive Porogens. *Nanomaterials (Basel)* **2012**, *2* (2), 163-186.

48. Schmidtke, J.; Stille, W.; Strobl, G. Static and Dynamic Light Scattering of a Nematic Side-Group Polysiloxane. *Macromolecules* **2000**, *33*, 2922-2928.

49. Andre, P.; Folk, S. L.; Adam, M.; Rubinstein, M.; DeSimone, J. Light Scattering Study of Polydimethyl Siloxane in Liquid and Supercritical Carbon Dioxide. *J. Phys. Chem. A* **2004**, *108*, 9901-9907.

50. Soraru, G. D. Silicon Oxycarbide Glasses from Gels. *J. Sol-Gel Sci. Technol.* **1994**, *2*, 843-848.

51. Lu, K. Porous and High Surface Area Silicon Oxycarbide-Based Materials—A review. *Mater. Sci. Eng. R Rep.* **2015**, *97*, 23-49.

52. Vakifahmetoglu, C.; Zeydanli, D.; Colombo, P. Porous Polymer Derived Ceramics. *Mater. Sci. Eng. R Rep.* **2016**, *106*, 1-30.

53. Vakifahmetoglu, C.; Zeydanli, D.; Ozalp, V. C.; Borsa, B. A.; Soraru, G. D. Hierarchically Porous Polymer Derived Ceramics: A promising Platform for Multidrug Delivery Systems. *Mater. Des.* **2018**, *140*, 37-44.

54. Mera, G.; Navrotsky, A.; Sen, S.; Kleebe, H.-J.; Riedel, R. Polymer-Derived SiCN and SiOC Ceramics – Structure and Energetics at the Nanoscale. *J. Mater. Chem. A* **2013**, *1* (12), 3826.

55. Hurwitz, F. I.; Heimann, P.; Farmer, S. C.; Jr, D. M. H. Characterization of the Pyrolytic Conversion of Polysilsesquioxanes to Silicon Oxycarbides. *J. Mater. Sci.* **1993**, *28*, 6622-6630.

56. Lu, K.; Li, J. Fundamental Understanding of Water Vapor Effect on SiOC Evolution during Pyrolysis. *J. Eur. Ceram. Soc.* **2016**, *36* (3), 411-422.

57. Soraru, G. D.; Modena, S.; Guadagnino, E.; Colombo, P.; Egan, J.; Pantano, C. Chemical Durability of Silicon Oxycarbide Glasses. *J. Amer. Ceram. Soc.* **2002**, *85* (6), 1529–36.

58. Bernhardt, E. S.; Rosi, E. J.; Gessner, M. O. Synthetic Chemicals as Agents of Global Change. *Front. Ecol. Environ.* **2017**, *15* (2), 84-90.

59. Alinsafi, A.; da Motta, M.; Le Bonté, S.; Pons, M. N.; Benhammou, A. Effect of Variability on the Treatment of Textile Dyeing Wastewater by Activated Sludge. *Dyes and Pigments* **2006**, *69* (1-2), 31-39.

60. Xu, J.; Xu, D.; Zhu, B.; Cheng, B.; Jiang, C. Adsorptive Removal of an Anionic Dye Congo Red by Flower-like Hierarchical Magnesium Oxide (MgO)-Graphene Oxide Composite Microspheres. *Appl. Surf. Sci.* **2018**, *435*, 1136-1142.

61. Barret, E. P. Joner, L. G; Halenda, P. P. The Determination of Pore Volume and Area Distributions in Porous Substances. I. Computations from Nitrogen Isotherms. *J. Am. Ceram. Soc.* **1951**, *73* (1), 373-380.

62. Micromeritics ASAP2020 Operator's manual V4.01(2011). **2011**.

63. Dibandjo, P.; Diré, S.; Babonneau, F.; Soraru, G. D. Influence of the Polymer Architecture on the High Temperature Behavior of SiCO Glasses: A Comparison between Linear- and Cyclic-Derived Precursors. *J. Non-Cryst. Solids* **2010**, *356* (3), 132-140.

64. Soraru, G. D.; D'Andrea, G.; Campostrini, R.; Babonneau, F. Characterization of Methyl-substituted Silica Gels with Si-H Functionalities. *J. Mater. Chem.* **1995**, *5* (9), 1363-1374.

65. Bois, L.; Maquet, J.; Babonneau, F.; Mutin, H.; Bahloul, D. Structural Characterization of Sol-Gel Derived Oxycarbide Glasses. 1. Study of the Pyrolysis Process. *Chem. Mater.* **1994**, *6*, 796-802.

66. Thommes, M.; Kaneko, K.; Neimark, A. V.; Olivier, J. P.; Rodriguez-Reinoso, F.; Rouquerol, J.; Sing, K. S. W. Physisorption of Gases, with Special Reference to the Evaluation of Surface Area and Pore Size Distribution (IUPAC Technical Report). *Pure Appl. Chem.* **2015**, *87* (9-10).

67. Sing, K. S. W.; Everett, D. H.; Haul, R. A. W.; Moscou, L.; Pieroti, R. A.; Rouquerol, J.; Siemieniewska, T. Reporting Physisorption Data for Gas: Solid Systems with Special Reference to the Determination of Surface Area and Porosity. *Pure Appl. Chem.* **1985**, *57*.

68. Walter, S.; Soraru, G. D.; Brequel, H.; Enzo, S. Microstructural and Mechanical Characterization of Sol Gel-derived Si–O–C Glasses. *J. Eur. Ceram. Soc.* **2002**, *22*, 2389-2400.

69. Pantano, C. G.; Singh, A. K.; Zhang, H. Silicon Oxycarbide Glasses. *J Sol-Gel Sci. Technol.* **1999**, *14*, 7-25.

70. Babonneau, F.; Thorne, K.; Mackenzie, J. D. Dimethyldiethoxysilane:Tetraethoxysilane Copolymers- Precursors for the Si-C-O System. *Chem. Mater.* **1989**, *1*, 554-558.

71. Zhang, H.; Pantano, C. G. Synthesis and Characterization of Silicon Oxycarbide Glasses *J. Amer. Ceram. Soc.* **1990**, *73* (4), 958-63

72. Singh, A. K.; Pantano, C. G. Porous Silicon Oxycarbide Glasses. *J. Am. Ceram. Soc.* **1996**, *79* (10), 2696-2704.

73. Hereid, S.; Einarsrud, M.-A.; Scherer, G. W. Mechanical Strengthening of TMOS-Based Alcogels by Aging in Silane Solutions. *J. Sol-Gel Sci. Technol.* **1994**, *3*, 199-204.

74. Smitha, S.; Shajesh, P.; Aravind, P. R.; Kumar, S. R.; Pillai, P. K.; Warrier, K. G. K. Effect of Aging Time and Concentration of Aging Solution on the

Porosity Characteristics of Subcritically Dried Silica Aerogels. *Micropor. Mesopor. Mat.* **2006**, *91* (1-3), 286-292.

75. Tamayo, A.; Mazo, M. A.; Veiga, M. D.; Ruiz-Caro, R.; Notario-Perez, F.; Rubio, J. Drug Kinetics Release from Eudragit - Tenofovir@SiOC tablets. *Mater. Sci. Eng. C Mater. Biol. Appl.* **2017**, *75*, 1097-1105.

76. Meier, A.; Weinberger, M.; Pinkert, K.; Oschatz, M.; Paasch, S.; Giebeler, L.; Althues, H.; Brunner, E.; Eckert, J.; Kaskel, S. Silicon Oxycarbide-Derived Carbons from a Polyphenylsilsequioxane Precursor for Supercapacitor Applications. *Micropor. Mesopor. Mat.* **2014**, *188*, 140-148.

77. David, L.; Bhandavat, R.; Barrera, U.; Singh, G. Silicon Oxycarbide Glass-Graphene Composite Paper Electrode for Long-Cycle Lithium-Ion Batteries. *Nat. Commun.* **2016**, *7*, 10998.

78. Kaspar, J.; Mera, G.; Nowak, A. P.; Graczyk-Zajac, M.; Riedel, R. Electrochemical Study of Lithium Insertion into Carbon-Rich Polymer-Derived Silicon Carbonitride Ceramics. *Electrochim. Acta* **2010**, *56* (1), 174-182.

79. Zhang, H.; Pantano, C. G. Synthesis and Characterization of Silicon Oxycarbide Glasses. *J. Am. Ceram. Soc.* **1990**, *73* (4), 958-963.

80. Abramoff, M. D.; Magalhaes, P. J.; Ram, S. J. Image Processing with ImageJ. *Biophotonics Intern.* **2004**, *11* (7), 36-42.

81. Hackley, V. A.; Ferraris, C. F. The Use of Nomenclature in Dispersion Science and Technology. *National Institute of Standards and Technology* **2001**.

82. Huang, D.; Zhang, M.; Shi, L.; Yuan, Q.; Wang, S. Effects of Particle Size of Silica Aerogel on its Nano-Porous Structure and Thermal Behaviors under Both Ambient and High Temperatures. *J. Nanopart. Res.* **2018**, *20* (11).

83. Thommes, M.; Cychosz, K. A. Physical Adsorption Characterization of Nanoporous Materials: Progress and Challenges. *Adsorption* **2014**, *20* (2-3), 233-250.

84. Tamayo, A.; Rubio, J.; Peña-Alonso, R.; Rubio, F.; Oteo, J. L. Gradient Pore Size Distributions in Porous Silicon Oxycarbide Materials. *J. Eur. Ceram. Soc.* **2008**, *28* (9), 1871-1879.

85. Belot, V., Corriu, R. J. P., Leclercq, D., Mutin, P. H. and Vioux, A. J. Thermal Redistribution Reactions in Crosslinked Polysiloxanes. *J. Polym. Sci. A: Polym. Chem.* **1992**, *30* (4), 613-623.

86. Greil, P. Active-Filler-Controlled Pyrolysis of Preceramic Polymers. *J. Am. Ceram. Soc.* **1995**, *78* (4), 835-48.

87. Thommes, M. Physical Adsorption Characterization of Nanoporous Materials. *Chem. Ing. Tech.* **2010**, *82* (7), 1059-1073.

88. Kenvin, J.; Mitchell, S.; Sterling, M.; Warringham, R.; Keller, T. C.; Crivelli, P.; Jagiello, J.; Pérez-Ramírez, J. Quantifying the Complex Pore Architecture of Hierarchical Faujasite Zeolites and the Impact on Diffusion. *Adv. Funct. Mater.* **2016**, *26* (31), 5621-5630.

89. Pivin, J. C.; Colombo, P. Ceramic Coatings by Ion Irradiation of Polycarbosilanes and Polysiloxanes. *J. Mater. Sci.* **1997**, *32*, 6163-6173.

90. Das, G.; Bettotti, P.; Ferraioli, L.; Raj, R.; Mariotto, G.; Pavesi, L.; Sorarù, G. D. Study of the Pyrolysis Process of an Hybrid $CH_3SiO_{1.5}$ Gel into a SiCO Glass. *Vib. Spectrosc.* **2007**, *45* (1), 61-68.

91. Soraru, G. D.; D'Andrea, N.; Campostrini, R.; Babonneau, F.; Mariotto, G. Structural Characterization and High-Temperature Behavior of Silicon Oxycarbide Glasses Prepared from Sol-Gel Precursors Containing Si-H Bonds. *J. Am. Ceram. Soc.* **1995**, *78* (2) 379-398.

92. Corriu, R. J. P.; Leclercq, D.; Mutin, P. H.; Vioux, A. ^{29}Si Nuclear Magnetic Resonance Study of the Structure of Silicon Oxycarbide Glasses Derived from Organosilicon Precursors. *J. Mater. Sci.* **1995**, *30*, 2313-2318.

93. Rouxel, T.; Soraru, G. D.; Vicens, J. Creep Viscosity and Stress Relaxation of Gel-Derived Silicon Oxycarbide Glasses. *J. Am. Ceram. Soc.* **2001**, *84* (5), 1052-58.

94. Soraru, G. D.; Andrea, G. D.; Glisenti, A. XPS Characterization of Gel-Derived Silicon Oxycarbide Glasses. *Mater. Lett.* **1996**, *27*, 1-5.

95. Pena-Alonso, R.; Mariotto, G.; Gervais, C.; Babonneau, F.; Soraru, G. D. New Insights on the High-Temperature Nanostructure Evolution of SiOC and B-Doped SiBOC Polymer-Derived Glasses. *Chem. Mater.* **2007**, *19*, 5694-5702.

96. Brequel, H.; Parmentier, J.; Walter, S.; Badheka, R.; Trimmel, G.; Masse, S.; Latournerie, J.; Dempsey, P.; Turquat, C.; Desmartin-Chomel, A.; Neindre-Prum, L. L.; Jayasooriya, U. A.; Hourlier, D.; Kleebe, H.-J.; Soraru`, G. D.; Enzo, S.; Babonneau, F. Systematic Structural Characterization of the High-Temperature Behavior of Nearly Stoichiometric Silicon Oxycarbide Glasses. *Chem. Mater.* **2004**, *16*, 2585-2598.

97. Kolář, F.; Machovič, V.; Svítilová, J.; Borecká, L. Structural Characterization and Thermal Oxidation Resistance of Silicon Oxycarbides Produced by Polysiloxane Pyrolysis. *Mater. Chem. Phys.* **2004**, *86* (1), 88-98.

98. Origin(Pro), Origin 2019, OriginLab Corporation, Northampton, MA, USA.

99. Pradeep, V. S.; Graczyk-Zajac, M.; Riedel, R.; Soraru, G. D., New Insights in to the Lithium Storage Mechanism in Polymer Derived SiOC Anode Materials. *Electrochim. Acta* **2014**, *119*, 78-85.

100. Brequel, H.; Parmentier, J.; Soraru, G.D.; Schiffini, L.; Enzo, S. Study of the Phase Separation in Amorphous Silicon Oxycarbide Glasses under Heat Treatment. *Nanostruct. Mater.* **1999**, *11* (6), 721-731.

101. Schiavon, M.A.; Redondo, S. U. A.; Pina, S.R.O.; Yoshida, I.V.P. Investigation on Kinetics of Thermal Decomposition in Polysiloxane Networks used as Precursors of Silicon Oxycarbide Glasses. *J. Non-Cryst. Solids* **2002**, *304*, 92-100.

102. Riedel, R.; Mera, G.; Hauser, R.; Klonczynski, A. Silicon-Based Polymer-Derived Ceramics Synthesis, Properties and Applications- A Review. *J. Ceram. Soc. Jpn.* **2006**, *114* (6), 425-444.

103. Ionescu, E.; Kleebe, H. J.; Riedel, R. Silicon-Containing Polymer-Derived Ceramic Nanocomposites (PDC-NCs): Preparative Approaches and Properties. *Chem. Soc. Rev.* **2012**, *41* (15), 5032-52.

104. Scherrer, P. Bestimmung der Größe und der inneren Struktur von Kolloidteilchen mittels Röntgenstrahlen. *Nachrichten von der Gesellschaft der Wissenschaften zu Göttingen, Mathematisch-Physikalische Klasse* **1918**, *1918* (98-100).

105. Howe, J. Y.; Rawn, C. J.; Jones, L. E.; Ow, H. Improved Crystallographic Data for Graphite. *Powder Diffr.* **2003**, *18* (2), 150-154.

106. Franklin, R. E. The Structure of Graphitic Carbons. *Acta Crystallogr.* **1951**, *4*, 253-261.

107. Willemse, C. M.; Tlhomelang, K.; Jahed, N.; Baker, P. G.; Iwuoha, E. I. Metallo-Graphene Nanocomposite Electrocatalytic Platform for the Determination of Toxic Metal Ions. *Sensors* **2011**, *11* (4), 3970-3987.

108. Kamali, A. R.; Schwandt, C.; J. Fray, D. Effect of the Graphite Electrode Material on the Characteristics of Molten Salt Electrolytically Produced Carbon Nanomaterials. *Mater. Charact.* **2011**, *62* (10), 987-994.

109. Ferrari, A. C.; Robertson, J. Interpretation of Raman Spectra of Disordered and Amorphous Carbon. *Phys. Rev. B* **2000**, *61* (20), 14095-107.

110. Ferrari, A. C.; Robertson, J. Resonant Raman Spectroscopy of Disordered, Amorphous, and Diamondlike Carbon. *Phys. Rev. B* **2001,** *64* (7).

111. Stabler, C.; Reitz, A.; Stein, P.; Albert, B.; Riedel, R.; Ionescu, E. Thermal Properties of SiOC Glasses and Glass Ceramics at Elevated Temperatures. *Materials (Basel)* **2018**, *11* (2).

112. Tuinstra, F.; Koenig, J. L. Raman Spectrum of Graphite. *J. Chem. Phys.* **1970**, *53* (3), 1126-1130.

113. Bokobza, L.; Bruneel, J.-L.; Couzi, M. Raman Spectra of Carbon-Based Materials (from Graphite to Carbon Black) and of Some Silicone Composites. *C.* **2015,** *1* (1), 77-94.

114. Latournerie, J.; Dempsey, P.; Hourlier-Bahloul, D.; Bonnet, J.-P. Silicon Oxycarbide Glasses: Part 1-Thermochemical Stability. *J. Amer. Ceram. Soc.* **2006**, *89* (5), 1485-1491.

115. Liu, G.; Kaspar, J.; Reinold, L. M.; Graczyk-Zajac, M.; Riedel, R. Electrochemical Performance of DVB-Modified SiOC and SiCN Polymer-Derived Negative Electrodes for Lithium-Ion Batteries. *Electrochim. Acta* **2013**, *106*, 101-108.

116. Cançado, L. G.; Takai, K.; Enoki, T.; Endo, M.; Kim, Y. A.; Mizusaki, H.; Jorio, A.; Coelho, L. N.; Magalhães-Paniago, R.; Pimenta, M. A. General Equation for the Determination of the Crystallite Size L_a of Nanographite by Raman Spectroscopy. *Appl. Phys. Lett.* **2006**, *88* (16), 163106.

117. Cancado, L. G.; Jorio, A.; Ferreira, E. H.; Stavale, F.; Achete, C. A.; Capaz, R. B.; Moutinho, M. V.; Lombardo, A.; Kulmala, T. S.; Ferrari, A. C. Quantifying

Defects in Graphene via Raman Spectroscopy at Different Excitation Energies. *Nano Lett.* **2011**, *11* (8), 3190-6.

118. Oteo, J. L.; Mazo, M. A.; Palencia, C.; Rubio, F.; Rubio, J. Synthesis and Characterization of Silicon Oxycarbide Derived Nanocomposites Obtained through Ceramic Processing of TEOS/PDMS Preceramic Materials. *J. Nano Res.* **2011**, *14*, 27-38.

119. Sadezky, A.; Muckenhuber, H.; Grothe, H.; Niessner, R.; Pöschl, U. Raman Microspectroscopy of Soot and Related Carbonaceous Materials: Spectral Analysis and Structural Information. *Carbon* **2005**, *43* (8), 1731-1742.

120. Pawlyta, M.; Rouzaud, J.-N.; Duber, S. Raman microspectroscopy Characterization of CarbonBlacks: Spectral Analysis and Structural information. *Carbon* **2015**, *84*, 479-490.

121. Soraru, G. D.; Suttor, D. High Temperature Stability of Sol-Gel-Derived SiOC Glasses. *J. Sol-Gel Sci. Technol.* **1999**, *14*, 69-74.

122. Takahashi, T.; Colombo, P. SiOC Ceramic Foams through Melt Foaming of a Methylsilicone Preceramic Polymer. *J. Porous Mater.* **2003**, *10*, 113-121.

123. Brewer, C. M.; Bujalski, D. R.; Parent, E. V.; Su, K.; Zank, G. Insights into the Oxidation Chemistry of SiOC Ceramics Derived from Silsesquioxanes. *J. Sol-Gel Sci. Technol.* **1999**, *14*, 49-68.

Biographical Information

The author's research involves the investigation of the properties of porous and dense silicon oxycarbide (SiCO) materials. Training has been interdisciplinary, involving material science and chemistry research. The author is an experienced user of FE-SEM, TEM, Raman, FT-IR, porosimeter, XPS, TGA, DSC, and UV-Vis characterization methods. Training is based on the physical, chemical, and microstructural characterization of materials to investigate their properties and applications.

For the synthesis of pre-ceramic aerogels, solvent exchange and supercritical drying in CO_2 are performed. To synthesize ambient dried porous SiCO materials by slowly drying the gel until obtaining a porous material. For the chemical analysis of the samples, Raman, FT-IR, CHN analysis, and electron microscopy is performed. The author's primary research interest is in the applications of these materials, and the effects of different microstructural features on their properties. For example, SiCO materials with high and tailored SSA are suitable desirable for applications such as for gas adsorption for gases such as NO_2, for environmental remediation, and charge storage applications, specifically for Li-ion insertion. One of the author's projects involves the use of these materials for the removal of organic dyes in water. Using UV-Vis spectroscopy, it is possible to monitor and analyze SiCO performance for environmental remediation.

Investigating phase separation and microstructural features of bulk SiCO ceramics when exposed up to 1500 °C in Argon atmosphere is essential for the high-temperature application of these ceramics. Microstructural evolution with exposure temperature is a critical feature since it affects oxidation, creep, and crystallization resistance of these ceramics.